

ABSTRACT

Title of Dissertation: MODELING AND VALIDATION OF NEUTRON
ACTIVATION AND GAMMA-RAY
SPECTROSCOPY MEASUREMENTS AS AN
EXPLORATORY TOOL FOR NUCLEAR
FORENSIC ANALYSIS

John James Goodell, Doctor of Philosophy, 2018

Dissertation Directed by: Professor Alice C. Mignerey
Department of Chemistry and Biochemistry

The continued success of nuclear forensic analysis relies on the development of new material and process signatures. However, the unique safety hazards and strict controls concerning nuclear materials and operations limit the practicality of experimental scenarios. To bypass these limitations, the nuclear science community is increasingly reliant on simulation-based tools. In this dissertation, neutron activation and gamma-ray spectroscopy measurements are simulated to explore the activation network of stainless steel and its components using two neutron sources. The goal is to identify nuclides or ratios that are indicative of the neutron source and test their measurability in complex samples. The neutron sources are a critical assembly, providing fission spectrum neutrons, and a beryllium (Be) neutron converter, producing neutrons through various deuteron induced reactions. Simulated neutron energy

distributions are calculated using the Monte Carlo N-Particle (MCNP) radiation transport code.

Neutron activation has an inherent neutron energy dependence, making nuclide production rates contingent on the neutron energy distribution. Activation calculations performed by hand and with the FISPACT-II code are compared against experiments to validate the neutron energy distributions and assess available reaction cross-section data. Additionally, ratios of activation products common to both neutron sources are investigated to determine if they are indicative of the neutron source.

Gamma-ray spectroscopy with high-purity germanium (HPGe) detectors is the leading passive assay technique for radioactive samples, providing detailed qualitative and quantitative information while preserving sample integrity. A simple HPGe detector is modeled using MCNP to assess the measurability of different activation product ratios. The HPGe model is validated against its real counterpart to determine if the level of complexity is sufficient for this work.

Activation calculations were able to validate the critical assembly neutron energy distribution but showed significant errors in the Be converter model. Additionally, validation of activation calculations identified shortcomings in the $^{60}\text{Ni}(n,p)^{60}\text{Co}$ reaction cross section. Absent interferences, HPGe simulation performance was equivalent to the real detector. The HPGe model also showed that decay time can affect measurement accuracy when significant interferences are present. Activation product ratios identified in this work that are indicative of the neutron source are $^{57}\text{Co}/^{54}\text{Mn}$, $^{51}\text{Cr}/^{54}\text{Mn}$, $^{57}\text{Co}/^{59}\text{Fe}$, and $^{51}\text{Cr}/^{59}\text{Fe}$.

MODELING AND VALIDATION OF NEUTRON ACTIVATION AND
GAMMA-RAY SPECTROSCOPY MEASUREMENTS AS AN EXPLORATORY
TOOL FOR NUCLEAR FORENSIC ANALYSIS

by

John James Goodell

Dissertation submitted to the Faculty of the Graduate School of the
University of Maryland, College Park in partial fulfillment
of the requirements for the degree of
Doctor of Philosophy
2018

Advisory Committee:

Professor Alice C. Mignerey, Chair
Professor William B. Walters
Professor Amy S. Mullin
Professor Timothy W. Koeth
Professor Michael A. Coplan, Dean's Representative

© Copyright by
John James Goodell
2018

Dedication

To my incredible wife, Amy, thank you for always believing in me more than I believe in myself. To my amazing parents, Kenn and Nancy, thank you for always pushing me to be better, try again, learn more, and never give up on my dreams. To my grandfather, thank you for giving me something to aspire to.

Acknowledgement

I must first thank my advisor, Dr. Alice Mignerey, for starting me down this path. Upon beginning my graduate work, I was indecisive and apathetic to most research projects. I knew I wanted to pursue an advanced degree, but I lacked direction and purpose. She pointed me in the direction of nuclear forensics, and for that I am forever grateful. It has been a winding path with a few dead ends, but her continued support and encouragement has led me here.

I also want to thank Dr. Christie Egnatuk, Dr. Stephen Padgett, Dr. Kevin Roberts, and Dr. Bryan Bandong from Lawrence Livermore National Laboratory for their guidance throughout this effort. Without their mentorship, I would have had a much more difficult path.

Table of Contents

Dedication	ii
Acknowledgement	iii
List of Tables	vii
List of Figures	viii
List of Abbreviations	xi
Chapter 1: Introduction	1
1.1 A Historical Perspective	5
1.2 Principles of Nuclear Forensic Analysis	7
1.3 Research Objectives	12
Chapter 2: Radioactivity & Gamma-Ray Spectroscopy	15
2.1 The Unstable Nucleus	15
2.2 The Decay Equations	17
2.3 Neutron Activation	21
2.4 Gamma-Ray Spectroscopy	25
2.4.1 The Gamma Ray	26
2.4.2 Gamma Ray Detection Mechanisms	29
2.4.3 The Gamma-Ray Spectrum	33
2.4.4 Practical Considerations in Gamma-Ray Spectroscopy	36
Chapter 3: Data, Reactions, Sources, and Codes	40
3.1 Nuclear Data	40
3.1.1 Data Libraries	41
3.1.2 The Neutron Reaction Cross Section	43
3.2 Nuclear Reactions	47
3.2.1 Scattering Reactions	48
3.2.2 Direct Reactions	49
3.2.3 Compound Nucleus Reactions	50

3.2.4 Nuclear Structure Effects	51
3.3 Neutron Sources.....	52
3.3.1 The Flattop Critical Assembly	55
3.3.2 The UC Davis ⁹ Be Converter	56
3.4 Computation Codes.....	58
Chapter 4: Validation of a Monte Carlo HPGe Detector Model Against Irradiated Foil Gamma-Ray Spectroscopy Measurements	60
4.1 Introduction.....	60
4.1.1 Activation Product Ratios	62
4.2 Experimental.....	66
4.2.1 Foil Irradiations	66
4.2.2 Simulation	69
4.3 Results and Discussion	75
4.4 Conclusions.....	81
Chapter 5: Comparison of Irradiated Foil Measurements with Activation Calculations and HPGe Simulations.....	83
5.1 Introduction.....	83
5.1.1 The Activation Network.....	85
5.2 Experimental.....	87
5.2.1 Flattop Irradiation and Measurement	88
5.2.2 Activation Calculations	90
5.2.3 HPGe Simulation with MCNP	91
5.3 Results and Discussion	93
5.3.1 Activation Calculations vs Experiment.....	93
5.3.2 Decay Time Effects on HPGe Simulation.....	98
5.4 Conclusions.....	106
Chapter 6: Determining the Activation Network of Stainless Steel in Different Neutron Energy Regimes and Decay Scenarios Using Foil Activation Experiments and FISPACT-II Calculations.....	107
6.1 Introduction.....	107

6.2	Methodology	109
6.2.1	The Activation Network	109
6.2.2	Foil Activation Experiments	110
6.2.3	Activation Calculations	111
6.2.4	Production Rates vs Activation Network Progression	114
6.3	Results and Discussion	115
6.3.1	Input Neutron Distributions and Cross Section Validation.....	115
6.3.2	Neutron Source Dependence	118
6.3.3	Activation Network Time Progression.....	121
6.4	Conclusions.....	124
Chapter 7:	Summary	126
7.1	Simulation Efficacy	126
7.2	Future Outlook	131
Appendix A:	Equation Derivations.....	133
A.1	Nuclide Decay.....	133
A.2	Neutron Activation and Depletion	136
A.3	The Compton Scattering of Gamma rays.....	139
A.4	The Simulated Activation Product Ratio	142
Appendix B:	Simulation Descriptions and Input Files	144
B.1	The HPGe Model	144
B.2	The d+Be Neutron Converter.....	150
B.3	The Flattop Critical Assembly	153
B.4	Activation Calculations with FISPACT-II.....	155
Appendix C:	The Random Walk of MCNP	157
List of	References	159

List of Tables

Table 1.1 Categories and applications of special nuclear material (SNM).....	4
Table 4.1 Activation product ratios, reactions, and gamma rays used in analysis.....	64
Table 4.2 HPGe measurement results for Fe, Ni, and Cr foils, as atoms at t=0 with 1-sigma uncertainty (ND: not detected).....	68
Table 4.3 HPGe measurement results for SS foil, as atoms at t=0 with 1-sigma uncertainty.....	69
Table 4.4 Performance ratio values for Fe, Ni, Cr, and SS foils with 1-sigma uncertainty (ND: not detected).....	81
Table 5.1 Activation products, ratios, and gamma ray lines with 1-sigma uncertainty used in analysis	87
Table 5.2 Experiment results for selected activation products as atoms at the end of irradiation for each foil with 1-sigma uncertainty	90
Table 5.3 Coefficient values with standard deviation for the photopeak efficiency function described by Eq. (5.4).....	93
Table 6.1 C/E values with 1-sigma uncertainty for the Flattop irradiation using available libraries in FISPACT-II.....	116
Table 6.2 C/E values with 1-sigma uncertainty for the UC Davis irradiation using available libraries in FISPACT-II.....	116
Table 6.3 Experimental production rate ratios, with 1-sigma uncertainty, between UC Davis and Flattop neutron sources for common activation products.....	119
Table 7.1 Comparison of foil mass-normalized production rates from Flattop for activation calculation methods with different nuclear data libraries.	128

List of Figures

Figure 1.1 The number of incidents of unauthorized possession and related criminal activities from 1993-2015 as reported to the IAEA.....	2
Figure 1.2 Stages of the nuclear fuel cycle from ore mining to storage/disposal.	8
Figure 1.3 Pu isotope ratio correlation for different reactor types.....	10
Figure 1.4 Normalized rare earth element patterns in Australian UOC samples and the Mary Kathleen uranium ore (MKU) showing mine-to-mine variability.	11
Figure 2.1 Summary of major decay pathways for an unstable nucleus.....	16
Figure 2.2 Population variation over time for the decay of a parent nuclide either to a stable daughter, or an unstable daughter leading to a stable granddaughter.....	20
Figure 2.3 General neutron activation scheme showing neutron capture and inelastic scattering.....	22
Figure 2.4 Production and decay of an activation product for arbitrary irradiation and decay times.....	24
Figure 2.5 Decay-level scheme for ^{60}Co	27
Figure 2.6 Photon interactions with an absorbing material.	28
Figure 2.7 Signal production methods for scintillator and semiconductor gamma-ray spectrometers.	30
Figure 2.8 Spectral features resulting from gamma ray interactions.	33
Figure 2.9 The effect of the full-width at half maximum peak height (FWHM) on gamma-ray spectrum resolution.....	38
Figure 3.1 Nuclear data library energy dependent cross section comparison for the $^{58}\text{Ni}(n,\alpha)^{55}\text{Fe}$ reaction, including experimental data [78].	43
Figure 3.2 Effective cross section representation for neutron reactions in a sharp cutoff model.....	44
Figure 3.3 Energy dependence of the cross section for different neutron reactions on ^{58}Fe	46
Figure 3.4 General reaction map for neutron induced reactions on a target nuclide.	51
Figure 3.5 The Monte Carlo model energy dependent neutron flux probability and cumulative flux probability distributions for the Flattop critical assembly.....	56
Figure 3.6 The Monte Carlo model energy dependent neutron flux probability and cumulative probability distributions for the UC Davis d+Be converter.	58
Figure 4.1 Activation Map for Cr showing the 6 primary reaction pathways [80]....	65

Figure 4.2 Neutron energy spectrum resulting from the ${}^9\text{Be}(d,n){}^{10}\text{B}$ reaction at the University of California-Davis cyclotron [12].	67
Figure 4.3 Representation of the simulated HPGe detector geometry.	70
Figure 4.4 FWHM parameter fit based on experiment data, n=310.	72
Figure 4.5 Full energy photopeak efficiency comparison between experiment data, simulation without shield, and simulation with shield.	73
Figure 4.6 Spectrum comparison for irradiated Ni foil, 1.955 d post-irradiation, source-to-detector distance of 10.46 cm, normalized to the 810 keV peak.	75
Figure 4.7 Magnification of peak shift observed at the 810 keV peak in the Ni spectrum.	77
Figure 4.8 Simulation/Experiment performance ratios for the recreated count to assess the quantitative effect of the shield chamber.	78
Figure 4.9 Simulation/Experiment performance ratios for each activation product ratio for all target foils.	79
Figure 5.1 Activation map for Fe.	86
Figure 5.2 Neutron flux energy probability distribution resulting from a flux tally in the Monte Carlo model of the Flattop critical assembly.	89
Figure 5.3 C/E ratios for theoretical activation calculations of individual activation products with 1-sigma uncertainty.	94
Figure 5.4 C/E values, with 1-sigma uncertainty, at each decay time for activation product ratios from the Fe and Ni foils, as determined by HPGe simulation.	99
Figure 5.5 Decay time dependence of ${}^{59}\text{Fe}$ based activation product ratios in the Ni foil as determined by HPGe simulation.	101
Figure 5.6 C/E values, with 1-sigma uncertainty, at each decay time for activation product ratios in the SS-L foil, as determined by HPGe simulation.	102
Figure 5.7 Decay time dependence of ${}^{60}\text{Co}$ based activation product ratios in the SS-L foil as determined by HPGe simulation.	104
Figure 6.1 Activation map based on the Fe, Cr, and Ni components of stainless steel grade 304.	110
Figure 6.2 Input and re-binned neutron flux probability distributions for the Flattop critical assembly.	112
Figure 6.3 Input and re-binned neutron flux probability distributions for the d+Be neutron source at UC Davis along with experimental data.	113
Figure 6.4 Composite activation map for Flattop and UC Davis calculations using FISPACT-II with the JEFF-3.2 library.	120
Figure 6.5 The progression of the stainless steel 304 activation network in a Flattop irradiation, based FISPACT-II and the JEFF-3.2 library.	123

Figure 7.1 Activation product ratios based on simulated and experimental production rates from the Flattop and UC Davis neutron sources.	129
Figure A.1 The geometry of a Compton scattering event where energy and momentum must be conserved.	140
Figure B.1 Schematic representation of the shield chamber geometry for the HPGe detector simulation in MCNP.	145
Figure B.2 The ORTEC specification sheet for the physical detector used to build to the MCNP detector model.	149
Figure B.3 Simulation geometry in MCNP for the d+Be neutron converter at the University of California-Davis campus.	151

List of Abbreviations

Be	beryllium
C/E	Calculated/Experiment ratio
CENDL	Chinese Evaluated Nuclear Data Library
D-D	deuterium-deuterium fusion reaction
D-T	deuterium-tritium fusion reaction
E.C.	electron capture
EAF	European Activation File
ENDF	Evaluated Nuclear Data File
FEP	Full energy photopeak
FWHM	full-width at half max
GEB	Gaussian energy broadening
HEU	highly enriched uranium
HPGe	high-purity germanium (detector)
IAEA	International Atomic Energy Agency
ITDB	Incident & Trafficking Database
ITWG	Nuclear Forensics International Technical Working Group
JEFF	Joint Evaluated Fission and Fusion library
JENDL	Japanese Evaluated Nuclear Data Library
LHS	left-hand side
MCNP	Monte Carlo N-Particle radiation transport code
NaI(Tl)	sodium iodide crystal doped with thallium
NFA	nuclear forensic analysis
NRC	Nuclear Regulatory Commission
PNNL	Pacific Northwest National Laboratory

Pu	plutonium
RHS	right-hand side
SNM	special nuclear material
SS	stainless steel
SS-L(R)	Left (right) stainless steel foil
TENDL	TALYS Evaluated Nuclear Data Library
UC Davis	University of California-Davis campus
UOC	uranium ore concentrate

Chapter 1: Introduction

One of the greatest threats facing the international community is a nuclear attack. This may be in the form of deliberate actions by a state government or by the workings of a sub-national group, either state-sponsored or by their own accord. The incredible destructive ability of nuclear weapons has made them highly sought after by those who wish to inflict the greatest damage or believe they need them for survival and deterrence. This desire for nuclear material, regardless of use, has created an environment in which those interested in nuclear technologies and materials will buy, barter, or steal whatever is necessary for achieving their goals.

The magnitude of the illicit market for nuclear materials is demonstrated in the Incident and Trafficking Database (ITDB) maintained by the International Atomic Energy Agency (IAEA). The ITDB tracks data relevant to all events where nuclear and radioactive materials are found outside regulatory control. Events listed in the ITDB are voluntarily reported by participating nations and include unauthorized possession or related activities, theft and loss, and other unauthorized activities. The 2016 Fact Sheet shows that 454 events have occurred since 1993 involving unauthorized possession and related criminal activities, see Fig 1.1 [1]. During this time period, there were 13 incidents with highly enriched uranium (HEU) and 3 with plutonium (Pu). Clearly there is a continued demand for nuclear material.

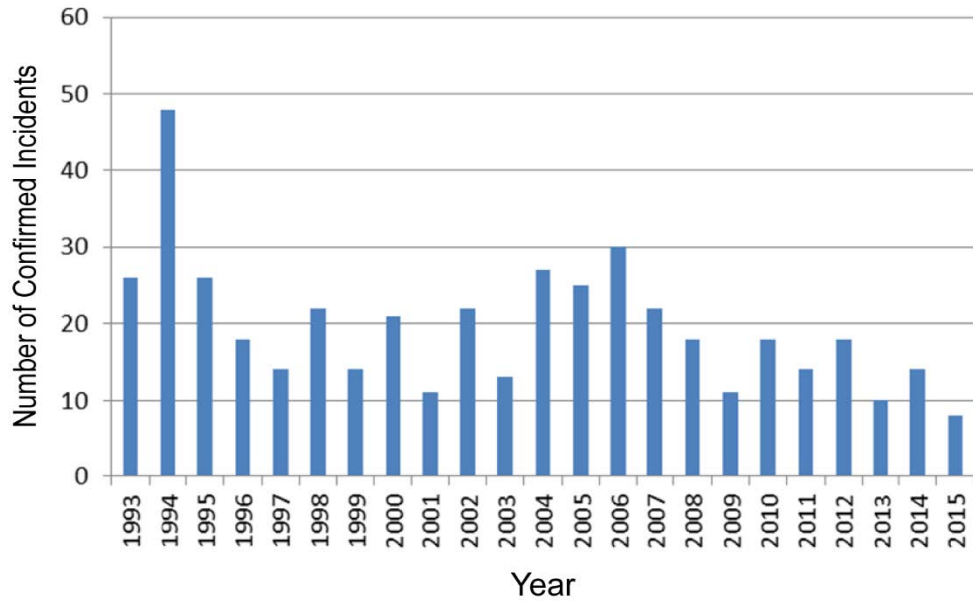


Figure 1.1 The number of incidents of unauthorized possession and related criminal activities reported each year to the IAEA Incident and Trafficking Database from 1993-2015, taken from the ITDB 2016 Fact Sheet [1].

The issue of nuclear security has become such a high priority that numerous international efforts are constantly working towards preventing nuclear proliferation. The Global Initiative to Combat Nuclear Terrorism is a multi-national partnership working towards “strengthen[ing] global capacity to prevent, detect, and respond to nuclear terrorism...” [2]. The Nuclear Forensics International Technical Working Group (ITWG) is tasked with developing techniques and signatures to be used in nuclear forensic analysis of interdicted materials [3]. The Global Threat Reduction Initiative, and the Proliferation Security Initiative are just two of the many other efforts working toward the prevention of nuclear war and terrorism [4, 5]. The continued international support for these organizations is evidence that this is a lasting concern.

In an effort to thwart those who would use nuclear weapons, law enforcement officials rely on nuclear forensic signatures to identify materials, processes, and

locations. Nuclear forensics is the science that takes place once nuclear materials are interdicted. More formally, nuclear forensic analysis (NFA) is the application of technical knowledge and methods in nuclear science to nuclear material outside of regulatory control for the support of investigations in matters of law enforcement [6–9]. NFA involves the use of various measurement techniques to determine the physical, chemical, and isotopic characteristics of samples.

In practice, there are two facets to the application of NFA: pre-detonation and post-detonation. In pre-detonation NFA, the focus is on identifying material from the nuclear fuel cycle that has fallen outside of regulatory control. Fuel cycle signatures are used to determine the type of material, its end-use, and its origin. Information gained from pre-detonation analysis can then be used to implement sanctions or additional safeguards. Post-detonation NFA focuses on device reconstruction in the event of a nuclear detonation. Post-detonation signatures are used to reconstruct the device in an effort to identify the design. There is little publicly available work on post-detonation NFA due to the classified nature of nuclear weapons designs.

The primary focus of NFA is on variants of special nuclear material (SNM), as it is the material making up the fissile components of nuclear weapons. The Atomic Energy Act of 1954 and the IAEA governing statute define SNM as ^{233}U , any uranium (U) enriched in ^{233}U or ^{235}U , or plutonium, specifically ^{239}Pu [10, 11]. SNM enrichment typically specifies the use of the material before it escaped regulatory control. Table 1.1 summarizes the enrichment categories for different SNM nuclides and their intended uses. In the case of Pu, enrichment is described by ^{240}Pu content, rather than ^{239}Pu . The goal is to minimize ^{240}Pu content since it has an appreciable spontaneous

fission rate which is problematic for use in weapons. Too much ^{240}Pu can cause premature fission of the device causing performance to suffer.

Table 1.1 Categories and applications of special nuclear material (SNM) [6, 12]

Nuclide	Isotopic Content (%)	Description and Application
^{233}U	Any	Fissile material, primary weapons component
^{235}U	< 0.72	Depleted U, evidence of enrichment activities, SNM disposition
	0.7204	Natural abundance, ore and source material
	0.72-20	Low-Enriched U, power production and research reactors
	20-90	Intermediate-Enriched U, research reactors and weapons
	>90	High-Enriched U, primary weapons component
^{240}Pu	<7	Weapons-grade, 93% ^{239}Pu as primary weapons component
	7-18	Fuel-grade, fuel for power reactors (pre-irradiation)
	18-30	Reactor-grade, fuel from power reactors (post-irradiation)
	>30	MOX-grade, Mixed-Oxide fuel blends for power reactors
Other Pu	Any	Evidence of Pu recycling for power or weapons programs

Additional materials and related nuclides relevant to the nuclear fuel cycle are also of interest in NFA investigations. Along with U and Pu isotopics, decay products, trace element profiles, physical characteristics, morphology, and any accompanying materials are all used in developing material signatures [6, 9, 13, 14]. These signatures are then used to identify the point in the nuclear fuel cycle at which the material was no longer within regulatory control. Furthermore, if the origin of the material can be identified, there is the potential that additional safeguards can be put in place to minimize any recurring loss of material.

1.1 A Historical Perspective

NFA was unofficially born out of the World War II weapons programs and intelligence efforts as world powers sought to be the first to acquire nuclear weapons. The underlying science developed in the weapons programs laid the foundation for the techniques and signatures used today. In the late 1950s, the IAEA was established to promote the peaceful use of nuclear energy and to implement safeguards to ensure that its efforts are not used in furtherance of any military purpose [11]. The focus has been on preventing a path to nuclear weapons programs while allowing the use of nuclear energy for the benefit of society. Efforts of the IAEA and the Atoms for Peace philosophy helped spread nuclear technologies and material to other countries under peaceful intentions [15]. Continued proliferation during the Cold War gave rise to additional nuclear weapons states. Following the collapse of the Soviet Union, nuclear smuggling operations became just as much of a focal point, as much of the material in former Soviet Union states was not appropriately safeguarded [6].

Over the years since the first use of nuclear weapons, many international agreements have sought to reduce the global threat. In 1968, the Treaty on the Nonproliferation of Nuclear Weapons was signed by 190 nations to prevent horizontal proliferation, advance nuclear disarmament, and promote the peaceful use of nuclear energy [16]. The Strategic Arms Reduction Treaties signed in 1991 and 1993 sought to reduce the stockpiles of the USA and the Soviet Union [17, 18]. In 1996, the Comprehensive Nuclear-Test Ban Treaty was adopted by the United Nations General Assembly, having the goal of ending all nuclear explosions conducted for any reason [19]. The Nuclear Forensics ITWG was founded in 1995 to bring together the scientific

community, members of law enforcement, regulators, and first-responders with the goal of developing a formalism for NFA [3]. In 2010, the New START treaty was signed by the USA and Russia to further reduce weapons stockpiles after the expiration of the original START treaty [20].

In addition to these international agreements, programs like the Global Initiative to Combat Nuclear Terrorism, the Global Threat Reduction Initiative, Proliferation Security Initiative, and nuclear-weapons-free zones, among others, are also working towards eliminating the nuclear threat [2, 4, 21]. For many, global zero, the complete elimination of all nuclear weapons, is the ultimate goal. However, if just one nation retains any ability to create nuclear weapons, there will be others who will refuse to eliminate their stockpile.

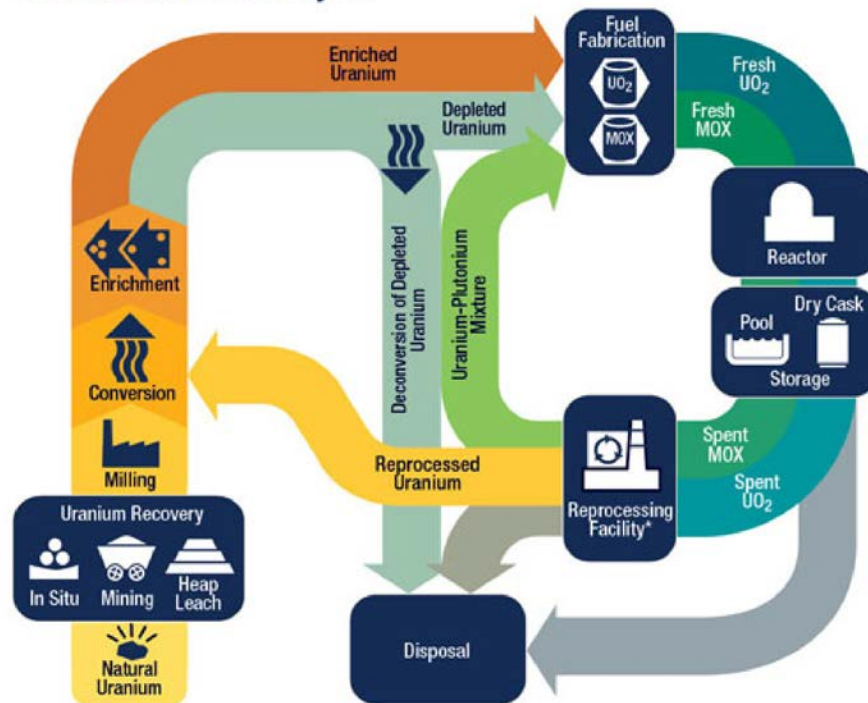
Today, the focus has shifted to nuclear terrorism by sub-national groups. Since these groups do not possess conventional infrastructure capable of providing their own materials for a weapons program, the most probable route to a weapon involves the theft or sale of SNM and related materials. Therefore, material security and the disposition of SNM is the focus of many counter-proliferation efforts. Additionally, the IAEA is tasked with enacting safeguards regimes and verification inspections to ensure that members of various international agreements are adhering to them. These safeguards and verification efforts help drive new research in NFA signatures and methods. Any newly developed techniques or signatures have the opportunity to be tested on real samples during collaborative exercises between participating members, sponsored by the ITWG [8, 14]. These exercises help the community maintain a state of readiness for when the next incident occurs.

1.2 Principles of Nuclear Forensic Analysis

The basic tenets of nuclear forensic analysis are the questions of what, where, and when as relating to the nuclear fuel cycle. What material is it? Where did it come from? When was it last processed? Answers to these questions involve various material and process signatures identified through a variety of analytical techniques. Signatures may be based in isotopic, elemental, or trace contaminants content, as well as physical or morphological characteristics. Signatures may also originate from any part of the nuclear fuel cycle, from the original mine to final waste disposal.

The nuclear fuel cycle begins with mining and milling of U ores, followed by conversion to uranium ore concentrates (UOC), commonly referred to as “yellowcake”. UOCs then go through another conversion process before being separated into enriched and depleted U. Both materials are then incorporated into the fuel fabrication process, leading to use in nuclear reactors. After being used for power production, the spent fuel is placed in interim storage before being either reprocessed or transferred to long-term disposal. Any reprocessing operations recover HEU and Pu to incorporate into additional fuel supplies. The many stages of the fuel cycle are shown in Fig 1.2. Transfer of materials between sites during these different stages presents many opportunities for materials to fall out of regulatory control.

The Nuclear Fuel Cycle



* Reprocessing of spent nuclear fuel, including mixed-oxide (MOX) fuel, is not practiced in the United States.
 Note: The NRC has no regulatory role in mining uranium.

As of June 2017



Figure 1.2 Stages of the nuclear fuel cycle beginning with natural uranium deposits, covering milling, enrichment, fuel fabrication, irradiation, reprocessing, and storage/disposal [22].

The goal of any nuclear forensic analysis is to provide actionable information about the sample to law enforcement officials. Doing so requires making decisions regarding the outcome of the analytical measurements and calculations. Decisions are made based on the type of signature, either on a predictive or comparative basis [23–25]. A predictive signature gives the precise information that is sought. The result of the analytical test for a predictive signature will directly identify a process, location, or material type. Conversely, a comparative signature cannot directly identify a process or location. Rather, a comparative signature relates multiple samples to each other and

is used to exclude possible processes or sources. Decisions made using comparative signatures often rely on statistical and graphical analysis, relative to known samples, to determine whether two or more results/samples are similar. No single signature can provide all of the necessary information, so multiple signatures are used to confirm each other and narrow the list of possibilities.

Signatures based in material isotopics cover U and Pu content as well as chronometry. Chronometry uses the relationships between members of the U and Pu decay chains to determine the time since the last purification of the sample [6, 26–28]. Chronometry can also be used to help determine if separate samples originated from the same batch of material. Uranium isotopic content can be used to identify sources of ores and UOCs, in addition to ^{235}U enrichment levels [29, 30]. Post-irradiation isotopics vary widely due to different reactor designs, burnup times, and initial fuel enrichment, making U isotopic signatures better suited to the front-end of the fuel cycle. With spent fuel samples, Pu isotopics are a better indicator of burnup, reactor type, and initial enrichment [23, 31, 32]. Figure 1.3 gives an example of how the $^{238}\text{Pu}/\text{total Pu}$ and $^{242}\text{Pu}/^{240}\text{Pu}$ ratios can be used to determine reactor type [28, 33]. Identifying sources, reactors, and timelines can help answer questions regarding route attribution and lead to improved safeguards.

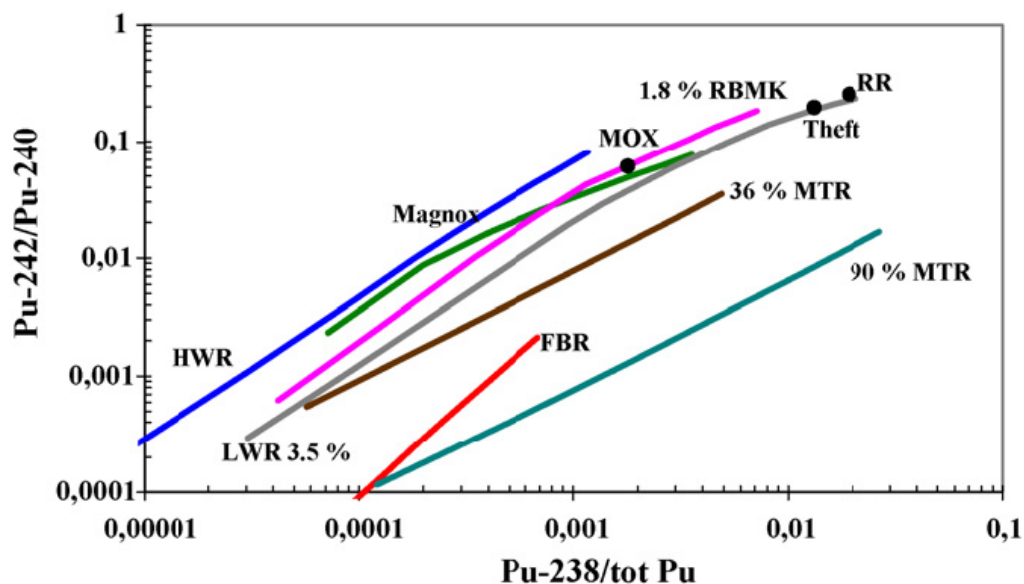


Figure 1.3 Pu isotope ratio correlation for different reactor types. Reactor types are shown as solid lines. HWR: heavy water reactor; Magnox: gas-cooled reactor; RBMK: graphite-moderated reactor; LWR: light water reactor; FBR: fast-breeder reactor; MTR: materials-testing reactor. The RR, Theft, and MOX black circles are case study results. Reprinted with permission [33]¹.

Elemental and trace component analysis can identify which process or location the material may have originated from. The relative distribution of rare earth elements found in UOCs can be indicative of the location at which the U ore was mined, resulting in location-specific rare earth element patterns as shown in Fig. 1.4 [34, 35]. Badaut *et al.* showed that anion signatures can be specific to the source of UOCs as well [36]. Trace elements may also persist through different processing steps or be introduced by the reagents used, creating process specific signatures [37].

¹ Reprinted from Journal of Alloys and Compounds, Vols. 444-445, Wallenius M, Lützenkirchen K, Mayer K et al, 57-62, Nuclear forensic investigations with a focus on plutonium, Copyright 2007, with permission from Elsevier.

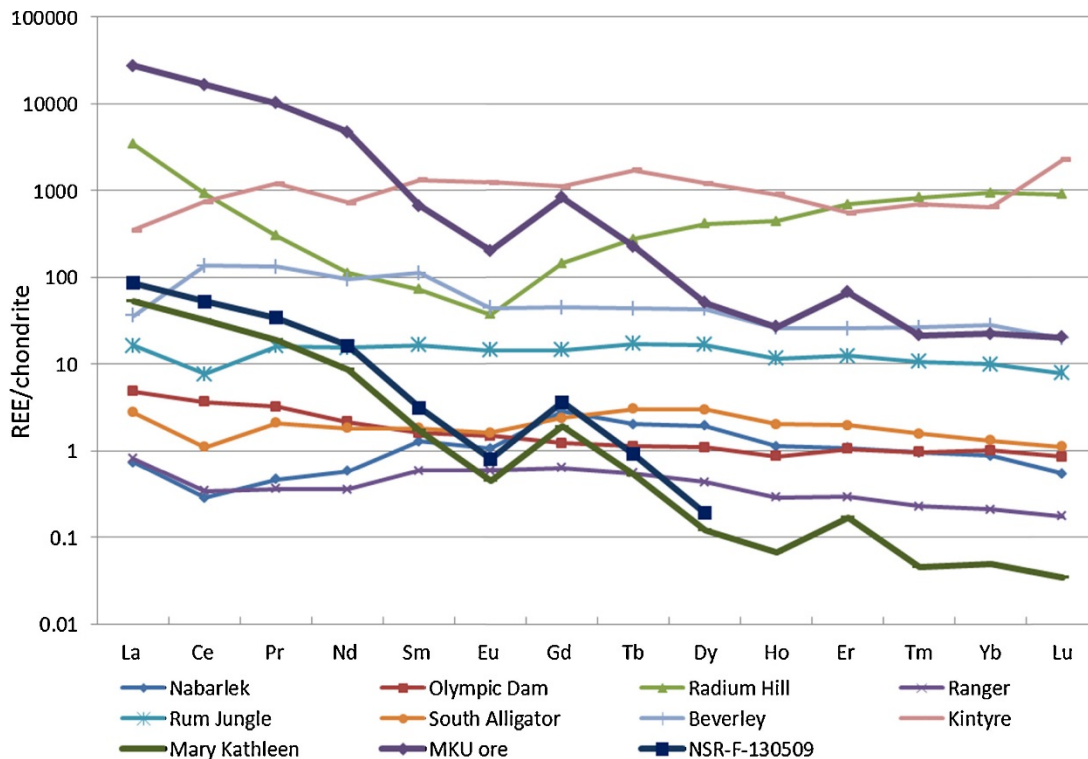


Figure 1.4 Normalized rare earth element patterns in Australian UOC samples and the Mary Kathleen uranium ore (MKU) showing mine-to-mine variability. Reprinted with permission [35]².

The morphology and physical characteristics of a sample are also important characteristics in NFA. The morphology of a sample can distinguish which type of process was used in creating UOCs or fuel pellets [14, 38]. Basic physical observations, like appearance, dimensions, and surface roughness, can immediately narrow the list of possible sources or intended uses of recovered samples [8, 14, 39]. Physical characterization is often the first step in NFA.

The nature of the fuel cycle dictates that the different signatures are more appropriate at different stages. U isotopics, rare earth element patterns, and trace anion

² Reprinted from Forensic Science International, Vol. 240, Keegan E, Richter S, Kelly I et al, 111-121, Nuclear forensic analysis of an unknown uranium ore concentrate sample seized in a criminal investigation in Australia, Copyright 2014, with permission from Elsevier.

signatures are most relevant for UOCs and U ores. Morphology and other trace element signatures are useful for determining the types of processes that may have been used. Chronometry is useful for establishing sample timelines. Pu isotopics are best-suited for the analysis of spent fuel. Any overlap of signatures only helps to verify results and constrain possibilities. The combination of multiple signatures begins to establish a complete history of the sample, providing direction for law enforcement officials.

1.3 Research Objectives

Most of the research in NFA and the development of signatures deals with the pre-detonation scenarios. This is primarily due to the ban on nuclear device testing imposed by the Comprehensive Nuclear-Test Ban Treaty and that much of the post-detonation research being done is not available in the open literature. Current efforts in signature development deal primarily with the characteristics of seized material. These signatures focus on using isotopic and elemental profiles along with physical and morphological characteristics. Because of this, the actinides, fission products, and process related identifiers have been well studied.

An area of lesser focus is activation products – nuclides produced through the irradiation of a given material, typically by a neutron source. Activation products have the potential to generate useful signatures in both pre-detonation and post-detonation scenarios. Activation products or ratios may be characteristic of the type of neutron source or provide details on the irradiation characteristics of a sample, making them a promising area for new signatures [40, 41]. Signatures based in activation products or

ratios could find applications in treaty monitoring and verification efforts, or in nuclear device reconstruction after a detonation event.

The objective of this dissertation is to develop simulation-based tools to aid in the search for new signatures for use in NFA. Simulations allow for the rapid evaluation of many different scenarios, some of which cannot be achieved experimentally, with minimal resource costs. In this work, simulations will be used to explore different neutron irradiation and measurement conditions in order to identify new diagnostic nuclides. For this purpose, a diagnostic nuclide is one that can provide information on, or constrain the possibilities of, any neutron source for the purposes of determining the neutron emitting material, reactor type, or weapon design.

The approach used here is to investigate the activation products of stainless steel. Stainless steel has become ubiquitous in modern life and is widely used as structural components in many industries, including the nuclear industry [42]. The premise is that identifying activation products in stainless steel variants would create additional constraints on the characteristics of the neutron spectrum. With a well characterized neutron spectrum, the neutron source can be identified. Activation products may not always be solely capable of making the necessary determinations, but they do serve as part of a diagnostic suite of nuclides that include fission products and other auxiliary nuclides.

The simulations that are used in this work include both neutron activation and gamma-ray spectroscopy measurements. The activation network dependency on the neutron profile will be explored using neutron irradiation simulations. The ability to measure activation products will be determined by using a gamma-ray spectroscopy

simulation. The goal is to identify unique nuclides or ratios that are characteristic of the neutron source responsible for the irradiation.

In the chapters that follow, the basic concepts are presented and then applied in the effort of new signature development based on activation products. Chapter 2 describes the mathematics of radioactive decay and neutron activation, along with the fundamentals of gamma rays and their measurement. In Chapter 3, more details are provided on neutron activation with regards to nuclear data and reaction cross sections. Chapter 3 also provides a general discussion of neutron production methods and describes the neutron sources of this work in greater detail. Chapter 4 is adapted from [43] which has been published in the Journal of Radioanalytical and Nuclear Chemistry. It provides validation for the high-purity germanium gamma-ray detector model against experimental measurements.

Chapter 5 is adapted from [44] and discusses results from activation calculations for the Flattop critical assembly. It is currently under peer review at the Journal of Radioanalytical and Nuclear Chemistry. Chapter 6 compares results of activation calculations between the Flattop critical assembly and the d+Be neutron converter at the University of California-Davis campus. The objective of this dissertation is to develop simulations that accurately reflect experimental conditions which can then be used to efficiently explore different irradiation and measurement scenarios and prove useful for developing new nuclear forensic signatures.

Chapter 2: Radioactivity & Gamma-Ray Spectroscopy

This chapter provides a working knowledge of the concepts that will be encountered in the later chapters. An overview of the underlying principles of radioactivity is offered first, followed by a discussion of the mathematical workings of radioactive decay. The concepts discussed in the mathematics of decay are then extended to use in neutron activation. Appendix A offers step-by-step derivations of the equations presented in Sec. 2.2, Sec. 2.3, and Sec. 2.4.1. A more detailed treatment of reactions and cross sections is saved for Chap. 3. Chapter 2 ends with a discussion of gamma-ray spectroscopy, providing a theoretical basis for measurements along with practical considerations.

2.1 *The Unstable Nucleus*

Radioactive decay comes in many forms, all sharing the same basic principle: the release of energy from an unstable nucleus as it transitions from higher energy states to lower energy states. A nucleus may reach an excited state through interactions with other particles, or by decay from other radioactive nuclides. If the ground state also happens to be unstable, decay will continue to occur until a stable ground state is reached. Any decay process defining multiple transitions across more than one nuclide is called a decay-chain. As mentioned in Chap. 1, decay chains are very useful for chronometry studies in nuclear forensic analysis.

The process through which energy is released during decay determines the specific decay mode. Possibilities include the conversion between neutrons and

protons, as well as the emission of high energy photons or light nuclei, and the disintegration of heavy nuclei in some circumstances. The major decay pathways are summarized in Fig. 2.1.

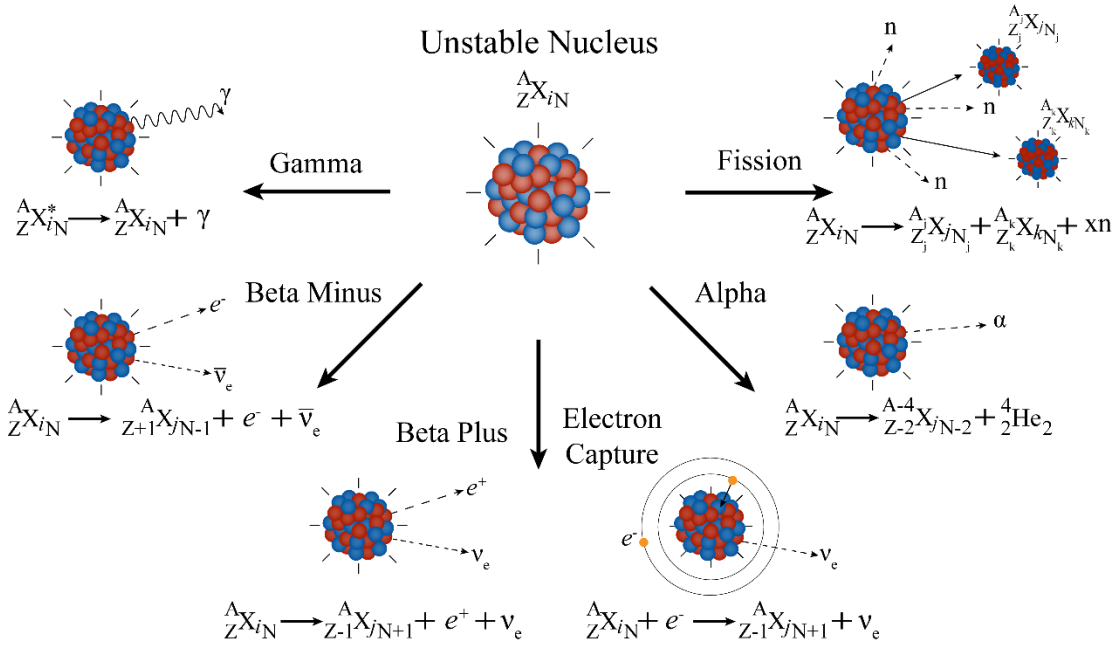


Figure 2.1 Summary of major decay pathways for an unstable nucleus, showing gamma emission, beta minus, beta plus and electron capture, alpha, and fission.

Conversion between neutrons and protons gives two distinct decay modes, depending on the direction of the conversion. Converting a neutron to a proton is defined as beta minus decay and also includes the emission of an electron (e^-) and an antineutrino ($\bar{\nu}_e$). Similarly, the conversion of a proton to a neutron with the emission of a positron (e^+) and a neutrino (ν_e) is defined as beta plus decay or positron emission. An alternative path for converting a proton to a neutron is electron capture, and involves the capture of an atomic electron, accompanied by the emission of a neutrino (ν_e).

High energy photons emitted from the nucleus during transitions to lower energy levels are called gamma rays (γ). They are particularly useful in nuclear forensic analysis since they provide characteristic information indicative of the emitting nucleus in a sample. The characteristic nature of gamma rays is based on the defined energy level structure of nuclei, resulting in unique gamma-ray signatures [6, 45, 46]. The detection of these signatures is a primary focus area in nuclear forensic analysis.

The most notable emission of a light nucleus is the creation of an alpha particle (α). An alpha particle is a ${}^4\text{He}$ nucleus, containing 2 protons and 2 neutrons. Alpha emission is commonly seen as the primary decay mode between heavy nuclei [45, 46]. Another decay mode of heavy nuclei is fission. Fission may be spontaneous or caused by excitation of the nucleus to an appropriate energy level, either through neutron or photon absorption. In fission events, the unstable nucleus splits into two fragments, emits multiple neutrons, and releases large amounts of energy.

Other decay modes, such as proton and neutron emission, are possible but less likely. These decay modes are reserved for more exotic nuclei that are not frequently encountered. Of the possible decay modes, gamma ray emission is of greatest interest in the remainder of this work. The detection of gamma rays is discussed in Sec. 2.4 and applications relevant to this work are discussed in Chap. 4 and 5.

2.2 *The Decay Equations*

Radioactive decay is a random process that follows first-order kinetics, where the rate of decay is proportional to the number of atoms of an unstable nuclide

(radionuclide), present in the sample. In this process, the decaying nuclide is referred to as the parent while the decay product nuclide is referred to as the daughter. As time proceeds and individual atoms decay away, the overall population of the radionuclide decreases along with the rate of decay. The proportionality constant is specific to each radionuclide and named the decay constant, given by λ . For a given radionuclide A, the rate at which the population (N_A) changes with time is given by Eq. (2.1):

$$dN_A/dt = -\lambda_A N_A. \quad (2.1)$$

Rearranging and solving the resulting differential equation using the initial condition that at $t=0$ there were N_0 atoms of A gives Eq. (2.2):

$$N_A(t) = N_{A0} e^{-\lambda_A(t-t_0)}. \quad (2.2)$$

Expressing $t-t_0$ as the elapsed time t gives the common expression for the population of radionuclide A, where t is the length of the decay period. Multiplying the population, $N_A(t)$, by the decay constant, λ_A , gives the instantaneous rate of decay at time t , which is defined as the activity (A) of the sample and is equivalent to Eq. (2.1).

The magnitude and range of decay constants makes it difficult to relate them to the passage of time. A more easily understood concept is the half-life ($t_{1/2}$), which is defined as the amount of time required for half of the population of radionuclide A to decay away. If N_{A0} is the amount of radionuclide A at $t=0$, then after one half-life passes, only 50% of N_{A0} remains. After two half-lives have passed, only 25% of N_{A0} is left. As more half-lives pass, the amount of N_A continues to decrease by half of the preceding value for each additional half-life time period. Eq. (2.3) describes the relationship between the half-life and the decay constant of any radionuclide.

$$t_{1/2} = \ln(2)/\lambda \quad (2.3)$$

The discussion of Eq. (2.1) describes the simple case of radioactive decay, where only the decay of a single radionuclide is considered. If the decay of the parent, radionuclide A, results in a daughter nuclide that is also unstable, radionuclide B, then B will decay into radionuclide C, and so on until a stable nuclide is reached. The expression for the rate of decay of B requires an additional term to account for the production of B from A. The rate equation for B then becomes Eq. (2.4):

$$dN_B/dt = -\lambda_B N_B + \lambda_A N_A. \quad (2.4)$$

Substituting Eq. (2.2) for N_A and solving the differential equation with the initial condition that at $t=0$, $N_B=0$ gives Eq. (2.5):

$$N_B(t) = \frac{\lambda_A}{\lambda_B - \lambda_A} N_{A0} (e^{-\lambda_A t} - e^{-\lambda_B t}). \quad (2.5)$$

The rate equation for radionuclide C, and subsequent decay products, can be determined in a similar fashion. Extension of this process to the general case leads to the Bateman equations and their solutions [47].

The relationships expressed for the decay of the parent nuclide, given by Eq. (2.2) and Eq. (2.5), are shown in Fig. 2.2 for decay directly to a stable daughter product, as well as for a 2-step decay chain where the granddaughter product is a stable nuclide. In the first scenario, as the parent population (N_A , red) declines, the population of the stable daughter (N_C , green dash) increases at a rate equal to the decay of the parent, since decay of the parent is equivalent to growth of the stable daughter.

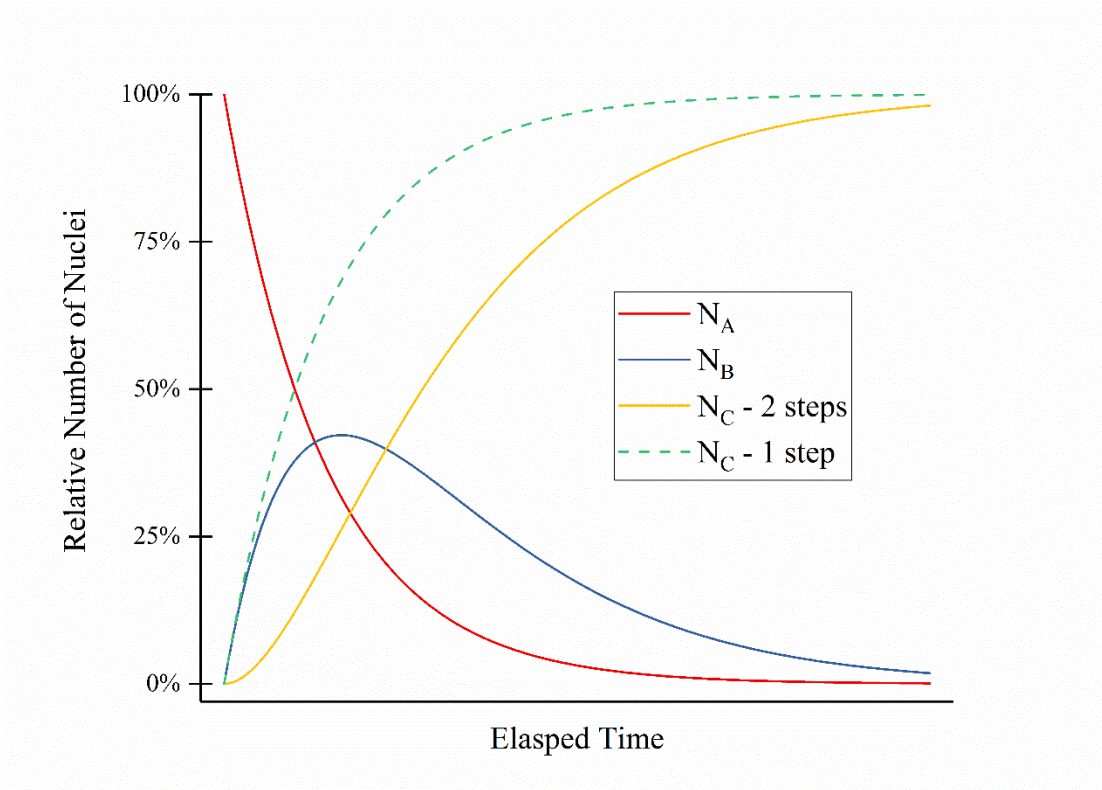


Figure 2.2 Population variation over time for the decay of a parent nuclide (N_A , red) either to a stable daughter (N_C , green dash) or an unstable daughter (N_B , blue) leading to a stable granddaughter (N_C , yellow). The half-life of the parent (A) is less than that of the daughter (B)

In the second scenario, the parent decays to an unstable daughter (N_B , blue), which then decays to a stable granddaughter (N_C , yellow). Initially, the growth rate of the daughter is the same as it was in the first scenario. Eventually, the rate of decay of the daughter exceeds the rate of decay of the parent, causing the population of the daughter to reach a local maximum. As this is occurring, the rate of growth of the stable granddaughter is initially slow, since the decay rate of the daughter is slow. After the decay rate of the daughter surpasses the decay rate of the parent, the decay of the daughter and growth of the granddaughter follow trends similar to the first scenario.

Extension of the decay equations to additional unstable progeny results in multi-step decay chains.

In the second scenario of Fig 2.2, the half-life of the parent is less than the half-life of the daughter, such that equilibrium is not reached. If the half-life of the parent is much greater than that of the daughter and observable time scales, the decay of the parent, growth of the daughter, is considered to be constant. The activity of the daughter then increases until it is equal with the parent, achieving secular equilibrium. When the half-life of the parent is greater than that of the daughter and the half-life of the daughter is non-negligible relative to the parent, transient equilibrium will occur. With transient equilibrium, the activity of the daughter grows to a maximum value before falling at a rate that appears similar to the parent.

2.3 *Neutron Activation*

Neutron activation is any neutron-based reaction which induces radioactivity in the target material. In this class of reactions, the incident neutron either transfers energy to, or is captured by, the target nucleus. Transfer of energy from the incident neutron to the target nucleus constitutes an inelastic scattering reaction, leaving the target nucleus in an excited state. Neutron capture reactions cause transmutation of the target nuclide, with the product nuclide being dependent on the particle emitted from the reaction. The general cases of inelastic scattering and neutron capture are presented in Fig. 2.3. All reactions are governed by their respective cross sections, which are interaction probabilities dependent on the neutron energy. Cross sections are specific

to each reaction, comprised of the incident particle, target nucleus, and emitted reaction product. More details on cross sections and reactions are offered in Chap. 3.

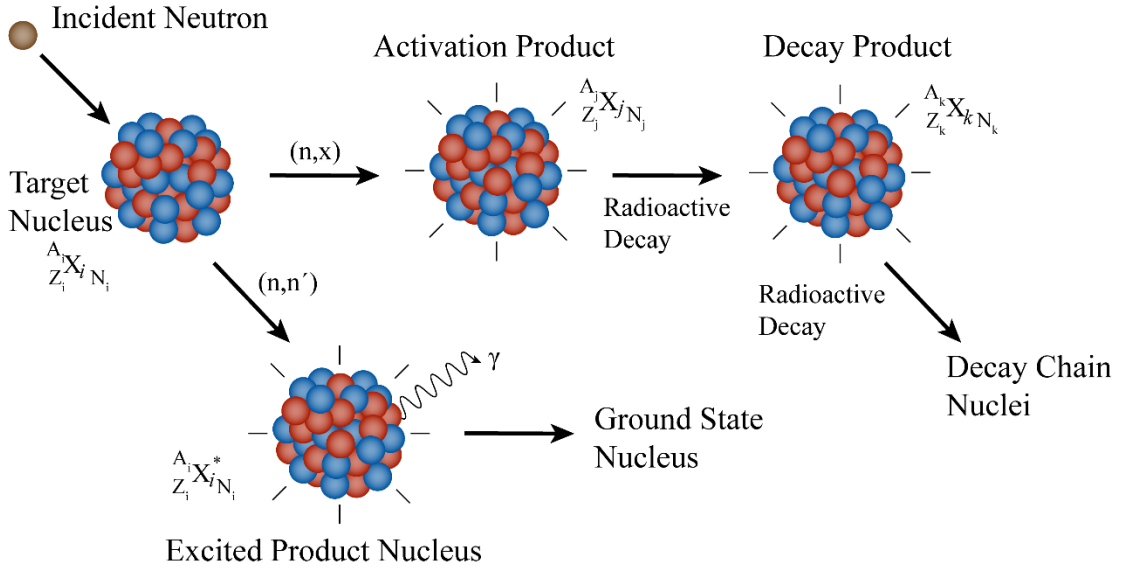


Figure 2.3 General neutron activation scheme showing neutron capture and inelastic scattering. Neutron capture reactions generate activation products, leading to additional decay products in many cases. Inelastic scattering leaves the target nucleus in an excited state, which then decays by gamma ray emission.

The rate of change of the population of a nuclide produced through a neutron capture reaction (N_p) is determined by the difference between the rate of production and the rate of decay, as given in Eq. (2.6) [46]:

$$dN_p/dt = n_0\Phi_T\bar{\sigma} - \lambda_p N_p. \quad (2.6)$$

The production rate is determined by the number of target nuclei (n_0), the energy-integrated neutron flux (Φ_T), and the collapsed cross section ($\bar{\sigma}$). The collapsed cross section is the magnitude of the cross section integrated over all neutron energies and weighted by the specific neutron energy distribution (see Sec. 3.1.2 for more details). The rate of decay for the activation product is given by Eq. (2.1). Solving the

differential equation for N_p yields Eq. (2.7), the time-dependent activation expression for the population of the product nuclide where t_{irr} is the irradiation time:

$$N_p(t_{irr}) = \frac{n_0 \Phi_T \bar{\sigma}}{\lambda_p} (1 - e^{-\lambda_p t_{irr}}). \quad (2.7)$$

This expression is useful for examining the growth of individual activation products over the course of an irradiation. Figure 2.4 shows the production and post-irradiation decay for the population of an activation product. Initially, the population is determined solely by the production term, $n_0 \Phi_T \bar{\sigma}$. Eventually, the population is large enough that the decay rate is no longer negligible in regard to the production rate, and the population curve begins to deviate from the trend of production only. The saturation value, $N_{sat} = (n_0 \Phi_T \bar{\sigma}) / \lambda_p$, is achieved when the production and decay rates reach equilibrium. The effect of irradiation time on the population for production, as well as post-irradiation decay, is illustrated in Fig. 2.4 by t_A and t_B .

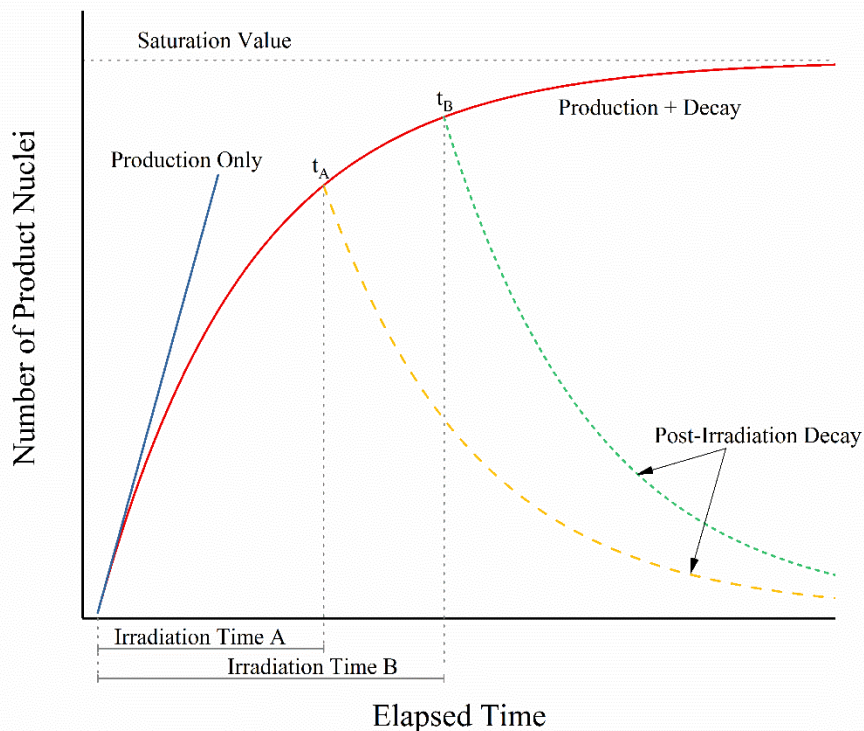


Figure 2.4 Activation product population change for arbitrary irradiation and decay times. Blue: constant rate of production; Red: decay-corrected population; Gray: saturation value. Post-irradiation decay curves for irradiations of t_A and t_B are shown in yellow (dash) and green (dot).

Experimental irradiations are often more complex, creating many routes to the same activation product. Multiple pathways may occur through different reactions on different target nuclides, or through the decay of other activation products produced by entirely different reactions. To a lesser effect, secondary activations of initial activation products may also contribute. Regardless of the route to the activation product, appropriate adjustments must be made to the rate equation.

2.4 *Gamma-Ray Spectroscopy*

Gamma-ray spectroscopy is a detection method for photons, typically with energies from 100 keV up to several MeV. The resulting energy spectrum distributions are used to identify and quantify gamma ray emitting radionuclides present in the sample. The characteristic nature of gamma rays makes them uniquely suited for nuclide identification. The simplicity of gamma-ray spectroscopy, paired with modern computer analysis programs, makes the technique an attractive option for nuclear forensic analysis.

Gamma-ray spectroscopy is a bulk sample measurement capable of providing trace level details. It proves useful in a variety of applications other than nuclear forensic analysis. Simple examples include the characterization of radioactive materials to identify and quantify active nuclides and calculate dose rates [27, 48–50]. When paired with neutron activation, gamma-ray spectroscopy measurements provide information on trace element concentrations and allow for flux characterization of neutron sources [51–53]. Gamma-ray spectroscopy is also used for investigating nuclear data, whether by using single detectors to quantify activation products and investigate reaction cross sections, or by using detector arrays to perform in-beam analysis on rare nuclei created in particle accelerators [54–56]. The breadth of applications is only limited by the ability to measure the gamma rays of interest.

The most desirable attributes of gamma-ray spectroscopy, with regards to nuclear forensic analysis, are that it is a passive and nondestructive analysis technique. These features allow investigators to obtain quantitative isotopic information about a

radioactive sample quickly and easily while preserving the integrity of the sample. Gamma-ray spectroscopy measurements can set the direction for the remainder of an investigation and provide confirmation for other measurement techniques, such as the various iterations of mass-spectrometry. Because of this, gamma-ray spectroscopy is used in all investigations of interdicted nuclear material [14].

2.4.1 The Gamma Ray

As previously stated, a gamma ray is a high energy photon emitted from the nucleus as it transitions from an excited energy level to lower energy levels, eventually reaching the ground state. The energy difference between the initial state and final state of a transition determines the photon energy. The energy levels of nuclei are well defined, giving each transition a known energy. The unique energy structure and known transitions create a gamma-ray fingerprint for each gamma ray emitting nuclide. An example is the beta minus decay of ^{60}Co to ^{60}Ni , shown in Fig. 2.5, which details the possible beta decay pathways and gamma-ray transitions. Almost all ^{60}Co decays result in the emission of two gamma rays with energies of 1173 keV and 1332 keV, respectively.

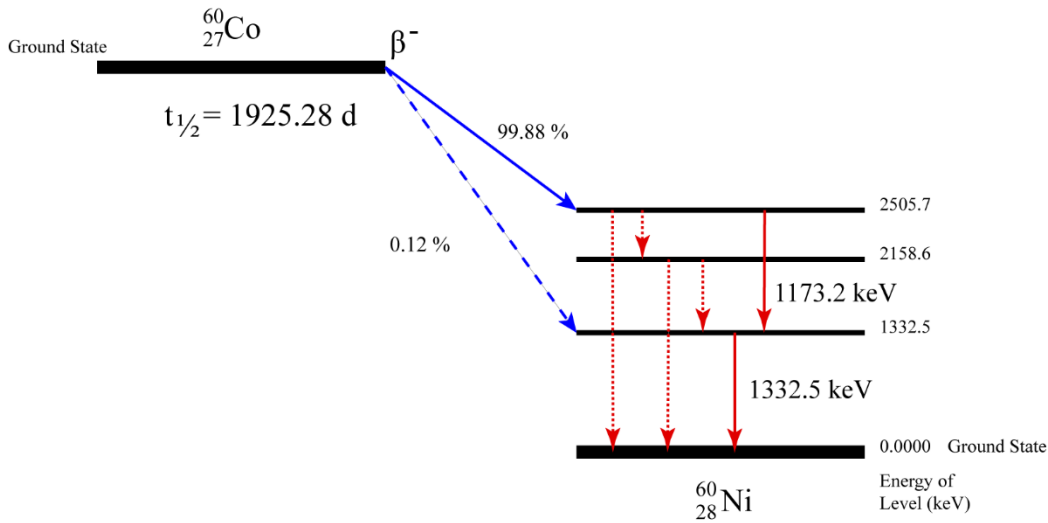


Figure 2.5 Decay-level scheme for ^{60}Co showing the transitions producing the primary gamma rays of 1173.2 keV and 1332.5 keV. Blue: beta minus decay pathways. Red: possible gamma-ray transitions. Dotted lines represent low probability transitions [57].

Gamma-ray interaction probabilities with the absorbing material are dependent, to varying degrees, on the Z-number of the material and the gamma-ray energy [46, 58]. Interactions take place through three competing processes: photoelectric absorption, Compton scattering, and pair production. Each interaction mode in a detector volume is shown in Fig 2.6. Photoelectric absorption is the process in which the energy of a gamma ray is absorbed by an atom of the absorbing material, *e.g.* the detector medium, causing the ejection of an electron with an energy of E_γ minus the binding energy of the electron. Photoelectric absorption is more common for lower energy gamma rays and high-density materials due to the Z^5 dependence of the interaction.

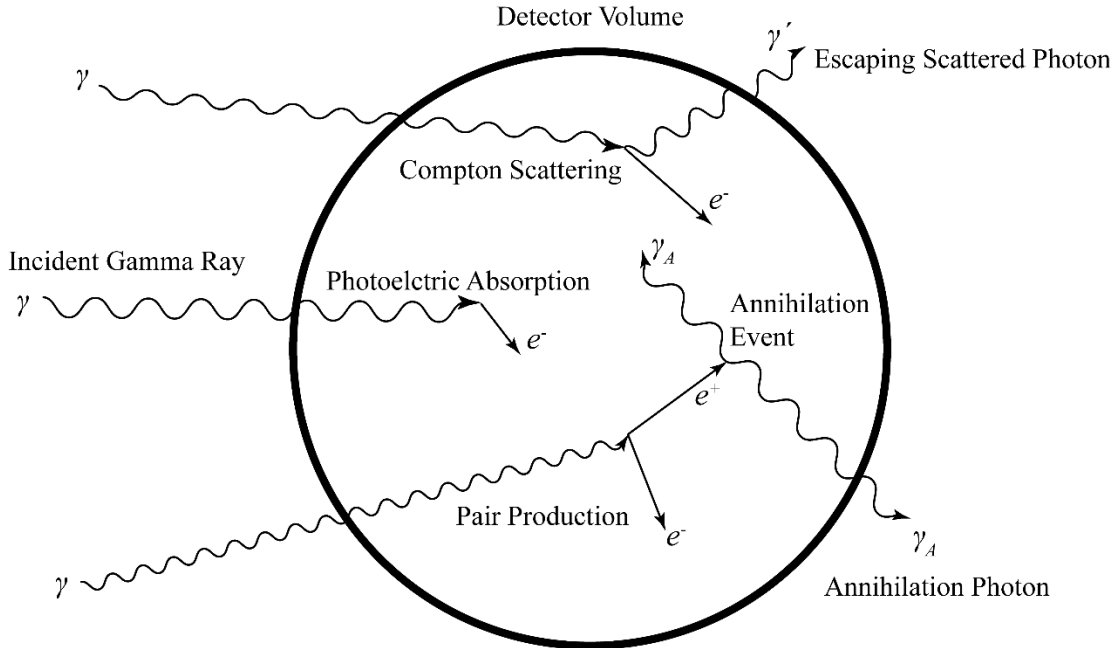


Figure 2.6 Photon interactions with an absorbing material, a detector volume in this case, showing Compton scattering, photoelectric absorption, and pair production, along with an annihilation event and the resulting annihilation photons.

Compton scattering occurs when a portion of the gamma ray energy is transferred to an electron of the absorber through a scattering event. Compton scattering probabilities are more affected by electron density than Z-number or photon energy. The energies of the scattered electron and gamma ray are dependent on the scattering angle of the photon, as given by Eq. (2.8):

$$E'_\gamma = \frac{E_\gamma}{1 + \frac{E_\gamma}{m_e c^2} (1 - \cos \theta)}. \quad (2.8)$$

E_γ is the incident photon energy, E'_γ is the scattered photon energy, $m_e c^2$ is the rest-mass energy of the electron (0.511 MeV), and θ is the scattering angle between the incident gamma-ray path and the scattered photon. The maximum energy transfer to the electron occurs for a gamma-ray scattering angle of $\theta=180^\circ$.

Pair production results in the creation of an electron-positron pair through the interaction of a gamma ray with the Coulomb field of an absorber nucleus. Since an electron and its antimatter counterpart are produced from a photon, the process requires that the gamma-ray energy exceeds 1.022 MeV, to account for the rest-mass energy of each created particle. The probability for pair production increases with Z-number and photon energy. If the positron annihilates with an electron in the absorbing material, then two photons with energies of 511 keV are created from the annihilation event.

2.4.2 Gamma Ray Detection Mechanisms

The interaction mechanisms of photoelectric absorption, Compton scattering, and pair production form the basis for measuring the gamma-ray spectrum. Gamma-ray spectrometers operate either as scintillation or semiconductor detectors. Signal production mechanisms within each type of detector are shown in Fig. 2.7 [58, 59]. For scintillators, the primary electrons created through photon interactions cause excitation of secondary electrons in the detector material. Relaxation of an excited secondary electron results in the emission of a photon, typically in the visible light range. The visible light photon then strikes the photocathode of a photomultiplier tube, causing the emission of another electron via the photoelectric effect. Amplification of this photoelectron within the photomultiplier tube creates the measured electronic signal which is proportional to the initial gamma-ray energy.

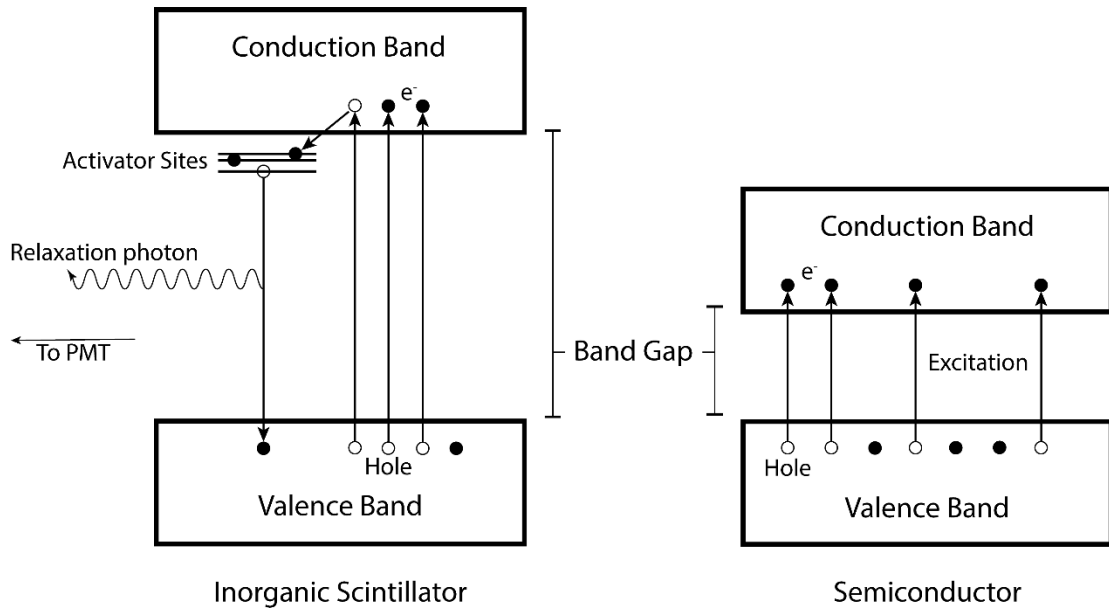


Figure 2.7 Signal production methods based on gamma-ray interactions in inorganic scintillator and semiconductor detectors. For inorganic scintillators, gamma-ray interactions elevate electrons to the conduction band, which then transition to excited activator sites, and produce a visible light photon during relaxation to the valence band. The relaxation photon creates the electrical signal via the photomultiplier tube (PMT). For semiconductors, gamma-ray interactions create electron-hole pairs which migrate in an applied electric field, generating a current pulse.

Scintillator options include both organic and inorganic, but inorganic based scintillators are better suited to gamma-ray spectroscopy because of the higher Z -values of the materials [58]. Inorganic scintillators are often doped with other elements to provide activator sites within the parent crystal bandgap. The dopant provides accessible energy levels for conduction band electrons. Relaxation from the activator sites provides the visible light photon, to which the detector crystal is transparent. In contrast, relaxation from the conduction band provides a photon outside the visible range that is likely to be reabsorbed by the crystal. A common example of an inorganic scintillation detector is the NaI crystal doped with Tl (referred to as NaI).

In semiconductor detectors, primary electrons resulting from photon interactions create electron-hole pairs in the detector material by exciting secondary electrons from the valence band to the conduction band, as shown by the right side of Fig. 2.7. This excitation leaves positively charged “holes”, or vacancies, in the valence band. An applied electric field causes the electrons and holes to migrate away from each other, generating a current pulse within the detector. The number of electron-hole pairs, and size of the resulting current pulse, is proportional to the energy deposited in the detector material by the gamma ray. An example of a semiconductor detector is the high-purity germanium crystal (HPGe).

Since the HPGe detector is a semiconductor, it has an inherent level of electron-hole pairs that is proportional to the temperature of the crystal and the band gap energy (E_G). The probability of thermal excitation of a valence electron, and creation of an electron-hole pair, is given by Eq. (2.9):

$$P(T) = aT^{3/2}e^{-\frac{E_G}{2kT}}, \quad (2.9)$$

where a is a proportionality constant specific to Ge, T is the temperature in Kelvin, k is the Boltzmann constant, and E_G is the band gap energy [58, 59]. Reducing the temperature reduces the number of electron-hole pairs inherent in the detector crystal, thereby reducing the thermal noise component of the resulting electrical signal.

Doping a high-purity Ge crystal with impurities during manufacturing results in a net reduction of the inherent level of electron-hole pairs by providing electron donor and acceptor sites which increase recombination. The differences in doped regions create a p-n junction across the Ge crystal with excess electrons and holes from

the dopants migrating towards the junction. The increase in recombination events result in a region with a reduced number of electron-hole pairs. This region is called the depletion layer and is most responsive to photons since it is essentially void of recombination sites and electron traps that would reduce the number of electron-hole pairs created through gamma-ray interactions.

In a zero bias crystal, no applied voltage, the depletion layer is relatively small. Applying a reverse bias to the doped Ge crystal increases the size of the depletion layer by drawing free electrons and holes towards the electrodes and away from the depletion region. The thickness of the depletion layer (d) is dependent on the reverse bias voltage (V), the net impurity of the bulk semiconductor material (N), the dielectric constant (ϵ) and the elementary charge (e), as given by Eq. 2.9 [58]:

$$d = \sqrt{\frac{2\epsilon V}{eN}}. \quad (2.10)$$

Reverse biasing the p-n junction also increases the leakage current and thermal excitation of the Ge crystal, increasing the electronic noise contribution. This effect is amplified in Ge because the band gap is less than 1 eV. Cooling the crystal to liquid nitrogen temperatures reduces the electronic noise signal from reverse biasing and thermal excitation, thereby improving detector performance. A high reverse bias voltage, with low impurity concentration, and operation at liquid nitrogen temperatures provides the best performance for a HPGe detector.

2.4.3 The Gamma-Ray Spectrum

For either detector type, the competing photon interaction mechanisms give rise to several distinct features when measuring a gamma-ray spectrum: the full-energy photopeak, Compton edge and continuum, multiple Compton events, single and double escape peaks, annihilation peak, X-ray peak, backscatter peak, and sum and coincidence peaks [58, 59]. The predicted detector response to gamma rays, showing each of these spectral features is shown in Fig. 2.8. The full-energy photopeak, Compton edge and continuum, multiple Compton events, annihilation peak, and single and double escape peaks are generated from source gamma-ray interactions within the detector. Interactions in the surrounding materials lead to the x-ray peak, backscatter peak, and additional contributions to the annihilation peak and Compton regions. Limitations in detector electronics give rise to the sum and coincidence peaks.

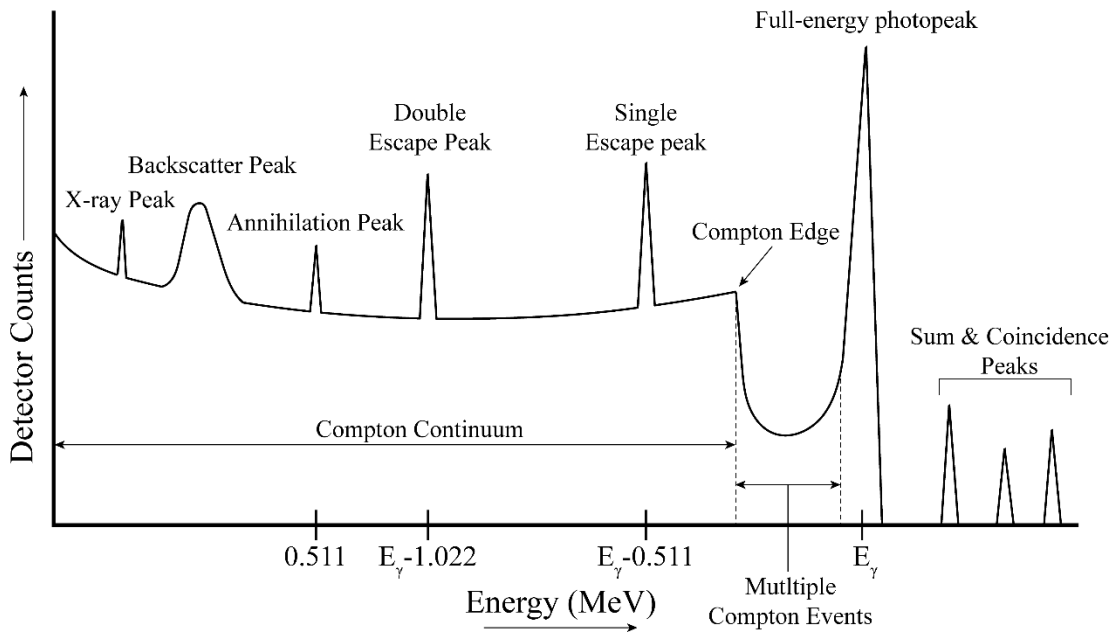


Figure 2.8 Idealized gamma-ray spectrum predicted by photon interactions in the detector volume and surrounding materials showing the variety of spectral features.

The most important feature is the full-energy photopeak, which is used for nuclide identification and quantification. This peak represents the complete deposition of the gamma-ray energy within the detector. The photopeak may arise from a combination of events as a gamma ray interacts with the detector. The simplest case is that of photoelectric absorption of the initial gamma ray. A second case involves one or more Compton scattering events, ending with photoelectric absorption of the scattered photon. The final case involves pair production with the annihilation event occurring within the detector. Here, both photons from the positron annihilation event, as well as the paired electron, deposit their energy in the detector.

Another prominent feature is the Compton continuum and edge. Detected counts in this region are generated by Compton scattering events. The scattered photon then exits the detection medium while the energy transferred to the scattered electron is deposited in the detector. The Compton edge is set by the maximum energy transfer of a scattering event, determined by Eq. (2.8) with $\theta = 180^\circ$. The Compton continuum represents all other scattering events with photon scattering angles from 0 - 180° . When multiple Compton events occur before the scattered photon escapes the detector, a continuum of counts between the Compton edge and the full-energy photopeak will be present in the spectrum.

For gamma-ray energies above 1.022 MeV, where pair production is possible, single and double escape peaks are present in the gamma-ray spectrum. Following pair production, the positron annihilates with an electron in the detection medium, generating two 511 keV photons. If one of the annihilation photons escapes without depositing any of its energy in the detector, the single escape peak is present at an

energy of $E_{\gamma}-0.511$ MeV. When both annihilation photons escape the detector without further interaction, the double escape peak is present at an energy of $E_{\gamma}-1.022$ MeV.

The only other features of a gamma-ray spectrum caused by incident gamma rays from the source are sum and coincidence peaks. They are artificial peaks and have energies greater than the photopeak. Sum and coincidence peaks are a result of the limitations in electronics and signal processing. These spurious peaks occur when multiple gamma rays interact with the detector on a time scale shorter than processing time of the associated electronics. To the detection system, the multiple gamma rays arrive simultaneously and are recorded as if they were a single gamma ray with the combined energy.

Several other spectral features occur when the detector has associated shielding or other materials are nearby. These features include the annihilation, backscatter, and X-ray peaks. The annihilation peak has an energy of 511 keV and occurs only when gamma rays above 1.022 MeV are present. Pair production events in peripheral materials create annihilation photons which may find their way to the detector. The backscatter peak occurs when gamma rays scatter off nearby materials and the scattered photon interacts with the detector. Backscatter gamma rays are generally near 250 keV due to the scattering angles required to direct the photon back to the detector [59]. Characteristic X-rays generated from photoelectric absorption events in surrounding materials, typically from Pb in shielding materials, are also common in the low energy region of gamma spectra.

2.4.4 Practical Considerations in Gamma-Ray Spectroscopy

For any gamma-ray spectroscopy measurement, one must consider the following: detection efficiency, resolution, and interferences. In general terms, detection efficiency is a measure of how well the detector counts the number of gamma rays emitted by the source. It is described by two parameters: the intrinsic efficiency of the detector, and a geometry factor. The intrinsic efficiency of the detector is determined by the ratio of the number of counts recorded by the system to the number of gamma rays incident on the detector. Intrinsic efficiency is dependent on the detector material and dimensions, and varies with photon energy. The energy dependence of the intrinsic efficiency will depend on the detector material, size, and detection mechanism. The intrinsic efficiency focuses on photopeaks, since they are the peaks of interest and are less sensitive to perturbations from other interactions such as Compton scattering from higher energy gamma rays. Efficiency functions used in quantitative analysis are generated from empirical fits to efficiency calibration data. A commonly used function for coaxial HPGe detectors is the logarithmic polynomial given in Eq. (2.11):

$$\ln(\varepsilon) = \sum_{i=0}^n a_i \left[\ln\left(\frac{E_\gamma}{E_{ref}}\right) \right]^i, \quad (2.11)$$

where ε is the photopeak efficiency, E_{ref} is a fixed reference energy in the same units as the photon energy E_γ , values of a_i are fitted coefficients, and values of i can vary based on the number of calibration points [58, 59].

The geometry factor depends on the distance between the source and detector, as well as the detector shape and dimensions. The geometry factor is determined by the solid angle subtended by the detector, as seen by the source. Practically speaking, the

geometry factor is the ratio of gamma rays incident on the detector to the number emitted by the source. The solid angle varies as $1/r^2$, where r is the source-to-detector distance [58, 59]. Therefore, as r increases, the solid angle and geometry factor decrease. Since geometry factors can be difficult to calculate and are usually measurement specific, gamma-ray spectroscopy systems are calibrated for detection efficiency beforehand. Together, calibrated intrinsic efficiency values for photopeaks and known geometry factors allow for the calculation of the source activity, based on the number of counts recorded in the photopeak.

Another consideration is detector resolution: the ability to distinguish between closely spaced gamma-ray energies. It is a function of the full-width at half maximum peak height (FWHM) for photopeaks [58]. Greater resolution corresponds to lower FWHM values, allowing for the detection of closely spaced gamma rays. Figure 2.9 shows the effect of the FWHM on resolution. Good resolution is defined as a minimum separation of peak centroids of at least 3 times the FWHM value [59]. This is shown by Peak I and Peak II in Fig. 2.9. The relationship between FWHM and resolution, shown by Peak III and Peak IV, is that smaller FWHM values describe narrower peaks, increasing the separation between neighboring peaks and providing better resolution. Neighboring peaks with larger FWHM values result in poorer resolution due to the greater potential for peak overlap. For complex spectra with many different gamma-ray energies, resolution can affect whether two photopeaks of similar energy are individually distinguishable, or if they appear as one larger peak. Poor resolution in complex gamma-ray spectra can cause some peaks of interest, particularly those with low activity, to be hidden by more prominent peaks.

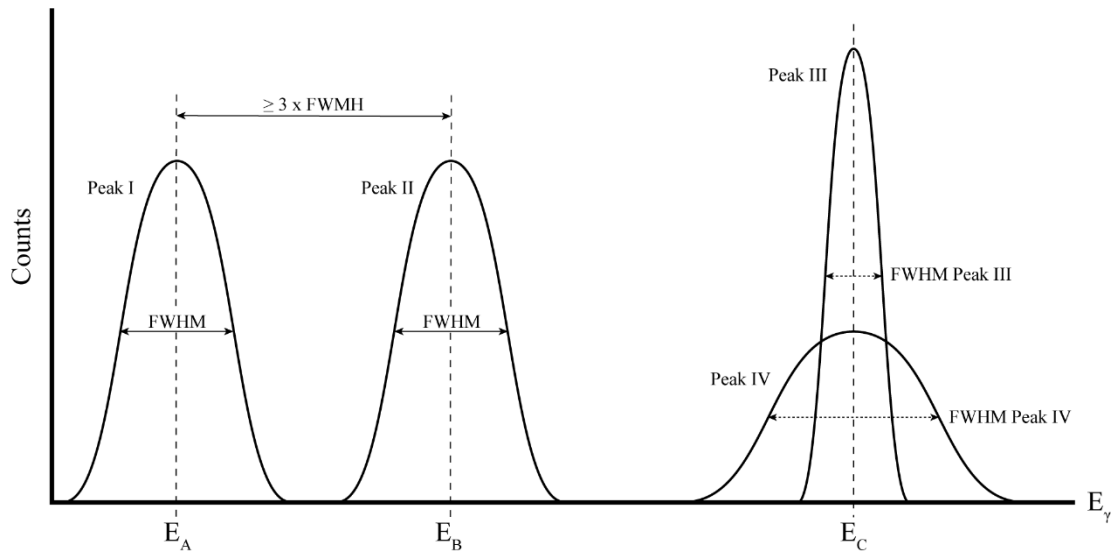


Figure 2.9 The effect of the full-width at half maximum peak height (FWHM) on gamma-ray spectrum resolution. Good resolution is achieved when peak centroid separation is at least 3 times the FWHM, as shown for Peaks I and II. Larger FWHM values, as with Peak IV compared to Peak III, lead to poorer resolution. Adapted from [58, 59].

The final consideration is interferences. Interfering gamma rays are those with similar energies to the gamma ray of interest, such that they are indistinguishable from, or greatly overlap with, the gamma ray being measured. For detectors with poor resolution, the chance for interferences is greater since the FWHM values are larger, causing peaks to cover a wider energy range within the spectra. With greater resolution and lower FWHM values, peaks are narrower, making them more distinguishable from neighboring peaks and any background.

The impact of intrinsic efficiency and resolution will vary with the choice of detector material and size. Since a range of efficiencies can be achieved by changing the dimensions of the detector or the source-to-detector distance, resolution and cost are often the deciding factors. Traditionally, the choice was between NaI and HPGc

detectors. The NaI detector offers ease of use and improved photopeak efficiency due to the higher Z -value, but at the cost of resolution. The HPGe detector provides superior resolution, but at the cost of lower efficiency and the detector must be cooled with liquid nitrogen. More recently, $\text{LaBr}_3(\text{Ce})$ scintillator detectors have been gaining popularity since they provide better resolution than NaI and retain the ease of operation. However, HPGe resolution is still superior and the $\text{LaBr}_3(\text{Ce})$ scintillator is accompanied by intrinsic radiation from the decay of native ^{138}La and the process contaminant ^{227}Ac , along with associated decay chain nuclei, which can affect measurement [58, 60, 61]. The work presented in later chapters uses HPGe detectors due to the excellent resolution, which is necessary for the complex spectra often encountered in nuclear forensic analysis.

Chapter 3: Data, Reactions, Sources, and Codes

The chapter begins by building on the concepts of nuclear reactions and cross sections introduced in Chap. 2, providing additional details and relevant discussion of the available nuclear data. Following that, an introduction to the various methods of neutron production is provided. The neutron sources used in this work are discussed in more detail. Input files for the neutron source models are offered in App. B. Finally, a brief discussion of the use of computation codes in nuclear science is offered, with a focus on the codes utilized in this dissertation. A brief description of the approach to simulations used with the Monte Carlo N-Particle radiation transport code (MCNP) is provided in App. C.

3.1 Nuclear Data

The term “nuclear data” includes many different quantities that find use in various nuclear science applications. It is a general term that can refer to nuclear structure, reactions, cross sections, fission yields, and decay parameters. Some uses of nuclear data include reactor design, activation and decay, shielding and dose assessment, and radiation detector simulations [62–70]. If it describes any interactions of nuclei, it is nuclear data.

The extensive nature of nuclear data makes it difficult to obtain a complete set of experimentally determined parameters for every possible interaction. This means that the availability of nuclear data is driven by the application, with high priority work receiving more attention. The result of this inequality means that some data may be

deficient for particular applications, while other data may be nonexistent. For the data that is available, it is organized in various nuclear data libraries.

3.1.1 Data Libraries

A nuclear data library provides a set of standard reference data of nuclear structure, decay, and reaction cross sections for the scientific community. The reference data is as complete as possible, relying on existing experimental data and current nuclear models. Collaborative groups are tasked with the process of analyzing the available experiment data and nuclear model predictions to arrive at accepted values for the various quantities, resulting in an evaluated nuclear data file. Evaluated files are then collected, processed, and packaged for easy use, resulting in the various evaluated nuclear data libraries.

Modern nuclear data libraries are stored in the Evaluated Nuclear Data File (ENDF) Version 6 format to provide a common structure ensuring functionality across different platforms [71]. The major general-purpose libraries are the ENDF-B library maintained by the Cross Section Evaluation Working Group of the U.S. Nuclear Data Program, the Joint Evaluated Fission and Fusion (JEFF) library maintained by the Nuclear Energy Agency in Europe, and the Japanese Evaluated Nuclear Data Library (JENDL) maintained by the Japanese Atomic Energy Agency [72–74]. An alternative is the TALYS Evaluated Nuclear Data Library (TENDL) which is based on the TALYS nuclear model code, maintained by NRG in the Netherlands and CEA in France, complemented by evaluated nuclear data when necessary [75, 76]. Because TENDL is

primarily based on the TALYS code, it provides data files for virtually all nuclides, including reactions for a greater variety of projectiles. Other data libraries are available but are less frequently used and may be tailored for specific applications.

A complete evaluated nuclear data file contains one or more “materials”, or nuclides, which have corresponding data types. The data types include reaction cross sections for different incident particles, cross-section resonance parameters, angular and energy distributions of reaction products, scattering and radioactivity data, specific nuclide and photon production data, and associated covariance data, along with any other descriptive and miscellaneous data. Evaluated data files are revised when new meaningful experimental results are available, data is found to produce errors, or the scientific community expresses a need for more accurate data [77].

Due to the human factor in the interpretation of experiment data and differences in the nuclear models, significant differences in reaction cross sections may exist between evaluated data libraries. An example of this is the $^{58}\text{Ni}(n,\alpha)^{55}\text{Fe}$ reaction, where ^{58}Ni is the target nuclide, n is the neutron projectile, α is the reaction ejectile (an alpha particle in this case), and ^{55}Fe is the residual nucleus from the reaction. Figure 3.1 plots the cross section for this reaction from various nuclear data libraries, in millibarns, for incident neutron energies up to 30 MeV. The evaluated data includes the ENDF-B/VII.1, JEFF-3.2, JENDL-4.0, and TENDL-2015 library data, along with available experimental data. The European Activation File from 2010 (EAF-2010) and most recent Chinese evaluated library data (CENDL-3.1) are also included. Of the evaluated cross-section data, only EAF and TENDL extend past 20 MeV. It is easy to see that there is disagreement within the evaluated libraries and also within the

experimental data. Depending on the neutron distribution, the choice of evaluated library can have a significant effect the results of activation calculations.

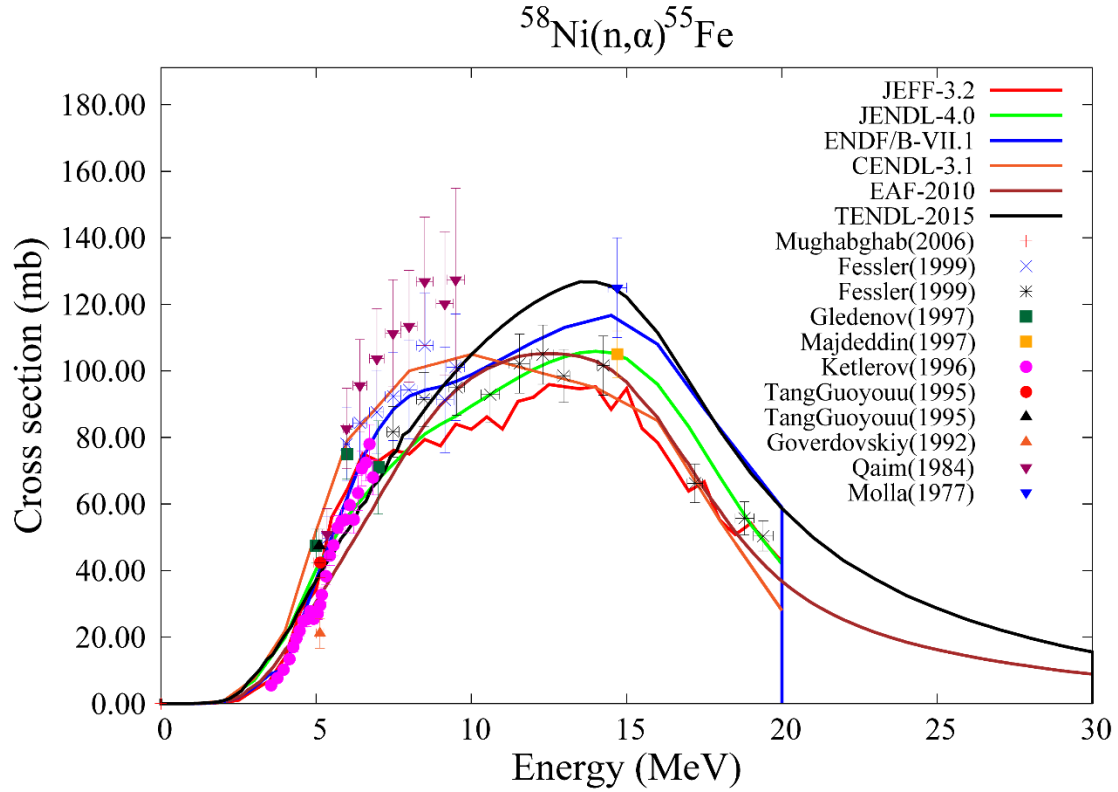


Figure 3.1 Nuclear data library energy dependent cross section comparison for the $^{58}\text{Ni}(n,\alpha)^{55}\text{Fe}$ reaction, including experimental data [78].

3.1.2 The Neutron Reaction Cross Section

Of the various quantities available in the nuclear data libraries, the neutron reaction cross section is of most importance in this work. A cross section is a probability of interaction between two particles or nuclei, having units of area. The commonly used unit of 1 barn (b) is equal to 10^{-24} cm^2 . Cross sections exist for each specific interaction, with the total interaction probability being the sum of all possible reactions. Cross

sections obtained from the evaluated nuclear data libraries are used to calculate the collapsed cross section value which is used in Eq. (2.7).

The classical estimate of the cross section for neutron reactions in a sharp-cutoff model with neutron energies in the MeV range is described by the interaction radius R_I , which is the sum of the effective radii of the incident neutron (r_n) and the target nucleus (r_T) [46]. This concept is shown in Fig. 3.2. The approximation states that if a neutron is within the interaction radius when encountering a target nucleus, the reaction may take place. Conversely, if the neutron falls outside the interaction radius, no reaction takes place. The probability of a specific interaction occurring has an energy dependence, as illustrated in Fig 3.1. The energy dependence is contingent on the target nuclide and specific reactions products.

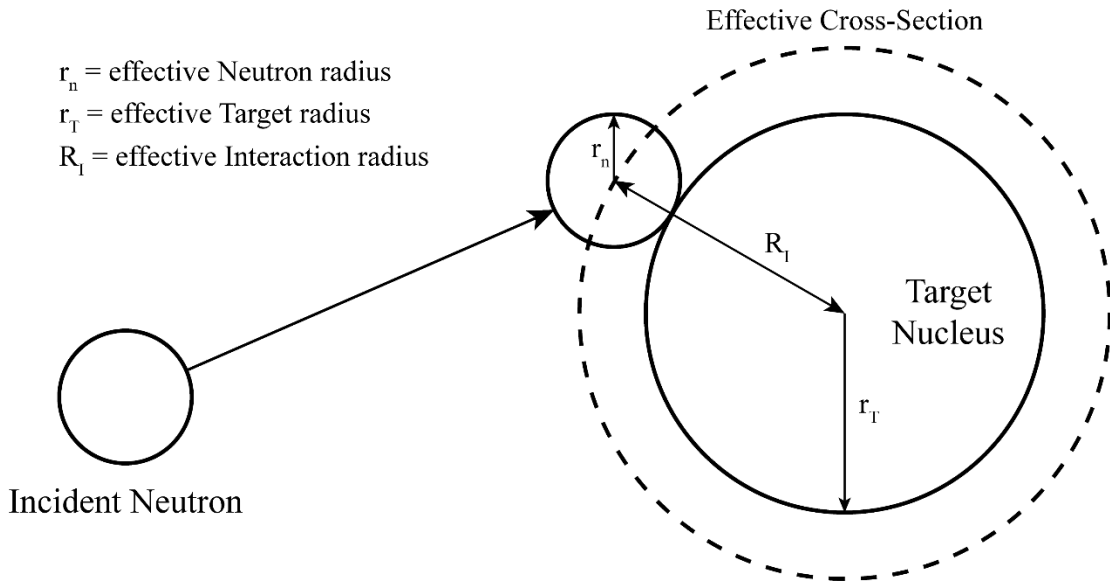


Figure 3.2 Effective cross section representation for a neutron reaction based on the effective interaction radius (R_I) for a target nucleus of radius r_T and incident neutron of radius r_n .

At low neutron energies, the cross section has a $1/v$ dependence, where v is the neutron velocity. At mid-range and higher energies, the cross section shows resonance peaks, which are increased reaction probability areas, consistent with the energy-level structure of the compound nucleus. Each resonance is described by the Breit-Wigner formula, given in Eq. (3.1):

$$\sigma_{\alpha\beta} = g_{\alpha}(J) \frac{\pi}{k_{\alpha}^2} \frac{\Gamma_{\alpha}\Gamma_{\beta}}{(E-E_r)^2 + (\Gamma/2)^2}, \quad (3.1)$$

where α and β refer to the entrance (projectile/target) and exit (ejectile/residual) channels of the reaction. The cross-section value ($\sigma_{\alpha\beta}$) is determined by a spin factor, $g_{\alpha}(J)$, that accounts for spin and angular momentum, the partial energy widths of the entrance and exit channels ($\Gamma_{\alpha}, \Gamma_{\beta}$), the wave number in the entrance channel (k_{α}), the energy of the incident particle (E) and resonance (E_r), and the energy width of the resonance (Γ) [46]. The partial energy widths in the entrance and exit channels are proportional to the decay probabilities of each channel, with the total decay width being proportional to the total decay probability.

Following the resonance range, the cross section continues to decrease with increasing neutron energy. These features of the cross section are displayed in Fig. 3.3 for the $^{58}\text{Fe}(n,\gamma)^{59}\text{Fe}$ reaction. Some reactions are threshold reactions, meaning that they require a minimum neutron energy before the reaction can take place. This is illustrated in Fig. 3.3 by the (n,p) and (n,2n) reactions on ^{58}Fe , which require the neutron energy to be above 5 or 10 MeV, respectively.

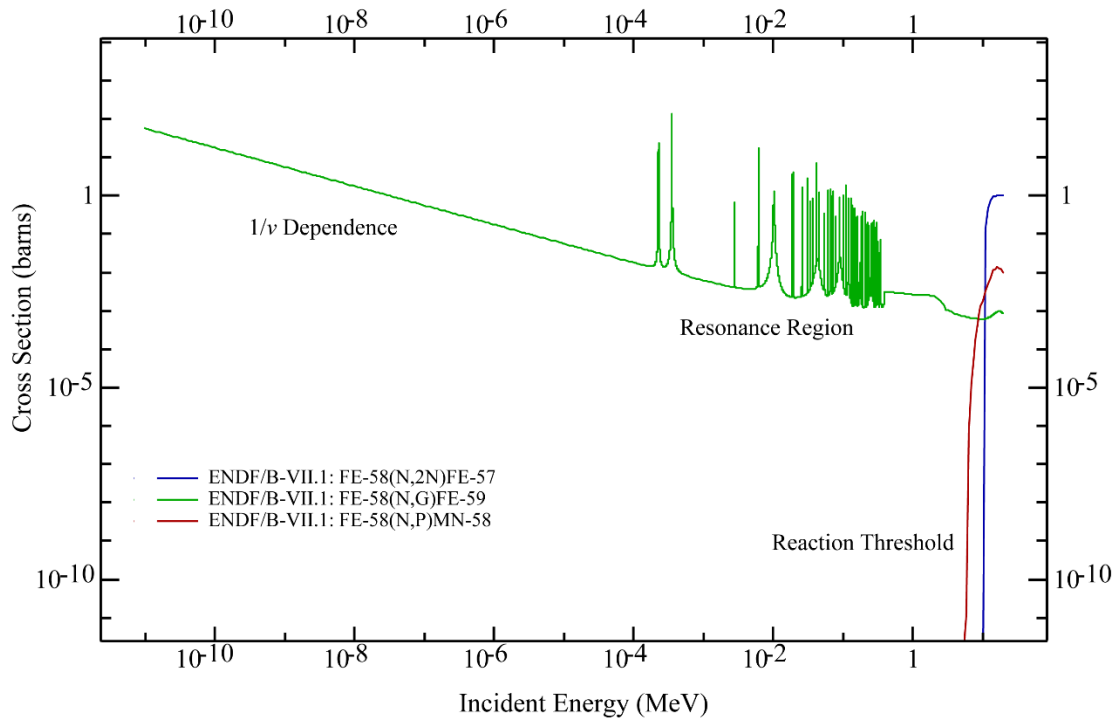


Figure 3.3 Energy dependence of the cross section for the (n,2n), (n, γ), and (n,p) reactions on ^{58}Fe from the ENDF/B-VII.1 library, showing the $1/v$ dependence at low neutron energies, resonance region at mid-range energies, and reaction thresholds at higher energies [72].

For monoenergetic neutrons, the cross-section value at the energy of incident neutron can be used in calculating reaction rates and activation product populations with Eq. (2.7). When neutron energy distributions are encountered, as is typically the case in most activation situations, the energy dependent cross section must be used. Activation calculations then require weighting of the multi-energy group cross sections available in the nuclear data to arrive at a 1-group collapsed cross section, given as $\bar{\sigma}$. The 1-group cross section is a weighted sum of the energy dependent cross section and energy dependent flux probability distribution according to Eq. (3.2):

$$\bar{\sigma} = \sum_i \frac{\Phi(E_i)\sigma(E_i)}{\Phi_T}, \quad (3.2)$$

where $\Phi(E_i)$ is the flux value at energy E_i , $\sigma(E_i)$ is the reaction cross-section value at E_i , and Φ_T is the total flux magnitude. Since the energy dependent cross section represents an interaction probability for a given reaction at a specific energy, the 1-group collapsed cross section is then a measure of the interaction probability for a specific reaction using a specific neutron distribution.

3.2 Nuclear Reactions

In the general sense, a nuclear reaction is the interaction of a nucleus and some other particle. For the general reaction of $A(a,b)B$, A is the target nucleus, a is the projectile, b is the ejectile, and B is the residual nucleus. Each reaction has an associated energy term as a product, the Q-value, which is the energy released or absorbed by the reaction. It is determined by the mass difference between the initial (m_A, m_a) and final (m_b, m_B) particles, multiplied by the speed of light squared as shown by Eq. (3.3):

$$Q = (m_A + m_a - m_b - m_B)c^2. \quad (3.3)$$

Reactions with negative Q-values require additional energy, since the Q-value is defined as a reaction product. These negative Q-value reactions are termed threshold reactions, like the (n,2n) and (n,p) reactions shown in Fig. 3.3, since the projectile must have a minimum energy for the reaction to proceed. As an example, the $^{58}\text{Fe}(n,p)^{58}\text{Mn}$ has a Q-value of -5.545(3) MeV [79]. Note that the Q-value is in the center-of-mass frame, so the threshold energy of the neutron in the lab-frame is positive and slightly

larger at 5.642(3) MeV. For the reaction to take place, the additional energy is supplied by the kinetic energy of the neutron. Reactions with positive Q-values result in energy release in addition to the production of particles. Positive Q-values, or projectile kinetic energies in excess of negative Q-values, can cause the reaction products to gain additional kinetic energy, or leave the residual nucleus in an excited state.

Many different combinations of b and B are possible, including multiple ejectiles. For this work, these combinations fall into 3 general classes of reactions: scattering reactions, direct reactions, and compound nucleus reactions. All reactions are subject to nuclear structure effects leading to cross-section resonances and Coulombic repulsion in the case of charged projectiles. In this work, the specific case of a neutron projectile impinging on a target nucleus is considered.

3.2.1 Scattering Reactions

Scattering reactions are the simplest class of reactions, involving no change in the identity of the initial and final particles. The general form of the reaction is then $A(a,a')A'$ where only the transfer of kinetic energy occurs. If total kinetic energy is conserved, then the reaction is defined as elastic scattering. When total kinetic energy is not conserved, the reaction is defined as inelastic scattering, $A' = A^*$, and the residual nucleus is left in an excited state.

For this work, scattering reactions for neutrons are important in the context of slowing the neutron down, a process called moderation. Moderation is utilized in nuclear reactors and ^3He neutron detectors to maximize neutron absorption.

Moderation of neutrons through scattering reactions is a significant precursor event to the other classes of reactions because of the energy dependence of the cross section. For some reactions, slower neutrons provide higher cross-section values. In others, the reaction may no longer be possible because the reaction threshold energy is no longer met. In either case, significant moderation of neutrons changes which reactions are possible for future neutron interactions.

3.2.2 *Direct Reactions*

A direct reaction occurs when the projectile interacts primarily on the surface of the target nucleus with a limited number of proton/neutrons (nucleons)[45, 46]. The result is an exchange of nucleons between the projectile and target nucleus. Direct reactions are more likely to occur for peripheral collisions, where the trajectory of the projectile is off-axis relative to the center of the target nucleus.

Direct reactions are further categorized as stripping, pickup, or breakup reactions. In any case, they require the projectile to have multiple nucleons. In a stripping reaction, the projectile loses a nucleon to the target nucleus. An example of this is the ${}^9\text{Be}(d,n){}^{10}\text{B}$ reaction, where a proton is transferred from the deuteron to the ${}^9\text{Be}$ target, resulting in the production of ${}^{10}\text{B}$ and a neutron. If the projectile gains one or more nucleons in the process, it is pickup reaction. An example of a pickup reaction is the ${}^{16}\text{O}(d,\alpha){}^{14}\text{N}$ reaction where the deuteron gains another proton and neutron to form an alpha particle. The third type of direct reaction is the breakup reaction, where the nucleons of the projectile become unbound. An example of a breakup reaction is the

${}^9\text{Be}(d,np){}^9\text{Be}$ reaction, resulting in the production of a proton and a neutron. Stripping and breakup reactions are common methods of neutron production, as is discussed in Sec. 3.3.

3.2.3 *Compound Nucleus Reactions*

A compound nucleus reaction occurs when the projectile binds to the target nucleus to create a one-body system [6, 46]. These reactions occur when the collision between the projectile and target nucleus is more central relative to the projectile path and center of the target nucleus. The higher degree of centrality causes the reaction energy to be shared between more nucleons. When an individual nucleon, or group of nucleons, has enough energy, it escapes the compound nucleus as the reaction ejectile. In some cases, the ejectile may be a photon rather than a single nucleon or group of nucleons.

Compound reactions from incident neutrons receive most of the attention because the neutron's lack of charge increases the availability of reaction channels at lower energies for a wider range of target nuclei. Figure 3.4 shows the reactions commonly encountered with available neutron sources, relevant to this work. Other combinations of nucleon emission are possible but require higher energy neutrons.

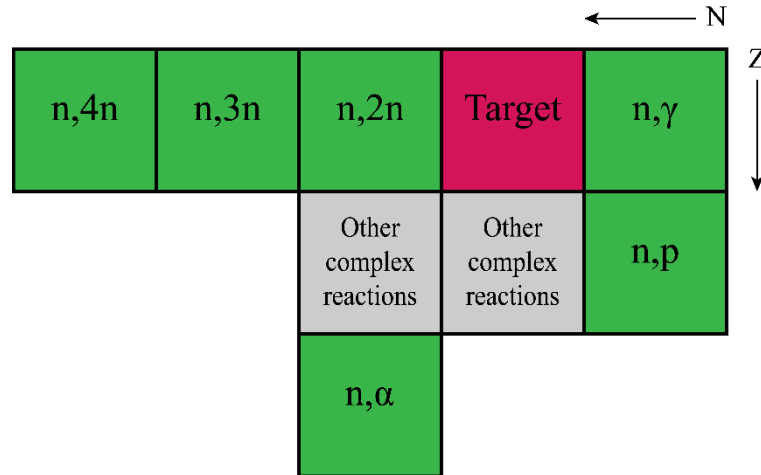


Figure 3.4 General reaction map for neutron induced reactions on a target nuclide. The (n,γ) , $(n,2n)$, $(n,3n)$, $(n,4n)$, (n,p) , and (n,α) reactions are the primary interest. Other complex reactions include (n,np) and $(n,2np)$, among others.

3.2.4 Nuclear Structure Effects

There are two components of nuclear structure that have pronounced effects on the various reactions: nuclear energy levels, and nuclear charge. When the reaction energy matches up with an excited state of the compound nucleus, the probability of reaction is greatly increased [6, 45, 46]. This increased reaction probability is called a resonance, identified in Fig. 3.3 and described by the Breit-Wigner formula in Eq. (3.1). The spacing of individual resonances is dependent on the energy level structure of the compound nucleus. Lower energy excited states are usually well-separated. The separation decreases with higher energy excited states, eventually resulting in a continuum of states where individual resonances can no longer be resolved. Resonance effects allow for reactions to be exploited in order to increase nuclide production or limit neutron populations. An example of the latter is the use of highly-absorbing neutron materials in reactor control rods [6, 45]. The large neutron capture cross section

of the control rod material, such as ^{113}Cd , allows the fission rate to be manipulated as desired.

The nuclear charge results in Coulombic effects when charged particles are involved as projectiles or reaction products. As shown by Eq. (3.4) for two point charges, Coulombic effects scale as the product of the Z numbers for the projectile/target, or ejectile/compound nucleus, and $1/r$, where r is the separation between particles:

$$V(Z_1, Z_2, r) = \frac{Z_1 Z_2 e^2}{4\pi\epsilon_0 r}. \quad (3.4)$$

In Eq. (3.4), e is the elementary charge and ϵ_0 is the permittivity in a vacuum. Equation (3.4) reduces to Eq. (3.5) to give V in MeV when r is in fm:

$$V(Z_1, Z_2, r) = \frac{1.44Z_1 Z_2}{r}. \quad (3.5)$$

The result is increased energy requirements for reactions to take place. The work presented in the remaining chapters focuses on residual nuclei from neutron interactions, rather than charged projectiles/ejectiles, so the effect of nuclear charge is limited to reducing the availability of charged particle emission channels for activation products.

3.3 *Neutron Sources*

The uncharged nature of the neutron makes it an excellent projectile for initiating nuclear reactions. The lack of charge eliminates the Coulomb barrier,

reducing energy requirements for reaction thresholds. There are several mechanisms for neutron production, all providing different neutron energy distributions. Common production mechanisms include fission, decay-induced reactions, and accelerator-based reactions using charged particle projectiles. The most significant difference between the production mechanisms is that neutron production from fission and decay-induced sources is isotropic, while accelerator sources are forward-peaked.

Fission, whether through spontaneous decay or induced through reactions, results in the production of multiple neutrons per fission event. The majority of these neutrons have an energy of less than 1 MeV but can extend up near 10 MeV depending on the fissioning nuclide. The most common spontaneous fission source is ^{252}Cf with a neutron yield of $0.116 \text{ n s}^{-1} \text{ Bq}^{-1}$, due to its relatively high yield of neutrons per fission and spontaneous fission probability of approximately 3% [58, 80]. Neutron energy distributions from fission in nuclear power reactors may resemble the spontaneous fission distribution or may be shifted significantly to lower energies, depending on the reactor design.

Decay-induced reactions involve the production of an alpha particle (α) or high-energy gamma ray (γ) from a radionuclide source, which then reacts with a target material to produce neutrons. Beryllium is the preferred target material for both the (α, n) and (γ, n) reactions because of the Q-values involved in each situation [58]. The (α, n) and (γ, n) reactions have Q-values of +5.71 MeV and -1.666 MeV, respectively. The next most favorable values are +2.2 MeV for ^{13}C with the (α, n) reaction, and -2.226 MeV for ^2H with the (γ, n) reaction. Neutron yields and energy distributions for decay-induced reactions vary greatly depending on the target material and decaying

nuclide. The (α ,n) reactions on ^9Be , $^{10, 11}\text{B}$, ^{19}F , ^{13}C , and ^7Li provide neutron distributions in the 1-10 MeV range. Conversely, the majority of the (γ ,n) reactions on ^9Be or ^2H targets lead to neutron energies less than 1 MeV.

Neutron production from accelerated charged particles is practically limited to protons and deuterons as projectiles since they have the lowest possible Coulomb barriers. The energy requirements of other charged projectiles make them less desirable as neutron sources. Deuterium-deuterium (D-D) and deuterium-tritium (D-T) reactions are the most common reactions because the required acceleration potential for deuterons is only a few hundred kilovolts [58]. The Q-values for the D-D and D-T reactions are +3.269 MeV and +17.59 MeV, respectively. The resulting neutron energies are approximately 3 MeV for the D-D reaction and 14 MeV for the D-T reaction, although the specific neutron energy varies with the emission angle and the spatial distribution is slightly forward peaked due to conservation of momentum.

Larger accelerator facilities are able to produce neutrons through (p,n) and (d,n) reactions on slightly heavier nuclei. The most common reaction in this situation is the $^9\text{Be(d,n)}^{10}\text{B}$ reaction with a Q-value of +4.362 MeV. When incident deuterons in the MeV range are used, the resulting neutron spectrum spatial distribution is heavily forward peaked. Another difference between sources is that neutron production from D-D and D-T reactions is much closer to monoenergetic, while the (d,n) reaction on ^9Be produces a broad spectrum of neutron energies dependent on the projectile energy and target dimensions.

Each of the neutron production methods provides different neutron energy distributions. For the purposes of this work and nuclear forensic analysis, the neutron

energy spectra from fission and the (d,n) reaction are of most interest. The fission spectrum is characteristic of special nuclear material and single-stage nuclear weapons. The (d,n) reaction on ^9Be can be manipulated to produce a neutron energy distribution that includes both fission and D-T neutron spectra, intended to mimic a two-stage nuclear weapon.

3.3.1 The Flattop Critical Assembly

The Flattop critical assembly is the neutron source chosen to provide fission spectrum neutrons. It is one of several assemblies used to perform benchmark experiments for nuclear data and criticality safety [81]. The Flattop critical assembly consists of a natural uranium sphere with interchangeable U or Pu cores, allowing for different neutron spectra to be obtained [82].

The assembly has a bore through the central horizontal axis to allow for sample irradiations. Due to the geometry of the assembly, the neutron energy distribution varies with position along the horizontal axis. The work presented in later chapters employs a ^{235}U core and irradiation occurs at the center point of the sample bore within the assembly. Neutrons are produced as the assembly is brought up to a critical state and maintained during the irradiation. A simulated neutron energy probability distribution of the Flattop flux, based on a Monte Carlo model, is presented in Fig. 3.5 along with the cumulative probability distribution. A description of the Monte Carlo model is available in App. B. The most probable energies from the Flattop distribution

span 0.1-4 MeV. However, approximately 60% of all neutrons have an energy less than 1 MeV, while the remainder have energies from 1-20 MeV.

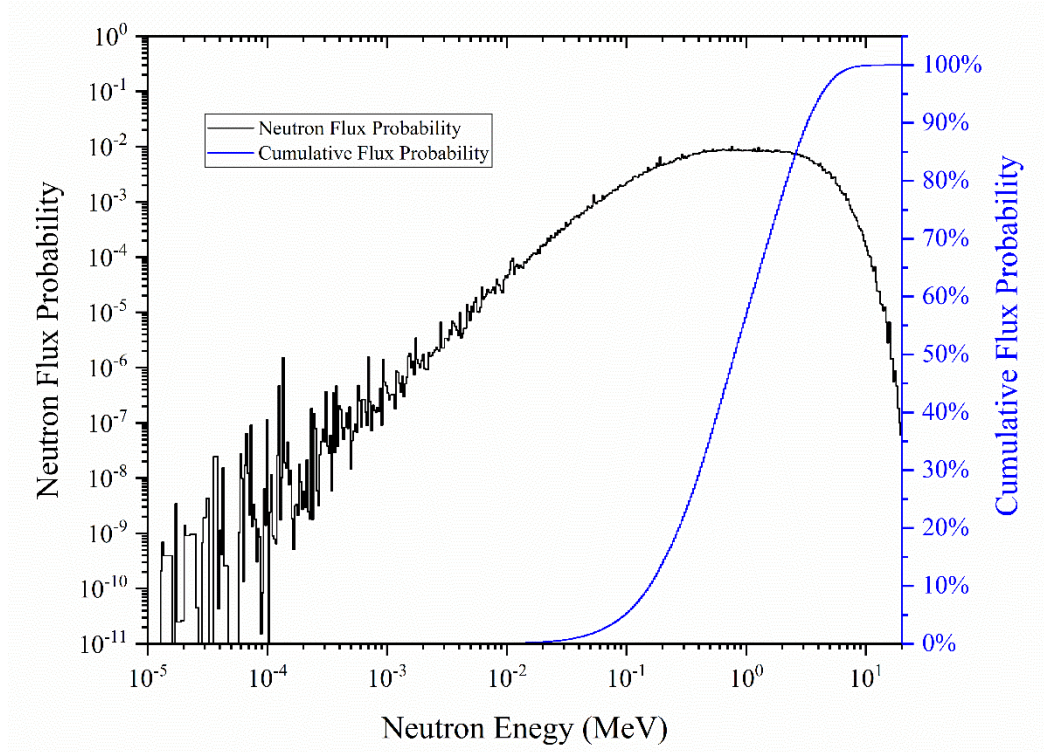


Figure 3.5 The Monte Carlo model energy dependent neutron flux probability (black) and cumulative flux probability (blue) distributions for the Flattop critical assembly at the center position of the irradiation bore.

3.3.2 The UC Davis ^9Be Converter

The ^9Be neutron converter at the University of California-Davis (UC Davis) uses a 76-inch cyclotron to accelerate deuterons and exploit the d+Be family of reactions. Reactions include the (d,n) stripping reaction and the (d,np) breakup reaction, along with the (d,xn) and (d,2np) reactions at higher energies [53, 83]. The resulting neutron spectrum is peaked in the forward direction, supplying a more efficient neutron

source based on the number neutrons on target when compared to isotropic neutron sources.

The work presented in later chapters uses a deuteron beam of 30 MeV, with a 10 μ A beam current. This results in a neutron spectrum that has characteristics of D-T fusion as well as fission. A Monte Carlo model of the UC Davis neutron converter is discussed in App. B. The simulated neutron energy probability distribution for 30 MeV deuterons is shown in Fig. 3.6 along with the cumulative probability distribution. The simulated neutron energy distribution shows that the most probable neutron energy is near 15 MeV. The cumulative distribution shows that only 10% of neutrons have energies less than 10 MeV, a significant change from Flattop. Also, approximately 60% of the neutrons from UC Davis have energies in the 10-20 MeV range. The UC Davis distribution shows a tailing off towards low neutron energies, below a few MeV, similar to what is seen with Flattop. However the Flattop distribution extends to lower neutron energies than the UC Davis distribution, while the upper energy portion of UC Davis extends further than the fission spectrum of Flattop. These differences in the neutron energy distributions will present different reaction channels for neutron activation.

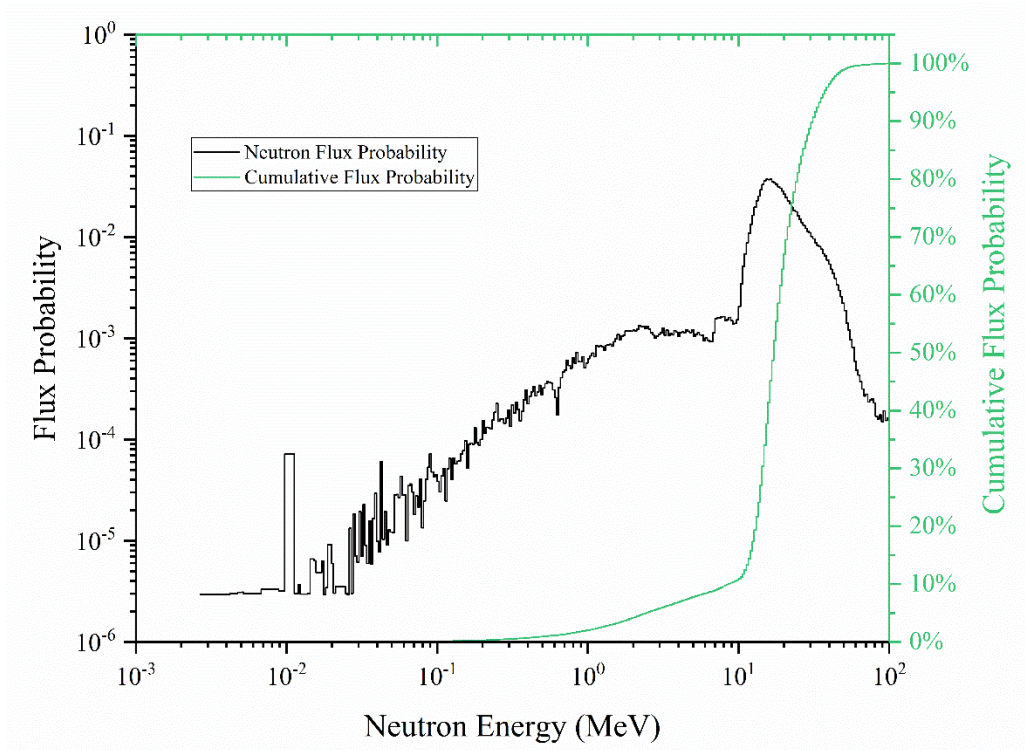


Figure 3.6 The Monte Carlo model energy dependent neutron flux probability (black) and cumulative probability distributions (green) for the UC Davis d+Be converter when using 30 MeV deuterons.

3.4 Computation Codes

The study of radiation interactions presents unique safety and engineering issues when performing experiments. Because of this, it is often more practical to simulate radiation interactions using various computation and transport codes. These codes are either stochastic or deterministic in their approach. Stochastic codes, or Monte Carlo codes, use a random approach to radiation interactions to arrive at the final solution to a problem. Individual particle histories are statistically sampled, based on the problem physics and available nuclear data, for the interactions that occur during the “life” of the particle. Many individual particle histories are then used to infer the

average behavior of the system. Examples of commonly used stochastic codes are the Monte Carlo N-Particle radiation transport code (MCNP) and the GEANT4 toolkit [84, 85]. The random approach of these codes offers more flexibility in the variety of problems that can be solved.

Deterministic codes explicitly solve for the solution to a problem, rather than rely on the randomness of individual interactions to infer the result. In deterministic codes, the average behavior of the system is determined by the parameter values and initial conditions. A complete mathematical description of the system is required. In contrast, stochastic codes do not have the same requirement. This difference leads to greater flexibility of stochastic codes, while deterministic codes usually have very specific applications. Examples of deterministic codes are FISPACT-II and the ORIGEN module of SCALE-6.2 [86, 87].

The work presented in the chapters that follow uses both the deterministic FISPACT-II and stochastic MCNP codes to explore activation scenarios and subsequent gamma-ray spectroscopy measurements. Neutron activation simulations are performed using hand calculations or FISPACT-II for the different neutron sources. Hand calculations were used when the number of activation products considered was small and predetermined. FISPACT-II was used to explore the entire activation network. Gamma-ray spectroscopy measurements are simulated using a high-purity Ge detector model in MCNP. Neutron production for the UC Davis and Flattop sources is also modeled using MCNP. Descriptions of the models are provided in App. B. The Monte Carlo process of MCNP is described in App. C. The combination of codes enables simulation of the entire process of neutron activation, decay, and measurement.

Chapter 4: Validation of a Monte Carlo HPGe Detector Model Against Irradiated Foil Gamma-Ray Spectroscopy Measurements³

The work presented here is adapted from [43]. It describes the validation of a high-purity germanium detector model written in the Monte Carlo N-Particle radiation transport code (MCNP). Additional details of the detector model and an example input file are provided in App. B. The detector model is validated against irradiated foil experiments which used the d+Be converter neutron source from the Crocker Nuclear Laboratory at the University of California-Davis. The activation product ratio equation expressed according to Eq. (4.3) is derived in App. A.

4.1 Introduction

Gamma-ray spectroscopy is a non-destructive, passive analysis technique for the identification and quantification of radionuclides. High-purity germanium (HPGe) detectors have superior resolution compared with other semiconductors or scintillation detectors [88].

³ Reprinted by permission from Springer Nature: Springer Journal of Radioanalytical and Nuclear Chemistry, J.J. Goodell, C.M. Egnatuk, S.W. Padgett, B.B. Bandong, K.E. Roberts, A.C. Mignerey, Validation of a Monte Carlo HPGe detector model against irradiated foil gamma-ray spectroscopy measurements, J. Radioanal. Nucl. Chem. 314:1793-1802. Copyright 2017. This work was performed under the auspices of the U.S. Department of Energy by Lawrence Livermore National Laboratory under Contract DE-AC52-07NA27344.

Simulations enable researchers to explore different scenarios and plan future experiments without wasting resources. For gamma-ray spectroscopy measurements, simulations can help identify interferences that may otherwise go unnoticed. Simulations can also predict minimum activity levels required to confidently quantify radionuclides. Knowing the required minimum activity at the time of measurement is needed to define irradiation conditions for activation experiments as well as place constraints on decay times for measurements. When the experiment is accurately modeled, deviations between the simulation and experiment data can identify problems with established databases and physics models.

The Monte Carlo method is employed when simulating radiation interactions, typically by using either the Monte Carlo N-Particle radiation transport code (MCNP) or the Geant4 toolkit [84, 85]. Previous work on HPGe detector modeling focuses on characterizing the crystal's dead layer and the full energy photopeak efficiency. Accurately modeling detector photopeak efficiency is straightforward if accurate physical characteristics of the detector are available [89–94]. Accurate representation of the crystal's dead layer improves simulated photopeak efficiency. In the case where nominal manufacturer's uniform specifications are used in the detector model, simulated photopeak efficiency deviates from experiment values. The magnitude of deviation is dependent on the dead layer of the actual crystal being modeled and how it differs from manufacturer specifications. This study uses MCNP version 6.1 (MCNP6.1) to develop a HPGe model based on the manufacturer's specifications. To evaluate model performance, activation product ratios calculated from simulated

spectra are compared with activation product ratios calculated from HPGe measurements on irradiated Fe, Ni, Cr, and stainless steel foils.

This study validates the HPGe model against experiment data rather than standard radionuclide sources for two reasons. First, standard sources are often simple or limited in the number of radionuclides. In the case of multi-radionuclide sources, components are chosen to limit interferences. This feature makes standard sources excellent for calibrating systems, but lacks the complexity often seen in real applications. Using experiment data provides the opposite scenario with the potential to have many interferences. This study investigates the choice of activation product ratios and the ability of the MCNP6.1 HPGe model to predict experiment results. Second, standard sources have significant known activities, meaning that all peaks of the source will be seen experimentally. This luxury is not afforded to real applications where decay times can significantly affect results because of multiple radionuclides with a range of half-lives.

4.1.1 Activation Product Ratios

The use of high-yield neutron sources or long irradiation times complicates the choice of activation product ratios. Both conditions provide a greater number of neutrons on target. More neutrons on target increases the potential for successive activations, an issue more prevalent when using long irradiation times. In some cases, the secondary activation product may also be produced through a different primary reaction. The successive activation problem is an issue for long irradiation times when

radionuclides having substantial half-lives are present. Successive activations also illustrate how cross sections must be accounted for when determining the source of a radionuclide. Additionally, comparison of activation results between experiments and simulations can uncover problems with nuclear data and accepted physics models.

Another complication due to long irradiation times is the decay of activation products during irradiation. If the primary activation product has a short half-life relative to its daughter product, the daughter will begin to accumulate during irradiation. As the daughter product accumulates, activation of the daughter nuclide becomes more probable during the remaining irradiation period. At the end of irradiation, the original target nuclide has led to the production of several different nuclides.

The activation product ratios chosen for this study focus on the irradiation of Fe, Ni, Cr, and stainless steel (SS) foils. Stainless steel type AISI 304 was used since it is very common and the major components are Fe, Ni, and Cr [95]. Activation products in this study result from six primary neutron capture reactions – (n,γ) , (n,α) , (n,p) , $(n,2n)$, $(n,3n)$, and $(n,4n)$. The ratios and production reactions are given in Table 4.1, along with gamma-ray energies and intensities [80]. When a primary activation product was not detected experimentally, a daughter nuclide produced through electron capture (E.C.) or positron emission (β^+) was used in the ratio. Ratios were chosen to represent single production pathways where possible. Ratios in this study used the highest intensity gamma-ray energy. Other gamma-ray peaks were considered if there were interferences to the primary line or the first-choice energies performed poorly. The definition of poor performance is a gamma-ray peak that has an irregular shape or a

low signal-to-noise ratio. These characteristics reduce accuracy and precision in calculated activation product ratios.

Table 4.1 Activation product ratios, reactions, and gamma rays used in analysis [80]

Foil	Ratio	Reaction	E_γ (keV)	Intensity (%)
Fe	$^{54}\text{Mn}/^{56}\text{Mn}$	$^{54}\text{Fe}(n,p)^{54}\text{Mn}$	834.848	99.976
		$^{56}\text{Fe}(n,p)^{56}\text{Mn}$	846.7638; 1810.726	98.85; 26.9
	$^{51}\text{Cr}/^{54}\text{Mn}$	$^{54}\text{Fe}(n,\alpha)^{51}\text{Cr}$	320.0824	9.91
		$^{54}\text{Fe}(n,p)^{54}\text{Mn}$	834.848	99.976
	$^{54}\text{Mn}/^{52}\text{Mn}^a$	$^{54}\text{Fe}(n,p)^{54}\text{Mn}$	834.848	99.976
		$^{54}\text{Fe}(n,3n)^{52}\text{Fe};$ $\text{E.C.}/\beta^+$ to ^{52}Mn	1434.06	98.2
Ni	$^{58}\text{Co}/^{60}\text{Co}$	$^{58}\text{Ni}(n,p)^{58}\text{Co}$	810.7593	99.45
		$^{60}\text{Ni}(n,p)^{60}\text{Co}$	1173.228; 1332.492	99.85; 99.9826
	$^{56}\text{Co}^a/^{58}\text{Co}$	$^{58}\text{Ni}(n,3n)^{56}\text{Ni};$ $\text{E.C.}/\beta^+$ to ^{56}Co	846.770; 1238.288	99.9399; 66.46
		$^{58}\text{Ni}(n,p)^{58}\text{Co}$	810.7593	99.45
	$^{57}\text{Ni}/^{58}\text{Co}$	$^{58}\text{Ni}(n,2n)^{57}\text{Ni}$	1377.63	81.7
		$^{60}\text{Ni}(n,4n)^{57}\text{Ni}$ $^{58}\text{Ni}(n,p)^{58}\text{Co}$	810.7593	99.45
Cr	$^{48}\text{Cr}/^{51}\text{Cr}$	$^{50}\text{Cr}(n,3n)^{48}\text{Cr}$	308.24	100
		$^{50}\text{Cr}(n,\gamma)^{51}\text{Cr}$	320.0824	9.91
		$^{52}\text{Cr}(n,2n)^{51}\text{Cr}$		
		$^{53}\text{Cr}(n,3n)^{51}\text{Cr}$ $^{54}\text{Cr}(n,4n)^{51}\text{Cr}$		
	$^{48}\text{V}^a/^{51}\text{Cr}$	$^{50}\text{Cr}(n,3n)^{48}\text{Cr};$ $\text{E.C.}/\beta^+$ to ^{48}V	983.525; 944.130	99.98; 7.870
		$^{50}\text{Cr}(n,\gamma)^{51}\text{Cr}$ $^{52}\text{Cr}(n,2n)^{51}\text{Cr}$ $^{53}\text{Cr}(n,3n)^{51}\text{Cr}$ $^{54}\text{Cr}(n,4n)^{51}\text{Cr}$	320.0824	9.91

^aDenotes nuclides that are daughters of primary activation product reactions

Pathways for the six primary reactions on Cr are described by the activation map shown in Fig. 4.1. Nuclides are shaded based on their role during the activation

and decay processes. The lines leaving target nuclides represent a specific reaction, determined by the origin of the line. Looking at Fig. 4.1, ^{48}Cr is a direct, single pathway product, ^{48}V is the daughter of ^{48}Cr , and ^{51}Cr is a multiple pathway product. ^{51}Cr is produced through 4 primary reactions – $^{50}\text{Cr}(n,\gamma)^{51}\text{Cr}$, $^{52}\text{Cr}(n,2n)^{51}\text{Cr}$, $^{53}\text{Cr}(n,3n)^{51}\text{Cr}$, and $^{54}\text{Cr}(n,4n)^{51}\text{Cr}$. In the case of SS, ^{51}Cr is also produced through the $^{54}\text{Fe}(n,\alpha)^{51}\text{Cr}$ reaction, making it complicated to determine the source of ^{51}Cr . Time also plays a role, illustrated by the relationship between ^{48}Cr and ^{48}V . ^{48}Cr decays through electron capture, or positron emission, to ^{48}V with a half-life of 21.56 h. Long decay times from the end of irradiation lead to the buildup of ^{48}V . Similar situations and compound reaction pathways involving successive activations may introduce interferences and obscure the true source of a given nuclide. Therefore, activation product ratios must be chosen carefully, especially for multi-element samples such as SS.

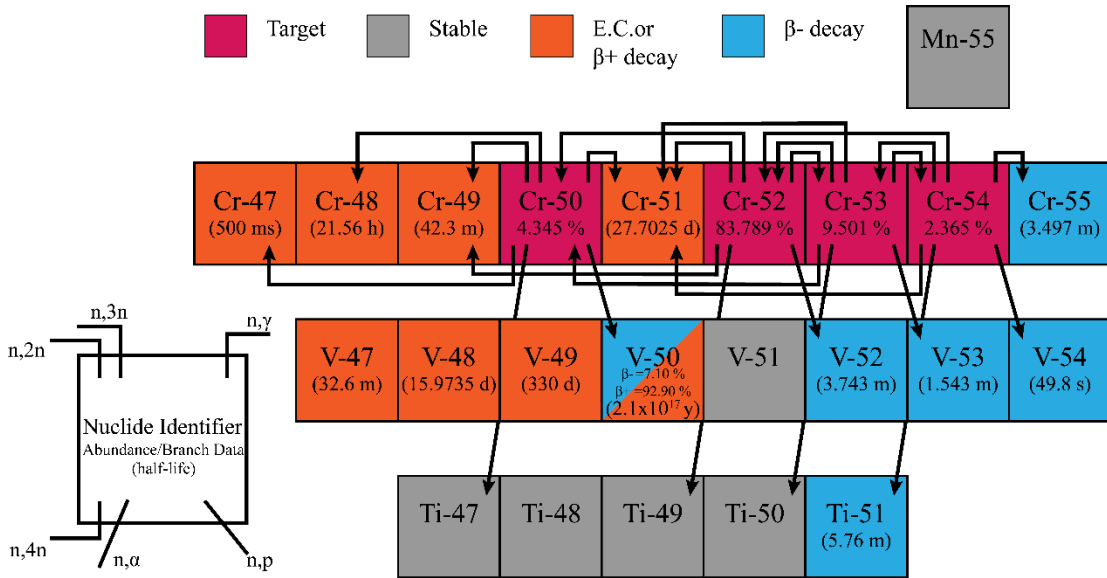


Figure 4.1 Activation Map for Cr showing the 6 primary reaction pathways [80].

4.2 *Experimental*

4.2.1 *Foil Irradiations*

The experiment data is from foil irradiations using the 76 inch cyclotron at the University of California-Davis. The neutron source for these experiments consisted of a Be cylinder, employing the ${}^9\text{Be}(d,n){}^{10}\text{B}$ reaction, with the deuteron beam supplied by the cyclotron. Prior experiments and mathematical models show that this method produces a high total neutron fluence with significant portion of the fluence having energies slightly less than one half of the deuteron beam energy [83, 96]. Figure 4.2 shows the measured neutron energy distribution at the University of California-Davis cyclotron [96]. The neutron spectrum, normalized for energy grouping and integrated beam current, shows a maximum fluence under 5 MeV as well as a significant plateau from 10-15 MeV. Past 15 MeV, the neutron spectrum tapers off to a maximum energy near 30 MeV.

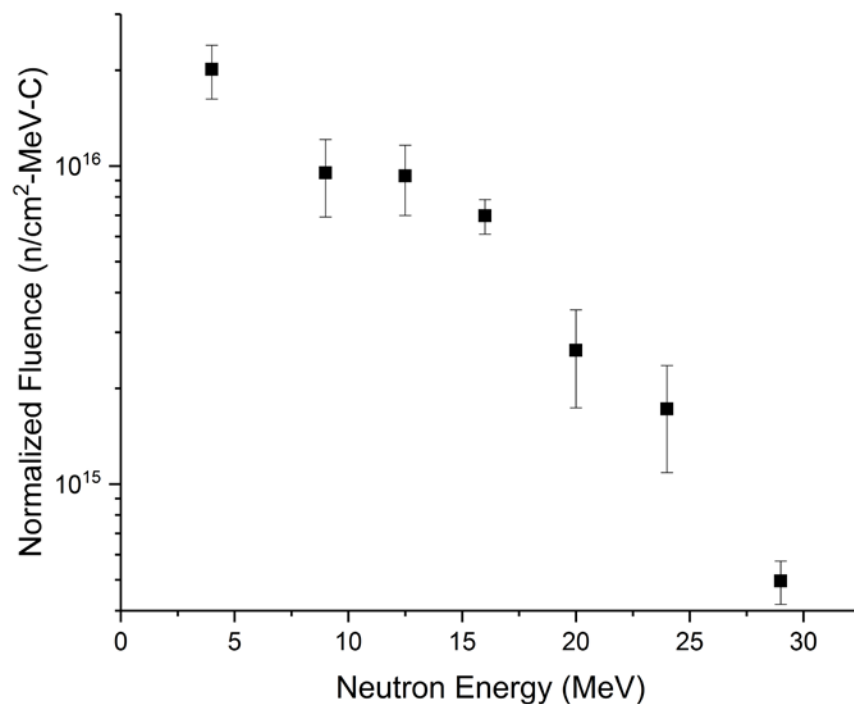


Figure 4.2 Neutron energy spectrum resulting from the ${}^9\text{Be}(d,n){}^{10}\text{B}$ reaction at the University of California-Davis cyclotron [96].

This study used data from four different irradiations, with each irradiation using a deuteron beam energy of 30 MeV and beam current of 10 uA. Irradiation time was 3 h for Run 1, 4 h for Run 2, and 7 h for Run 3 and Run 4. Decay times for samples ranged from 1.79 d to 16.64 d from the end of irradiation. Single element target foils were obtained from Shieldwrx while SS foils were obtained from Goodfellow [97, 98]. Shieldwrx foils were greater than 99.9% pure. The composition of the SS foil, as determined by ICP-MS analysis, was 71.21% Fe, 18.39% Cr, 8.05% Ni, 1.81% Mn, and 0.54% Cu, which is consistent with the manufacturer's analysis. Samples were counted using different HPGe detectors for a minimum of three independent counts. Counting times were adjusted as needed to ensure good statistics for the different nuclides under investigation. The HPGe detectors used were ORTEC GEM series p-

type coaxial detectors with relative efficiencies, against a 3 in by 3 in NaI crystal at 1332 keV, ranging from 12.3% to 37.0%. All counts used 4096 channels with a gain of 0.500 keV per channel. Experiment results from HPGe measurements are reported as atoms at t=0, end of irradiation, for each detected nuclide and are presented in Table 4.2 and Table 4.3.

Table 4.2 HPGe measurement results for Fe, Ni, and Cr foils, as atoms at t=0 with 1-sigma uncertainty (ND: not detected)

Foil	Nuclide	Run 1	Run 2	Run 3	Run 4
Fe	⁵¹ Cr	6.56(2)E+8	1.32(4)E+9	2.17(7)E+9	
	⁵² Mn	2.08(6)E+7	3.69(11)E+7	6.35(19)E+7	
	⁵⁴ Mn	5.92(18)E+9	1.12(3)E+10	1.89(6)E+10	
	⁵⁶ Mn	1.36(4)E+10	6.34(19)E+10	3.3(3)E+10	
Ni	⁵⁴ Mn	7.7(25)E+8	1.3(1)E+9	8.7(3)E+9	
	⁵⁶ Co	4.0(6)E+8	5.75(23)E+8	3.95(12)E+9	
	⁵⁷ Co	3.51(11)E+10	6.17(19)E+10	3.86(16)E+11	
	⁵⁸ Co	4.82(14)E+10	8.05(24)E+10	5.23(16)E+11	
	⁶⁰ Co	2.9(13)E+9	6.2(6)E+9	3.93(12)E+10	
	⁵⁷ Ni	2.39(7)E+9	4.07(12)E+9	2.60(8)E+10	
Cr	⁴⁶ Sc			ND	2.33(7)E+8
	⁴⁸ Sc			ND	1.56(5)E+8
	⁴⁸ V			3.89(12)E+8	4.59(14)E+9
	⁴⁸ Cr			7.8(12)E+6	9.1(7)E+6
	⁵¹ Cr			6.27(19)E+11	7.21(22)E+11
	⁵² Mn			ND	1.84(6)E+7

Table 4.3 HPGe measurement results for SS foil, as atoms at t=0 with 1-sigma uncertainty

Nuclide	SS
²⁴ Na	4.81(16)E+7
⁴⁸ V	2.26(10)E+7
⁵¹ Cr	1.493(8)E+11
⁵² Mn	2.38(7)E+8
⁵⁴ Mn	9.70(4)E+10
⁵⁶ Mn	1.4(5)E+11
⁵⁹ Fe	4.05(7)E+8
⁵⁵ Co	1.0(8)E+7
⁵⁶ Co	7.47(9)E+8
⁵⁷ Co	7.35(3)E+10
⁵⁸ Co	9.35(14)E+10
⁶⁰ Co	7.43(15)E+9
⁵⁶ Ni	2.1(4)E+7
⁵⁷ Ni	4.58(6)E+9
⁹⁹ Mo	6.97(17)E+8
^{99m} Tc	1.1(5)E+10

4.2.2 Simulation

The MCNP6.1 model consists of the detector capsule and the sample container. The detector capsule contains the Ge crystal, Al mounting cup, and Al housing. Simulations were run with and without a shield chamber to determine its effect on quantitative results. Other components, such as the sample platform and associated electronics, are not modeled. The HPGe model is based on an ORTEC GEM30P4-70 p-type coaxial detector having 37.0% relative efficiency. Detector component specifications were obtained from the ORTEC product specification sheet. The crystal has a length of 6.10 cm and a diameter of 5.90 cm. The inner bore has a diameter of 0.90 cm and a depth of 4.70 cm. Corrections for the bulletization of the crystal were not included in the model. The crystal is capped by 0.003 cm layers of Al and Mylar.

The gap from the crystal cap to front of the capsule is 0.3 cm. The distance from the source center of mass to the face of the detector capsule is 10.0 cm. The interior of the capsule and the inner bore is under vacuum. The outer dead layer is 0.07 cm thick, while the inner dead layer is 3×10^{-5} cm thick. The sample is modeled as a polyethylene vial and cap containing 10 mL of water. Materials used in the simulation include water, air, natural Ge, natural Al, and polyethylene, as described by the Pacific Northwest National Laboratory (PNNL) materials compendium [99]. A rendering of the MCNP detector geometry is presented in Fig. 4.3.

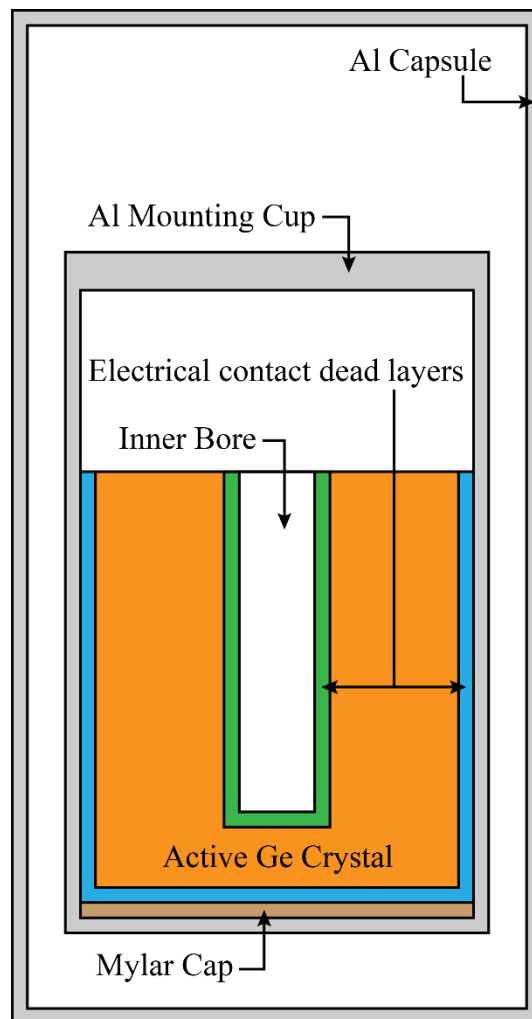


Figure 4.3 Representation of the simulated HPGe detector geometry.

A cylindrical shield chamber was included in some simulations to determine how it affects results. The shield chamber was comprised of natural Pb, with natural Cu and Cd liners, and a simple carbon steel cover as defined by the PNNL Compendium [99]. The cylindrical Pb layer was 9.525 cm thick, while the liners were 0.0793 cm thick, and steel cover was 0.635 cm thick. The Pb endcaps were 10.16 cm thick. The inner diameter of the shield chamber was 25.4 cm and the inner height was 38.1 cm.

Detector response was incorporated using the Gaussian energy broadening (GEB) tally treatment option for the F8 pulse-height tally [84, 100]. Simulated counts are tallied by sampling from a Gaussian based on the energy of the photon, having a full width at half max (FWHM) described by Eq. (4.1):

$$FWHM = a + b\sqrt{E + cE^2} \quad (4.1)$$

where E is the energy of the photon in MeV. FWHM parameters a , b , and c have units of MeV, $\text{MeV}^{1/2}$, and MeV^{-1} . Parameters for the GEB option were extracted from experiment data collected on the GEM30P4-70 detector that the model is based on. This was done by fitting Eq. (4.1) to FWHM data plotted as a function of photopeak energy. Fig. 4.4 shows the experiment data and parameter fit using Eq. (4.1). The fit gives a R-squared value of 0.9907, using 310 data points, and errors in parameter values are less than 5%.

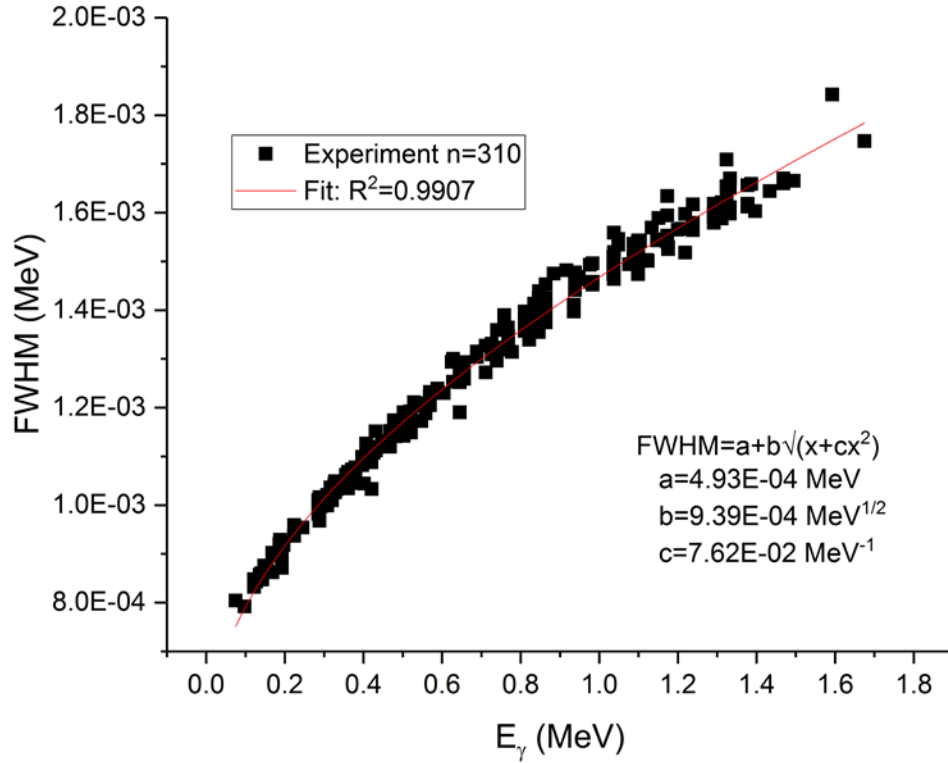


Figure 4.4 FWHM parameter fit based on experiment data, n=310. Errors in parameter values are less than 5%.

Model full energy photopeak (FEP) efficiency (ε) was simulated by using a monoenergetic photon source, ranging from 50 keV to 2000 keV, and calculating the ratio of counts in the photopeak to the total number photons used in the simulation. The simulated FEP efficiency data was fit using a 4th degree natural log polynomial, as described by Eq. (4.2):

$$\ln(\varepsilon) = \sum_{i=0}^n a_i \left[\ln\left(\frac{E_\gamma}{E_{ref}}\right) \right]^i \quad (4.2)$$

with E_γ in keV and E_{ref} equal to 1 keV. Simulated FEP efficiency data is plotted in Fig. 4.5 with experiment data from counts on the detector being modeled.

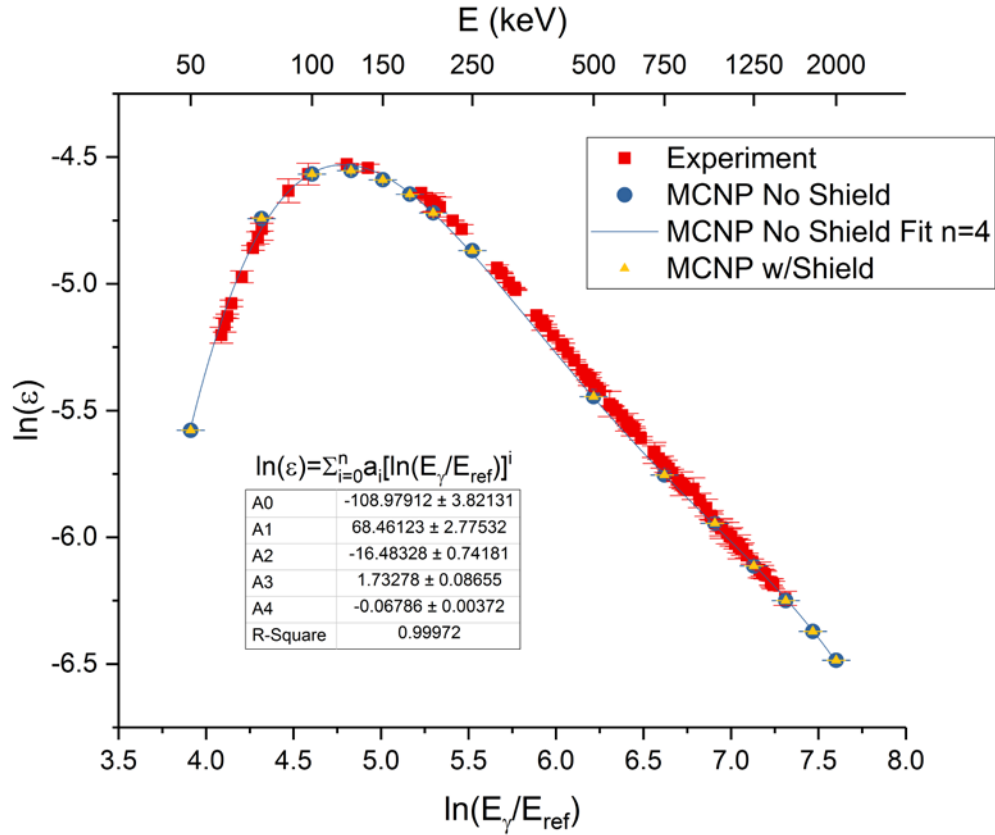


Figure 4.5 Full energy photopeak efficiency comparison between experiment data (red), simulation without shield (blue), and simulation with shield (yellow). Simulated data is fit with a 4th degree natural log polynomial and $E_{ref} = 1$ keV. Error bars for simulated points are statistical error when running 10^9 particles.

The fit from Eq. (4.2) gives a R-squared value of 0.99972 for the simulated data without the shield chamber. The MCNP6.1 model without the shield gives an equivalent relative efficiency of about 42% at 1332 keV. Since there is little difference in efficiency between simulations with and without the shield, computation time can be significantly reduced by proceeding without the shield.

All simulations were run by generating 10^9 photons as the source particles, emitted isotropically from random positions within the sample cell. A low energy cutoff

was set to 50 keV to save on computation time. The MCPLIB84 was used for photon interactions while the eI03 library was used for electron interactions.

The photon source for each simulation was calculated based on the experiment results given in Table 4.2 or Table 4.3. A decay time of 2 d was chosen to approximate the earliest experiment measurement. Activities for nuclides listed in Tables 4.2 and 4.3 were calculated based on the 2 d decay period and the experimentally determined number of atoms at the end of irradiation. Corrections were made to nuclides that are part of multi-step decay chains to account for the decay from parent to daughter. Source photon probabilities were calculated by multiplying the nuclide activity at 2 d by the gamma-ray emission probability (intensity) for each gamma ray of a given nuclide. Nuclear data was taken from the National Nuclear Data Center [80]. Simulated counts were tallied using the F8 tally with the GEB treatment. The energy bin structure for tallying counts was constructed to match the experiment counts, consisting 4096 bins spaced at 0.500 keV per bin.

Activation product ratios of atoms at $t=0$ were calculated using Eq. (4.3):

$$\frac{N_1}{N_2} = \frac{A_1 \lambda_2 \varepsilon_2 P_{\gamma 2}}{A_2 \lambda_1 \varepsilon_1 P_{\gamma 1}} e^{t(\lambda_1 - \lambda_2)} \quad (4.3)$$

where I and 2 are nuclide identifiers, N is the number of atoms at $t=0$, A is the peak area calculated using the specified gamma ray, λ is the decay constant, ε is the FEP efficiency calculated using Eq. (4.2), P_{γ} is the intensity of the specified gamma ray, and t is the decay time in minutes from the end of irradiation. Simulated peak areas were calculated using the PeakEasy software program with single Gaussian fitting and a linear background [101].

4.3 Results and Discussion

A specific count of a Ni foil was simulated with and without the shield chamber to assess its impact on the simulated results. The experiment spectrum along with the two simulated spectra are presented in Fig. 4.6, along with the difference between each simulated spectrum and the experiment spectrum. Counts for all spectra were normalized to the 810 keV peak for comparison, since the 810 keV peak was used in the activation product ratio calculations.

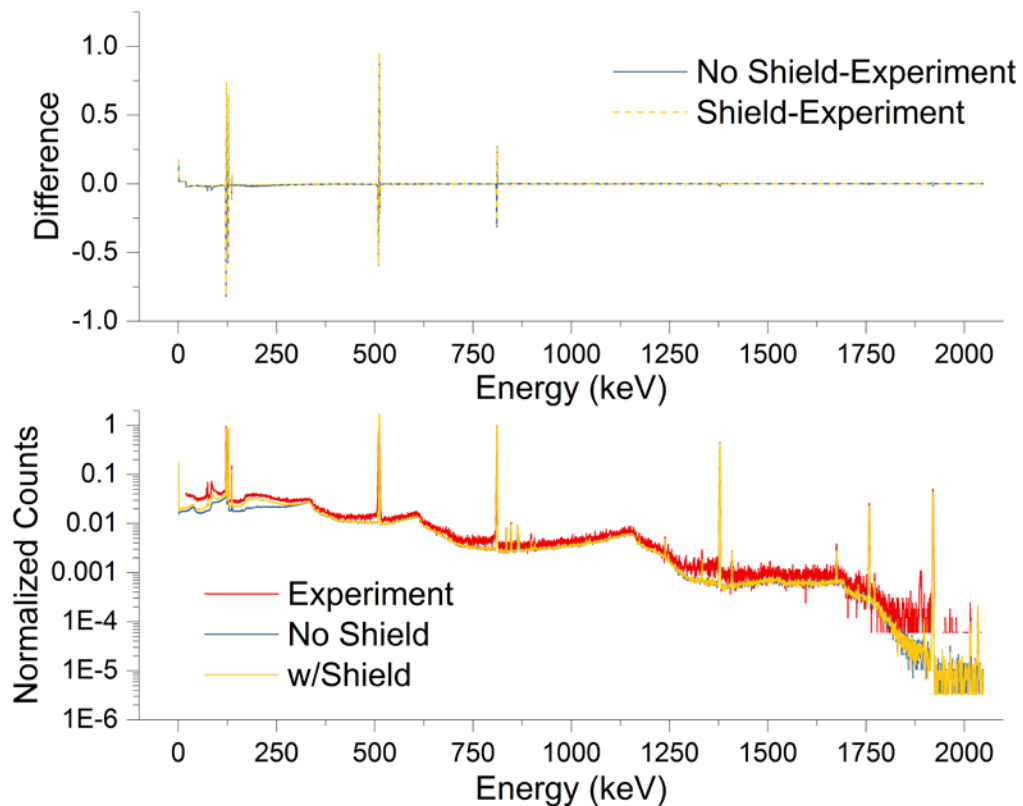


Figure 4.6 Spectrum comparison for irradiated Ni foil, 1.955 d post-irradiation, source-to-detector distance of 10.46 cm, normalized to the 810 keV peak. Top: difference between simulated and experiment spectra with the shield (yellow, dashed) and without the shield (blue). Bottom: full spectra for experiment (red), no shield (blue), and with shield (yellow).

The simulated spectra successfully recreate the major components of the experiment spectrum. Compton regions at either end of the simulated spectra are lower than experiment values. A few low energy peaks are missing from the simulation without the shield chamber. These missing peaks are attributed to Pb x-rays created by photons scattering off of the Pb in the shield. The noise of the Compton regions throughout the spectrum is lowest for the simulation including the shield chamber. The deviations between simulated and experiment spectra below 250 keV is likely caused by the dead layer approximation. Real outer crystal dead layers are non-uniform and may be significantly thinner than the 0.07 cm value used in the simulation. This affects detection efficiency at low energies, causing fewer counts to be registered in the simulated detector. The differences in spectra near 2000 keV are likely due to the ability of the simulations to run more particles and generate better statistics in the high energy region and combat decreasing photopeak efficiency. Opposing peaks in the top panel of Fig. 4.6 illustrate a small degree of peak shift. Fig. 4.7 shows the peak shift occurring at 810 keV. The peak shift is due to nonlinearity in the physical detector and does not affect quantitative results.

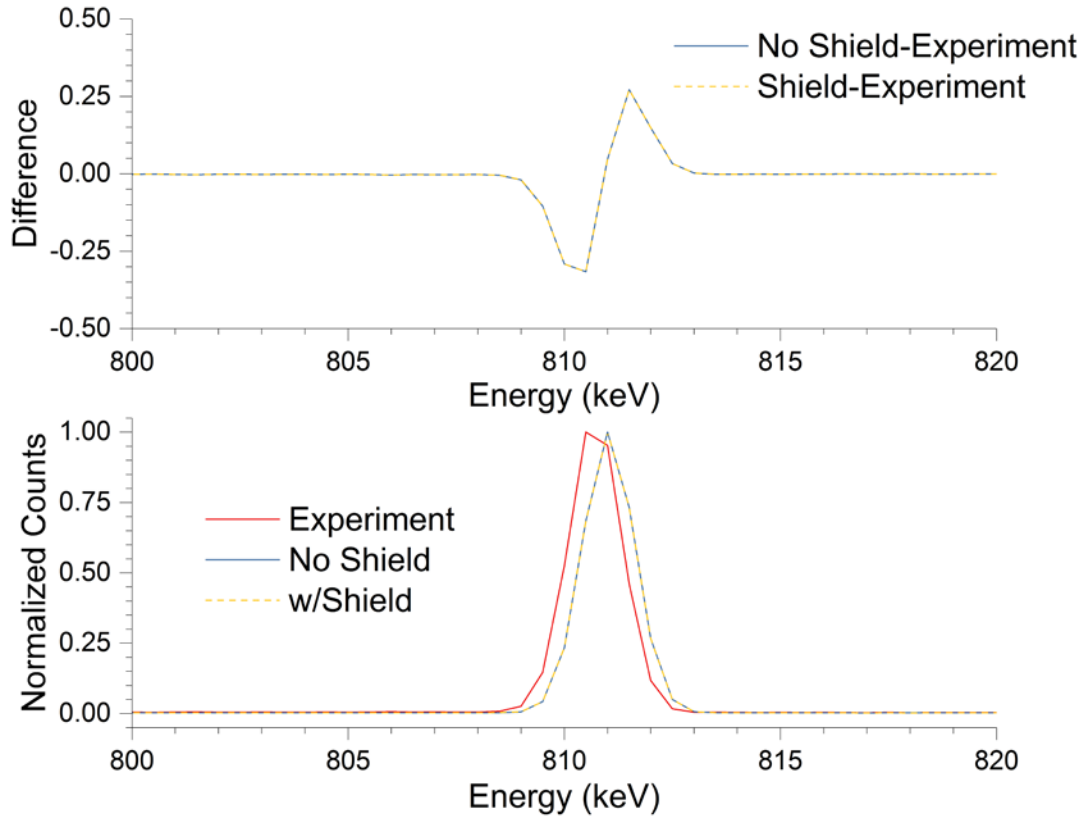


Figure 4.7 Magnification of peak shift observed at the 810 keV peak in the Ni spectrum. Top: difference between simulated and experiment spectra with the shield (yellow, dashed) and without the shield (blue). Bottom: spectra for the experiment (red) no shield (blue), and with shield (yellow, dashed).

Model performance was assessed by comparing activation product ratios calculated from simulated spectra using Eq. (4.3) and experiment data in Tables 4.2 and 4.3. Performance ratios representing the simulated activation product ratio value divided by the experiment activation product ratio value (Simulation/Experiment) are plotted in Fig. 4.8 and 4.9. Performance ratio values and uncertainties are presented in Table 4.4. Good performance yields a Simulation/Experiment ratio value of 1. Nuclides are identified as X-A(E), where X is the element symbol, A is the mass number of the nuclide and E is the gamma-ray energy in keV, rounded down to the whole number.

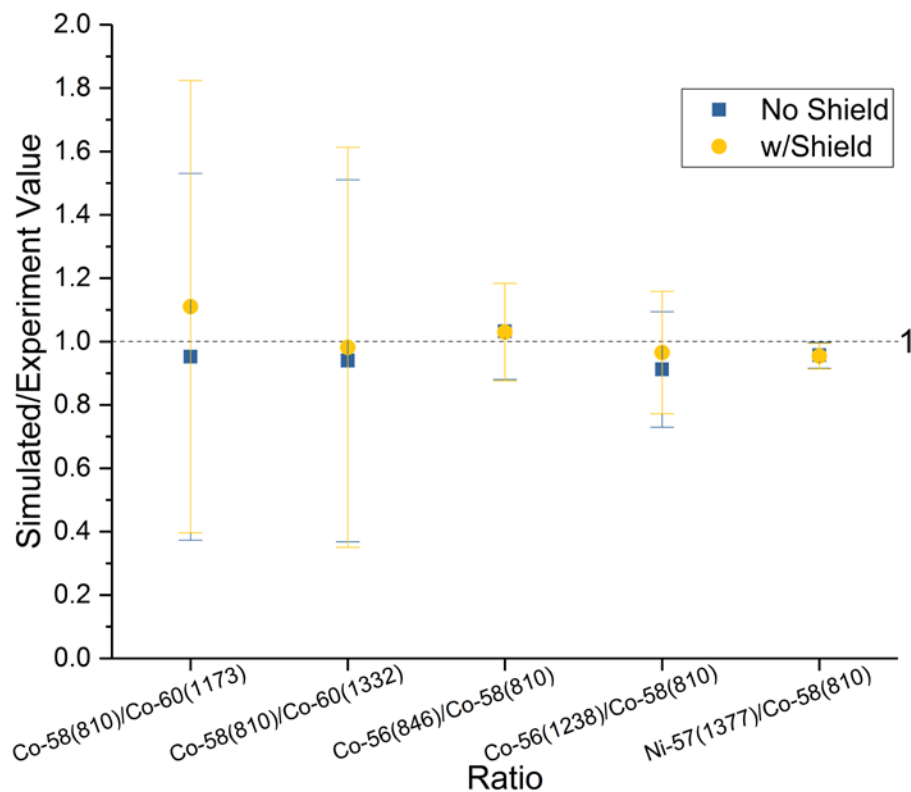


Figure 4.8 Simulation/Experiment performance ratios for the recreated count to assess the quantitative effect of the shield chamber. Blue-no shield; Yellow-with shield. Nuclides listed as X-A(E), where X is the element symbol, A is the mass number, and E is the approximate gamma-ray energy used. Ideal performance would yield a ratio value of 1.

The Simulation/Experiment ratios plotted in Fig. 4.8 show the quantitative results based on the recreated count described in Fig 4.6. All ratios for both scenarios are statistically similar to experiment values and vary little from each other. The large uncertainties are driven by experiment results. It is clear that the presence of the shield chamber does not offer any significant quantitative advantages. Therefore, the shield chamber may be omitted in order to reduce computation time. The additional results that follow are based on simulations that did not include the shield chamber.

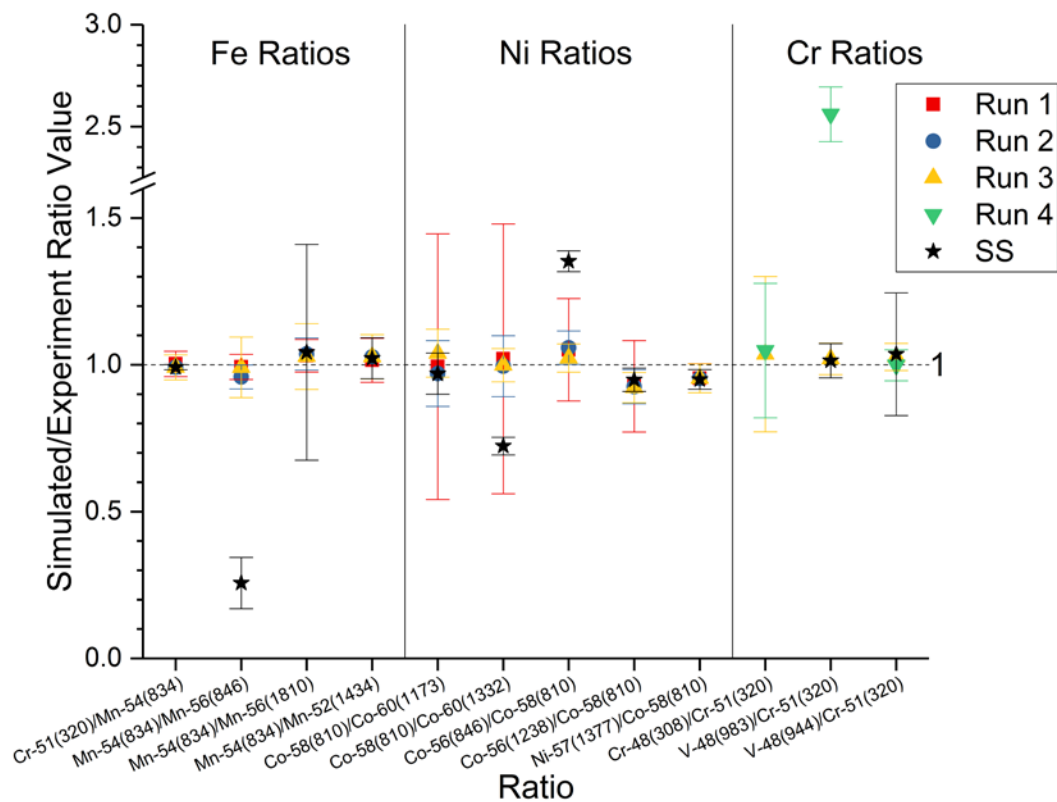


Figure 4.9 Simulation/Experiment performance ratios for each activation product ratio for all target foils. Nuclides listed as X-A(E), where X is the element symbol, A is the mass number, and E is the approximate gamma-ray energy used. Ideal performance would yield a ratio value of 1.

The Simulation/Experiment ratios plotted in Fig. 4.9 show the performance of the simulation for each target foil in all runs. Fe and Ni based ratios are grouped for single element foil Runs 1-3 as well as the SS foil. Cr based ratios are grouped for single element Runs 3 and 4 along with the SS foil. This allows for comparison of pure single element foils, with relatively simple spectra, against the multi-element SS foil having more complex spectra. All Simulation/Experiment ratios fall within 10% of a value of 1, with a few exceptions caused by significant interferences.

For the Fe activation product ratios, only the $^{54}\text{Mn}(834\text{ keV})/^{56}\text{Mn}(846\text{ keV})$ ratio deviates significantly from the desired value of 1. This is due to the presence of the ^{56}Co 846 keV line which overlaps directly with the ^{56}Mn 846 keV line, driving down the value of the simulated activation product ratio. By substituting the 1810 keV line of ^{56}Mn for the 846 keV line, the interference is avoided.

For the Ni activation product ratios, only the $^{58}\text{Co}(810\text{ keV})/^{60}\text{Co}(1332\text{ keV})$ and $^{56}\text{Co}(846\text{ keV})/^{58}\text{Co}(810\text{ keV})$ ratios in the SS foil give unacceptable results. The nuclide ^{52}Mn was detected during the experiment run for the SS foil, causing the 1333 keV line of ^{52}Mn to interfere with the 1332 keV line of ^{60}Co , lowering the simulated activation product ratio value. Again, the ^{56}Co 846 keV line is shared with the ^{56}Mn 846 keV line. Substituting the ^{60}Co 1173 keV and ^{56}Co 1238 keV lines removes the interferences and returns the Simulated/Experiment ratios to more acceptable values.

For the Cr activation product ratios, ^{48}Cr was not detected in the SS experiment and only the $^{48}\text{V}(983\text{ keV})/^{51}\text{Cr}(320\text{ keV})$ ratio in Run 4 is significantly different from the experiment ratio value. This is due to the presence of ^{48}Sc having a 983 keV line which interferes directly with ^{48}V . Substituting the 983 keV line for the 944 keV line removes the ^{48}Sc interference and returns the ratio to an acceptable value.

Table 4.4 gives the Simulated/Experiment ratio values with 1-sigma uncertainties. In the majority of cases, the uncertainty in the experiment activation product ratio was the primary driver of the final Simulated/Experiment ratio uncertainties. In a few cases where experiment ratio uncertainties were low, the uncertainty in the gamma-ray probability was the primary driver or a major contributor.

This occurred for ^{56}Mn (1810 keV), ^{52}Mn (1434 keV), ^{57}Ni (1377 keV), and ^{48}Cr (308 keV) based ratios in all runs. In ever fewer cases, the uncertainty in the simulated peak area was the primary driver of the final uncertainty. This occurred for the ^{60}Co 1173 keV peak in Run 3 and the SS foil, as well as the ^{56}Co 1238 keV and ^{48}V 944 keV peaks in the SS foil. Uncertainties for simulated ratios were calculated by combining the relative uncertainties of each term in Eq. (4.3) in quadrature. Standard error propagation was used to arrive at the final relative uncertainties.

Table 4.4 Performance ratio values for Fe, Ni, Cr, and SS foils with 1-sigma uncertainty (ND: not detected)

Ratio	Run 1	Run 2	Run 3	Run 4	SS
$^{51}\text{Cr}(320)/^{54}\text{Mn}(834)$	1.00(4)	0.99(4)	0.99(4)		0.992(9)
$^{54}\text{Mn}(834)/^{56}\text{Mn}(846)$	0.99(4)	0.99(4)	0.99(10)		0.26(9)
$^{54}\text{Mn}(834)/^{56}\text{Mn}(1810)$	1.03(6)	1.03(11)	1.03(11)		1.0(4)
$^{54}\text{Mn}(834)/^{52}\text{Mn}(1434)$	1.02(7)	1.03(8)	1.03(8)		1.02(7)
$^{58}\text{Co}(810)/^{60}\text{Co}(1173)$	1.0(5)	0.97(11)	1.04(8)		0.97(7)
$^{58}\text{Co}(810)/^{60}\text{Co}(1332)$	1.0(5)	1.00(10)	1.00(6)		0.72(3)
$^{56}\text{Co}(846)/^{58}\text{Co}(810)$	1.05(17)	1.06(6)	1.02(5)		1.35(4)
$^{56}\text{Co}(1238)/^{58}\text{Co}(810)$	0.93(16)	0.93(6)	0.92(5)		0.95(4)
$^{57}\text{Ni}(1377)/^{58}\text{Co}(810)$	0.95(5)	0.95(5)	0.95(5)		0.95(3)
$^{48}\text{Cr}(308)/^{51}\text{Cr}(320)$			1.0(3)	1.05(23)	ND
$^{48}\text{V}(983)/^{51}\text{Cr}(320)$			1.02(5)	2.56(13)	1.01(6)
$^{48}\text{V}(944)/^{51}\text{Cr}(320)$			1.03(5)	1.00(5)	1.04(21)

4.4 Conclusions

The MCNP6.1 HPGGe model accurately predicted activation product ratios in Fe, Ni, Cr, and SS foils, provided that the gamma-ray lines used in the analysis did not have significant interferences. In most cases, uncertainty in the experiment data was the major component of the final uncertainty of the Simulated/Experiment ratios. The

HPGe model accurately recreates experiment spectra. Minor peak shifts were observed between simulated and experiment spectra, caused by nonlinearity of the physical detector, but did not affect quantitative results. Photopeak efficiency of the model is comparable to the physical detector. The generalized dead layer approximation only affects low energy photons, which were not focused on in this study. Comparing results with and without the shield chamber showed that inclusion of the shield chamber does not provide any quantitative advantages. Omitting the shield chamber reduces computation time, removes backscatter and x-ray peaks, and increases noise in the Compton regions of spectra.

This model can be used to plan future experiments and explore different scenarios. With knowledge of nuclide activities, the model can be used to play out different what-if situations. It can be used to determine whether or not sample components can be detected at different decay times without having to perform successive experiments, saving on resources. The model can also be used to investigate potential interferences, assessing whether or not corrections need to be made of if other gamma rays should be used in analysis. Overall, this work has shown that a generalized HPGe detector model based on the manufacturer specification sheet is capable of providing accurate quantitative results without the need for extensive characterization of the physical detector.

Chapter 5: Comparison of Irradiated Foil Measurements with Activation Calculations and HPGe Simulations⁴

The work presented here is adapted from [44]. It evaluates the simple approach to performing activation calculations when considering a limited number of reactions. The Flattop critical assembly was used as the neutron source for the activation calculations. Additionally, the high-purity germanium detector model validated in Chap. 4 is used to simulate gamma-ray spectroscopy measurements and determine if there is a correlation between decay time and accuracy for selected activation product ratios. A derivation of the depletion reaction equation is offered in App. A. The Flattop critical assembly is described further in App. B.

5.1 Introduction

Radiation interaction simulations allow different scenarios to be explored more efficiently, bypassing common obstacles to experiments. Access to irradiation sources may be cost prohibitive and time constraints may render an experiment impractical. One use of simulations is to evaluate different safety options to minimize a researcher's dose [102–104]. Additionally, simulations can be used to optimize experiment

⁴ Reprinted by permission from Springer Nature: Springer Journal of Radioanalytical and Nuclear Chemistry, J.J. Goodell, C.M. Egnatuk, S.W. Padgett, C.C. Keith, T.A. Bredeweg, N. K. Harward, B.B. Bandong, K.E. Roberts, A.C. Mignerey, Comparison of irradiated foil measurements with activation calculations and HPGe simulations, J. Radioanal. Nucl. Chem. <https://doi.org/10.1007/s10967-018-5820-6>. Copyright 2018. This work was performed under the auspices of the U.S. Department of Energy by Lawrence Livermore National Laboratory under Contract DE-AC52-07NA27344.

parameters like irradiation and decay times. Also, some situations cannot be achieved experimentally. When this occurs, simulations can be used to predict environmental conditions, as well as define and track material signatures [105, 106].

This work evaluates a simple approach to simulating neutron activation and gamma-ray spectroscopy measurements using theoretical activation calculations and a high-purity germanium (HPGe) detector model. The intent is to simulate the activation and measurement process from start to finish in support of experiment planning efforts and to determine if this simple approach provides satisfactory results. Activation calculations for individual activation products are compared against measured values from a critical assembly foil irradiation experiment in order to determine if the results are suitable as initial input for measurement simulations. The critical assembly supplies fission spectrum neutrons, a distribution of interest in technical nuclear forensics exercises. The materials under study are stainless steel grade 304 (SS) and two of its components, Fe and Ni. These are common components of structural materials that can lead to significant induced radioactivity [68, 69]. Comparison between the activation of the individual elements and the alloy is used to investigate possible changes in the activation network.

Gamma-ray spectroscopy measurements are simulated in this work with a Monte Carlo HPGe detector model using the Monte Carlo N-Particle radiation transport code (MCNP) version 6.1 [84]. Since peak resolution can be a limiting factor for quantitative gamma-ray measurements, HPGe detectors are used because of their superior resolution over other semiconductor or scintillation detectors [107, 108]. This characteristic is necessary when dealing with high-Z materials and fission products

because of the substantial number of potentially closely spaced gamma-ray emission energies. The use of the critical assembly neutron source makes contamination from fission products a possibility that could undermine the reliability of gamma-ray spectroscopy measurements. To address this, the HPGe model is used to investigate the effect of decay time on the reliability of activation product ratio calculations and identify an optimal measurement window. A variety of activation product ratios are chosen based on experimentally measured nuclides to determine which, if any, are sensitive to the decay time.

5.1.1 The Activation Network

The activation products under consideration in this study focus on six neutron reactions – (n,γ) , (n,α) , (n,p) , $(n,2n)$, $(n,3n)$, and $(n,4n)$ – in Fe, Ni, and SS foils. These reactions on naturally occurring isotopes of Fe and Ni are considered primary reactions in this work. The cross sections for these six reactions cover a wide range of incident neutron energies and include threshold reactions. The limitation of studying only these primary reactions allows the complexity of the activation network to be assessed. An example of what may result from the irradiation of a Fe target is presented as an activation map in Fig. 5.1. In the activation map, nuclides are shaded based on their role during activation and decay. Only naturally occurring isotopes are considered to be target nuclides. Solid lines leaving these target nuclides show each specific reaction and point to the appropriate activation product. Any unstable activation products either decay directly to a stable nuclide or proceed through one or two daughter products

before reaching a stable nuclide. Abundance and decay data were taken from the National Nuclear Data Center Chart of the Nuclides [80].

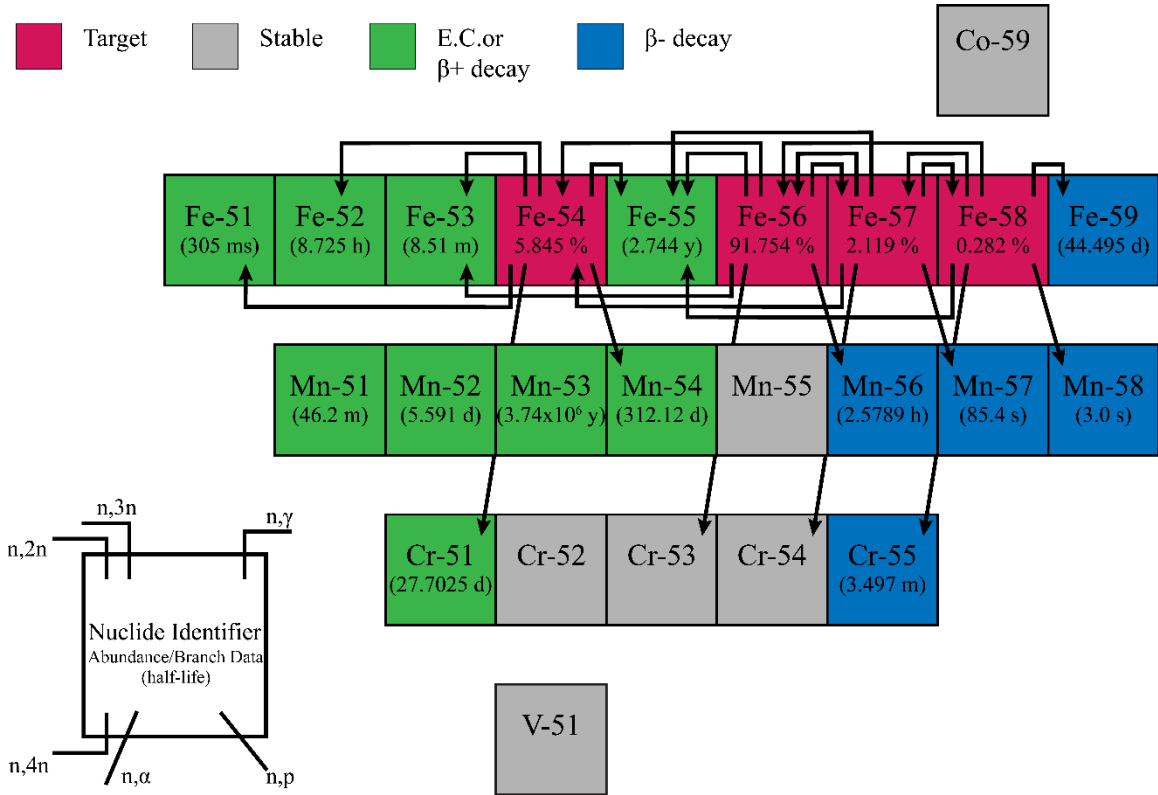


Figure 5.1 Activation map for Fe showing the six primary neutron reaction pathways [80].

Depending on irradiation conditions, complex activation networks may enable successive activations which can cause depletion or buildup of individual activation products. This situation is further complicated when multiple target elements with similar Z numbers are present, as is the case in SS. For example, ^{59}Fe has a half-life of 44.495 days and is produced through the $^{58}\text{Fe}(n,\gamma)^{59}\text{Fe}$ pathway. The nuclide ^{59}Fe could then undergo any one of the six neutron capture reactions under consideration, thereby lowering the amount of ^{59}Fe produced from ^{58}Fe , constituting a depletion reaction. In the opposite case and for a SS foil, ^{54}Mn is a direct product of (n,p) reaction on ^{54}Fe .

Mn is a minor element in most stainless steels, which would result in the production of ^{54}Mn from the $^{55}\text{Mn}(n,2n)^{54}\text{Mn}$ pathway. Depending on the situation, depletion and buildup reactions may need to be accounted for in simulations and theoretical calculations. One goal of this study is to determine whether or not only considering the primary reactions is sufficient for predicting activation product ratios. Activation product ratios and reactions are given in Table 5.1 along with the primary gamma-ray energy and absolute intensity used in analysis [80].

Table 5.1 Activation products, ratios, and gamma-ray lines with 1-sigma uncertainty used in analysis [80]

Foil	Ratio	Reaction	E_γ (keV)	E_γ Intensity (%)
Fe	$^{54}\text{Mn}/^{51}\text{Cr}$	$^{54}\text{Fe}(n,p)^{54}\text{Mn}$	834.848(3)	99.9760(10)
		$^{54}\text{Fe}(n,\alpha)^{51}\text{Cr}$	320.0824(4)	9.910(10)
	$^{59}\text{Fe}/^{51}\text{Cr}$	$^{58}\text{Fe}(n,\gamma)^{59}\text{Fe}$	1099.245(3)	56.5(18)
		$^{54}\text{Fe}(n,\alpha)^{51}\text{Cr}$	320.0824(4)	9.910(10)
	$^{59}\text{Fe}/^{54}\text{Mn}$	$^{58}\text{Fe}(n,\gamma)^{59}\text{Fe}$	1099.245(3)	56.5(18)
		$^{54}\text{Fe}(n,p)^{54}\text{Mn}$	834.848(3)	99.9760(10)
Ni	$^{58}\text{Co}/^{60}\text{Co}$	$^{58}\text{Ni}(n,p)^{58}\text{Co}$	810.7593(20)	99.450(10)
		$^{60}\text{Ni}(n,p)^{60}\text{Co}$	1173.228(3); 1332.492(4)	99.85(3); 99.9826(6)
	$^{59}\text{Fe}/^{60}\text{Co}$	$^{62}\text{Ni}(n,\alpha)^{59}\text{Fe}$	1099.245(3)	56.5(18)
		$^{60}\text{Ni}(n,p)^{60}\text{Co}$	1173.228(3); 1332.492(4)	99.85(3); 99.9826(6)
	$^{59}\text{Fe}/^{60}\text{Co}$	$^{62}\text{Ni}(n,\alpha)^{59}\text{Fe}$	1099.245(3)	56.5(18)
		$^{58}\text{Ni}(n,p)^{58}\text{Co}$	810.7593(20)	99.450(10)

5.2 Experimental

In this work, experiment data from a Flattop critical assembly irradiation of Fe, Ni, and SS metal foils were compared against theoretical activation calculations through calculated/experiment ratios (C/E), using ENDF/B-VII.1 cross-section data

[72]. Results from activation calculations were used to determine whether or not this method is appropriate as initial values for the HPGe simulation. Additionally, simulated HPGe measurements were modeled using MCNP6.1. The HPGe model was used to investigate the effect of decay time on measurement reliability for the activation product ratios listed in Table 5.1. Fe and Ni foils from Shieldwrx were of natural composition having 99.9679% and 99.981% purities [97]. The SS foil from Goodfellow had a mass composition of 71.2(7)% Fe, 18.39(18)% Cr, 8.05(9)% Ni, 1.81(4)% Mn, and 0.54(1)% Cu, as determined by ICP-MS analysis [98].

5.2.1 Flattop Irradiation and Measurement

The Flattop critical assembly consists of a natural uranium reflector with interchangeable cores and options for reactivity adjustments, allowing for different neutron spectra to be obtained [82]. This experiment employed a highly-enriched uranium core for the irradiation of Ni, Fe, and SS foils [40]. Foils were positioned at the center of the Flattop assembly and irradiated for 3179(4) s. The Ni and one SS foil (SS-L) were positioned slightly to the left of center, while the Fe and other SS foil (SS-R) were positioned slightly to the right of center. Foil masses, with an uncertainty of .0001 g, were 0.1666 g for Fe, 0.1762 g for Ni, 0.1518 g for SS-R, and 0.1516 g for SS-L. Au foils of 0.0751 g, 0.0760 g, and 0.0755 g, also having 0.0001 g uncertainty, were included at the left end, right end, and center position in the foil stack to serve as flux monitors. The total length of the foil stack was less than 1 cm. The neutron probability distribution for the center position, resulting from flux tally in a Monte Carlo model of the Flattop critical assembly, is shown in Fig. 5.2. The flux tally uses

and equal unit lethargy energy binning scheme with upper bin values from 1.00E-11 MeV to 20.0 MeV. Due to the small length of the foil stack, the flux distribution did not change and was used for all activation calculations.

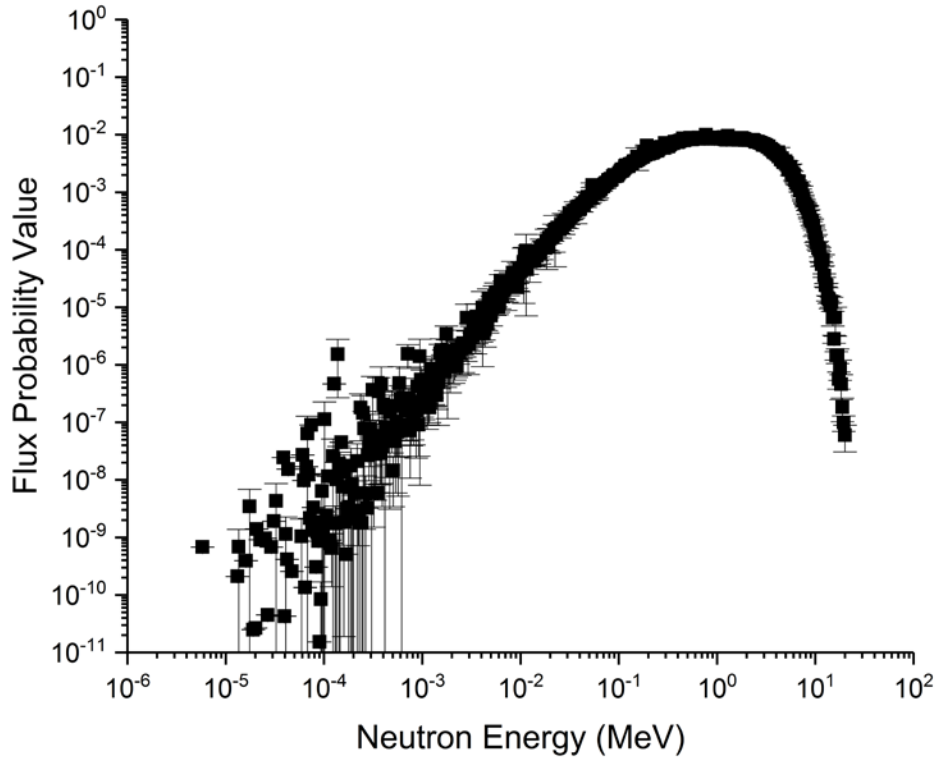


Figure 5.2 Neutron flux energy probability distribution with 1-sigma uncertainty, resulting from a flux tally in the Monte Carlo model of the Flattop critical assembly.

Experimental gamma-ray spectroscopy measurements were conducted using a suite of ORTEC GEM series p-type coaxial HPGe detectors, with each sample being counted on a minimum of three different detectors. Decay times ranged from 3 days to 15 days before measurements were taken. The relative efficiencies of the HPGe detectors ranged from 12% to 37% when compared to the 1332 keV peak of ^{60}Co measured with a 3x3 inch NaI detector at 25 cm. Counting times ranged from 12 minutes to 4320 minutes to ensure good counting statistics for peaks under

consideration. Counting geometries varied by changing the distance between the sample and detector face, covering distances from 4.86 cm to 6.67 cm, and one count at 18.67 cm. Spectrum analysis was accomplished using the GAMANAL program [109]. Final experiment results for selected activation products are presented in Table 5.2 as a weighted average of atoms of activation product at the end of irradiation (t=0) with 1-sigma uncertainties. Activation product ratios were calculated based on the experiment results at t=0.

Table 5.2 Experiment results for selected activation products as atoms at the end of irradiation for each foil with 1-sigma uncertainty

Activation Product	Fe Foil	Ni Foil	SS-R Foil	SS-L Foil
⁵⁴ Mn	1.901(8)E+10		1.192(6)E+10	1.191(5)E+10
⁵¹ Cr	2.06(3)E+08		5.70(7)E+08	5.63(8)E+08
⁵⁹ Fe	5.55(8)E+07	6.6(16)E+06	4.53(7)E+07	4.48(7)E+07
⁵⁸ Co		2.959(13)E+11	2.00(8)E+10	2.036(8)E+10
⁶⁰ Co		2.28(4)E+09	2.56(11)E+08	2.51(12)E+08

5.2.2 Activation Calculations

Activation calculations for the number of product nuclei, $N_p(t)$, were conducted according to Eq. (5.1):

$$N_p(t_{irr}) = \frac{N_0 \bar{\sigma} \Phi_T}{\lambda} (1 - e^{-\lambda t_{irr}}), \quad (5.1)$$

where $\bar{\sigma}$ is the collapsed cross section for a given reaction, Φ_T is the experimentally determined total neutron flux, N_0 is the number of target nuclei based on the foil mass, composition, and isotopic abundance, λ is the decay constant for the product nuclide, and t_{irr} is the irradiation time given in Sec. 5.2.1. The collapsed cross section, given by Eq. (5.2):

$$\bar{\sigma} = \sum \frac{\Phi(E_i)\sigma(E_i)}{\Phi_T}, \quad (5.2)$$

is a weighted sum of the ENDF/B-VII.1 reaction cross-section data, $\sigma(E_i)$, using the Flattop neutron energy probability distribution given in Fig. 2 as the weighting factors. The cross-section data was linearly interpolated to match the Flattop distribution energy binning structure. The total flux was determined experimentally through the $^{197}\text{Au}(n,\gamma)^{198}\text{Au}$ reaction in the Au flux monitor foils by rearranging Eq. (5.1) to solve for the total flux term. The total flux value used in subsequent activation calculations was an average of the different Au foil positions. Element isotopics and mass data were obtained from the NIST Table of Atomic Weights and Isotopic Compositions [110]. Uncertainties in activation calculations were estimated using standard error propagation. Uncertainty estimates for the cross-section data were taken from ENDF/B-VII.1, when available, and supplemented by TENDL-2015 when needed [72, 75]. Calculated activation yields were compared against experiment results to better understand the limitations when using Eq. (5.1) and the constrained activation network. Activation product ratios were also calculated, based on the results from Eq. (5.1), and compared against experiment ratios.

5.2.3 *HPGe Simulation with MCNP*

The gamma-ray spectroscopy measurement process was simulated using a MCNP6.1 HPGe detector model having a relative efficiency of 42%. A detailed description of the model and its performance is discussed by Goodell et al [43]. Simulated measurements were performed by modeling the detector response to a

calculated gamma-ray distribution, based on the activation product mixture at a specified point in time. Input gamma-ray distributions were calculated from experimental results for decay times of 2, 5, 10, and 15 days post-irradiation. Gamma-ray energy probabilities were defined as the product of a nuclide's activity at the time of measurement and the absolute intensity of the given gamma-ray energy. Half-lives and gamma-ray data were obtained from the National Nuclear Data Center [80]. The resulting pulse-height spectra, generated using an F8 tally in MCNP with the GEB option, were analyzed using the PeakEasy gamma-ray spectroscopy program [101].

Simulations were structured to run 10^9 particles, using the MCPLIB84 library for photon interactions and the el03 library for electron interactions. The activated foil source was positioned 10 cm from the face of the detector. Fission products and associated daughter nuclides were not included in the source terms unless they had been quantified experimentally. Simulated activation product ratios were calculated using Eq. (5.3):

$$\frac{N_1}{N_2} = \frac{PA_1 \lambda_2 \varepsilon_2 P_{\gamma 2}}{PA_2 \lambda_1 \varepsilon_1 P_{\gamma 1}} e^{t(\lambda_1 - \lambda_2)}, \quad (5.3)$$

where PA_i is the respective peak area calculated in PeakEasy, λ_i is the appropriate decay constant, $P_{\gamma i}$ is the selected gamma-ray intensity from Table 5.1, t is the decay time, and ε_i is the photopeak efficiency for the chosen gamma-ray energy. Simulated peak areas determined by Gaussian peak fitting with a linear background in PeakEasy. When multiple peaks were found within the region of interest, the number of Gaussian peaks used to fit the desired peak were automatically selected by PeakEasy. Simulated activation product ratios back-calculated to $t=0$ were compared against experiment

results. Photopeak efficiency values, based on the calibration in [43], were calculated using Eq. (5.4):

$$\ln(\varepsilon) = \sum_{i=0}^n a_i \left[\ln \left(\frac{E_\gamma}{E_{ref}} \right) \right]^i, \quad (5.4)$$

where $i=4$, E_γ is the photopeak energy in keV, and E_{ref} is equal to 1 keV. The values of the coefficients are given in Table 5.3.

Table 5.3 Coefficient values with standard deviation for the photopeak efficiency function described by Eq. (5.4)

Coefficient (a_i)	Value	Standard Deviation
a_0	-109	± 3
a_1	68	± 3
a_2	-16.5	± 0.7
a_3	1.73	± 0.09
a_4	-0.068	± 0.004

5.3 Results and Discussion

5.3.1 Activation Calculations vs Experiment

The ratio of individual activation yields, calculated using Eq. (5.1) and ENDF/B-VII.1 data, to experiment values for the Fe, Ni, and SS foils are shown in Fig. 5.3. Calculated/Experiment (C/E) ratio values range from 0.62 to 1.31, with relative uncertainties less than 5% in most cases. The C/E result for ^{59}Fe in the Ni foil is the exception, having a relative uncertainty of 27%, dominated by the experiment results. The relative uncertainty for the production of ^{59}Fe in Ni using Eq. (5.1) is only 9%, whereas the uncertainty in the experimental value of ^{59}Fe is 25%. C/E ratio values for the Fe and Ni foils are consistently above 1, except for ^{60}Co in the Ni foil. C/E values for both SS foils agree with each other in all cases. However, in the SS foils,

C/E values for ^{54}Mn and ^{58}Co are greater than 1, while those for ^{51}Cr are close to 1, and values for ^{59}Fe and ^{60}Co are less than 1. In the Fe and Ni foils, C/E values for ^{54}Mn and ^{58}Co are similar to the SS foils, but the values for ^{51}Cr , ^{59}Fe , and ^{60}Co are not. Production of ^{51}Cr in the SS foils included pathways using Cr targets, since Cr is the second largest component. It was determined that $^{50}\text{Cr}(n,\gamma)$ and $^{51}\text{Cr}(n,2n)$ reactions amount to 73% of total ^{51}Cr production through theoretical calculations, while the $^{54}\text{Fe}(n,\alpha)^{51}\text{Cr}$ reaction produces the remainder. Total ^{51}Cr production from both the Fe and Cr targets was used for the SS foil analysis.

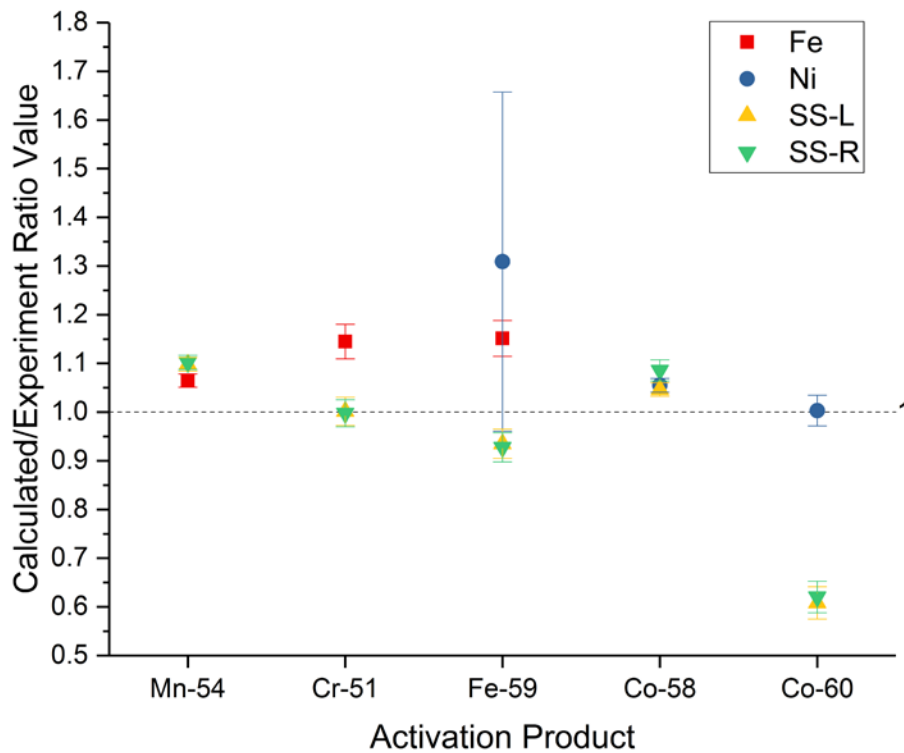


Figure 5.3 C/E ratios for theoretical activation calculations of individual activation products with 1-sigma uncertainty.

There are four potential causes for deviations from C/E values of 1 – inaccuracies in the neutron source distribution; errors in the cross-section data; the occurrence of secondary activations leading to depletion or buildup of the selected activation product; and incomplete selection of production pathways. Inspection of the input parameters for Eq. (5.1) shows that the uncertainty of the theoretical values is driven by the uncertainty in the collapsed cross section. Since both the neutron source distribution and the cross-section data are used in Eq. (5.2) to calculate the collapsed cross section, it is difficult to say which is more responsible for the C/E deviations without a thorough investigation of both variables. It is unlikely that either the neutron distribution or the cross-section data is the sole cause of the C/E deviations. Evidence for this includes the fact that theoretical uncertainties are relatively small and that total ^{51}Cr for the SS foils and ^{60}Co for the Ni foil have nearly perfect C/E values.

Even though uncertainties in the neutron distribution and cross-section data are small, that does not account for possible inaccuracies in either variable. Additionally, the method in which the collapsed cross section may introduce additional error by underestimating or over estimating the collapsed cross-section value. Based on the ENDF/B-VII.1 data, this would be most problematic for the (n, γ) reaction on ^{58}Fe due to the resonances in the cross section. The remaining reactions are all threshold reactions that do not have resonances, so the effect is expected to be less. It is likely that errors in both variables contribute in varying degrees for the production of a given radionuclide and should be addressed on a case by case basis.

Secondary or successive activations causing depletion or buildup may also play a role in the C/E deviations. Depletion of the primary activation product is not initially

considered in theoretical calculations, but if present during the experiment, it would cause C/E values to be above 1. This may be the case for ^{54}Mn , ^{51}Cr , and ^{59}Fe in the Fe foil, for ^{59}Fe and ^{58}Co in the Ni foil, and for ^{54}Mn and ^{58}Co in the SS foils. To determine the impact of depletion reactions, depletion calculations were performed by modifying Eq. (5.1) to include secondary activation, resulting in Eq. (5.5):

$$N_p(t_{irr}) = \frac{N_0 \Phi_T \bar{\sigma}_1}{\lambda + \Phi_T \bar{\sigma}_2} (1 - e^{-t_{irr}(\lambda + \Phi_T \bar{\sigma}_2)}), \quad (5.5)$$

where the secondary activation of the primary product is accounted for by the $\Phi_T \bar{\sigma}_2$ term. The total interaction cross sections from JEFF-3.2 or JENDL-4.0 were used to calculate $\bar{\sigma}_2$ as an upper limit on secondary activation, since ENDF/B-VII.1 data was not available [73, 74]. Depletion calculations showed insignificant differences, less than 0.001%, in the final value of the primary activation product from the original calculation. Therefore, depletion reactions can be eliminated from the list of possible causes contributing to C/E deviations. In depletion reactions, the magnitude of the secondary activation rate relative to the primary activation rate, along with the decay constant of the primary activation product, determine how substantial product depletion will be. Since the relative activation rates already show that depletion is unlikely, buildup reactions through secondary activation are also unlikely.

The simplest explanation for the C/E deviations in Fig. 5.3 is that the limited number of production pathways, outlined by the example in Fig. 5.1, do not accurately reflect the reaction channels seen in experiments. Additional experimental reaction channels would have the effect of lowering C/E values. Examples of where this may be the case are ^{59}Fe and ^{60}Co in the SS foils. For ^{59}Fe , predictions for the Fe and Ni

foils are high, but predictions for the SS foils are low. It is expected that prediction trends in the Fe and Ni foils would carry over to the SS foils, as for ^{58}Co , but they do not. If additional pathways are responsible, they would have to include different target nuclides. Between Fe or Ni and SS, there are no additional target nuclides that could be responsible for additional production pathways. Only Cu and Mn are additional elements above trace levels and they do not have viable pathways to ^{59}Fe . Therefore, the discrepancy in C/E values for ^{59}Fe between the Fe, Ni, and SS foils is due to errors in the calculation of the collapsed cross section or experimental error.

For ^{60}Co , predictions in the Ni foil are accurate, but predictions in the SS-foil are not. One possible additional pathway is the $^{63}\text{Cu}(n,\alpha)$ reaction. However, Cu is a minor component of SS and the $^{63}\text{Cu}(n,\alpha)$ cross section is lower than the $^{60}\text{Ni}(n,p)$ cross section. This suggests that additional reaction pathways are not likely to be responsible for the significant deviation in ^{60}Co C/E values between the Ni and SS foils. Rather, it is another case of a combination of errors in the calculation of the collapsed cross section and possibly experimental error.

Of the four potential causes for C/E deviations, the collapsed cross section appears to have the most significant effect. Accuracy errors need to be treated on a case by case basis, looking at the neutron source distribution, quality of the cross-section data, and potential number of production pathways. Expanding the reaction set and thorough investigation of collapsed cross section calculations may lead to more accurate results, or at least a better understanding of the sources of error. Accuracy errors in the individual nuclide C/E ratios combine as expected to produce activation

product C/E values ranging from 0.84-1.75. The inconsistency of the results makes the individual activation calculations unsuitable as input for the HPGe simulation.

5.3.2 Decay Time Effects on HPGe Simulation

The effect of decay time on the ability to measure activation product ratios was evaluated using a HPGe detector model to simulate gamma-ray spectroscopy measurements at decay times of 2, 5, 10, and 15 days. Simulated activation product ratios were calculated using Eq. (5.3) and compared to experiment values to investigate the reliability of measurements over time. C/E values with 1-sigma uncertainty for activation product ratios in the Fe and Ni foils are shown in Fig. 5.4. Large error bars are due to significant experiment error. HPGe simulations for the Ni foil were run with 10^{10} source particles, rather than 10^9 , in order to reduce statistical uncertainty in the ^{59}Fe 1099 keV peak. The large error bars for the ^{59}Fe based ratios in the Ni foil are dominated by the experimental error of 25%, whereas the uncertainty in the simulated results are near 12%.

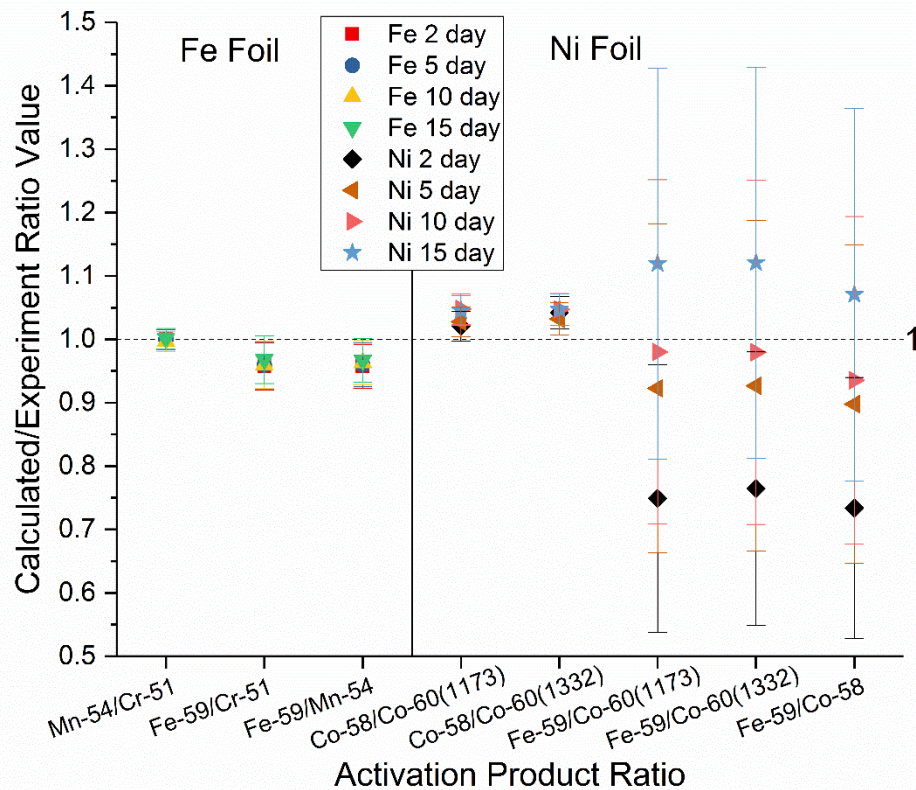


Figure 5.4 C/E values, with 1-sigma uncertainty, at each decay time for activation product ratios from the Fe and Ni foils, as determined by HPGe simulation

The clustered results for the $^{54}\text{Mn}/^{51}\text{Cr}$, $^{59}\text{Fe}/^{51}\text{Cr}$ and $^{59}\text{Fe}/^{54}\text{Mn}$ ratios in the Fe foil, along with the $^{58}\text{Co}/^{60}\text{Co}$ ratio in the Ni foil, show that the ability to measure these ratios is independent of the decay time. The spread of the $^{58}\text{Co}/^{60}\text{Co}$ ratio values in the Ni foil for the different time steps is larger, but all values are statistically similar for 1-sigma uncertainty. Even though the $^{59}\text{Fe}/^{60}\text{Co}$ and $^{59}\text{Fe}/^{58}\text{Co}$ ratios are statistically similar, the dispersion of over the different time steps suggests that there is an interference present that undermines the ability to predict these ratios. Since the time dependence is similar between the $^{59}\text{Fe}/^{60}\text{Co}$ and $^{59}\text{Fe}/^{58}\text{Co}$ ratios, the interference is most likely associated with the detection of ^{59}Fe .

The decay time dependence of the ^{59}Fe based ratios in the Ni foil is shown in Fig. 5.5. The C/E values for all three ratios increase with decay time. The large uncertainty is due to experimental uncertainty in the ^{59}Fe value. At the 2 and 15 day time steps, the C/E values are different, but remain statistically similar because of the large experimental uncertainty. Analysis of the simulated activation product ratios shows that the 2 and 15 day values are indeed statistically different, with a 1-sigma uncertainty around 12%. The simulated uncertainty is driven by the ^{59}Fe peak area uncertainty, as determined by PeakEasy. ^{59}Fe is produced through the $^{62}\text{Ni}(n,\alpha)$ reaction in the Ni foil. The natural abundance of ^{62}Ni is approximately 3.6%, making ^{59}Fe a minor activation product and sensitive to interferences. Analysis of the simulated spectra reveals an interference from the 1596 keV line of ^{140}La . The 1099 keV line of ^{59}Fe used in this analysis falls within the Compton region of the prominent ^{140}La peak. Since ^{59}Fe production in the Ni foil is low, the 1099 keV peak is obscured by the Compton continuum of the ^{140}La 1596 keV peak. As ^{140}La decays away, more of the ^{59}Fe 1099 keV peak is revealed, leading to more accurate results.

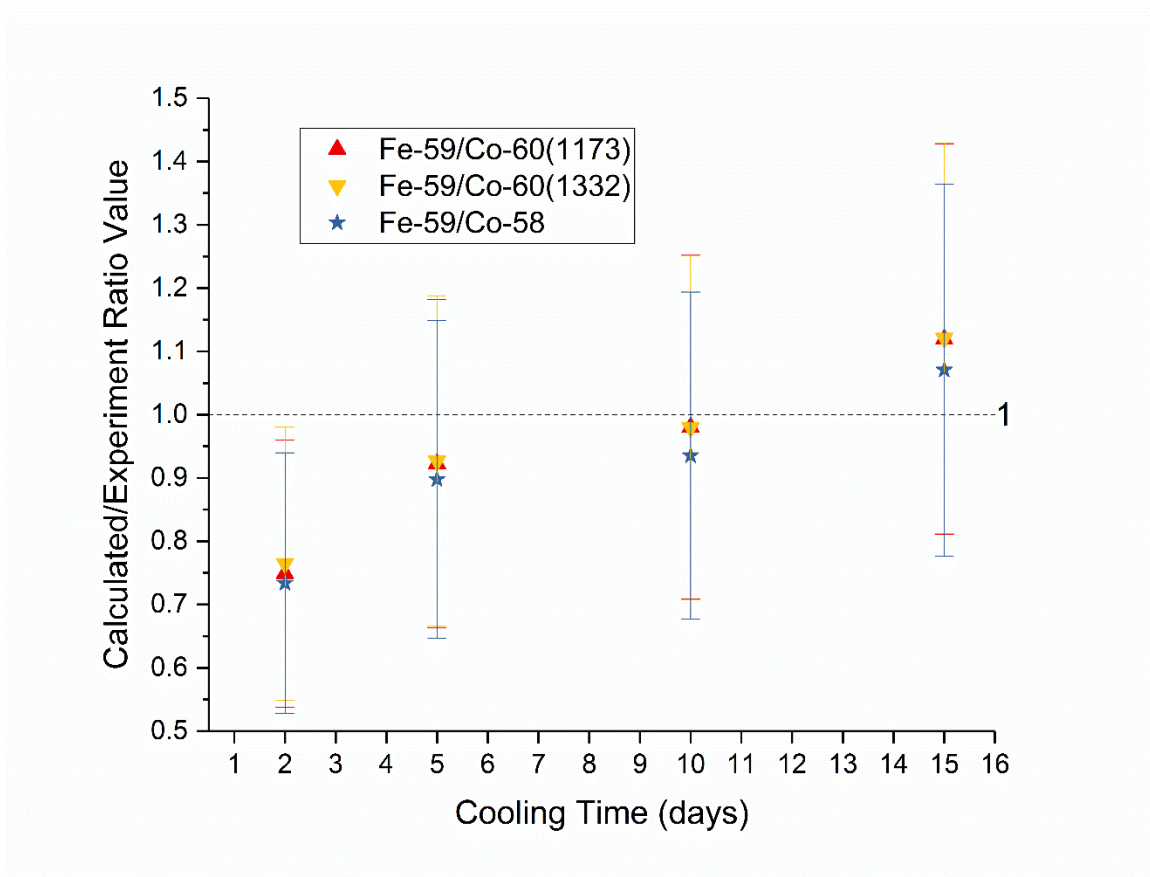


Figure 5.5 Decay time dependence of ^{59}Fe based activation product ratios in the Ni foil as determined by HPGe simulation. C/E results are given with 1-sigma uncertainty.

Figure 5.6 shows the C/E ratios, with 1-sigma uncertainty, for the SS-L foil. Only the $^{58}\text{Co}/^{60}\text{Co}$ and $^{59}\text{Fe}/^{60}\text{Co}$ activation product ratios exhibit any decay time dependence. All other ratios are statistically similar over the different time steps. Analysis of the SS-R foil produces a similar plot, but uncertainties are larger, causing all ratios to be statistically similar for all time steps. ^{140}La is also present in the SS-L foil, but the ^{59}Fe interference that was seen with the Ni foil is not a factor here since the Fe component is the major producer of ^{59}Fe . The larger amount of ^{59}Fe makes detection of the 1099 keV peak less susceptible to fluctuations in the background caused by the disappearance of the ^{140}La peak. Since the decay time dependence is

limited to ^{60}Co based ratios, any interferences are associated with the detection of both the 1173 keV and 1332 keV lines of ^{60}Co .

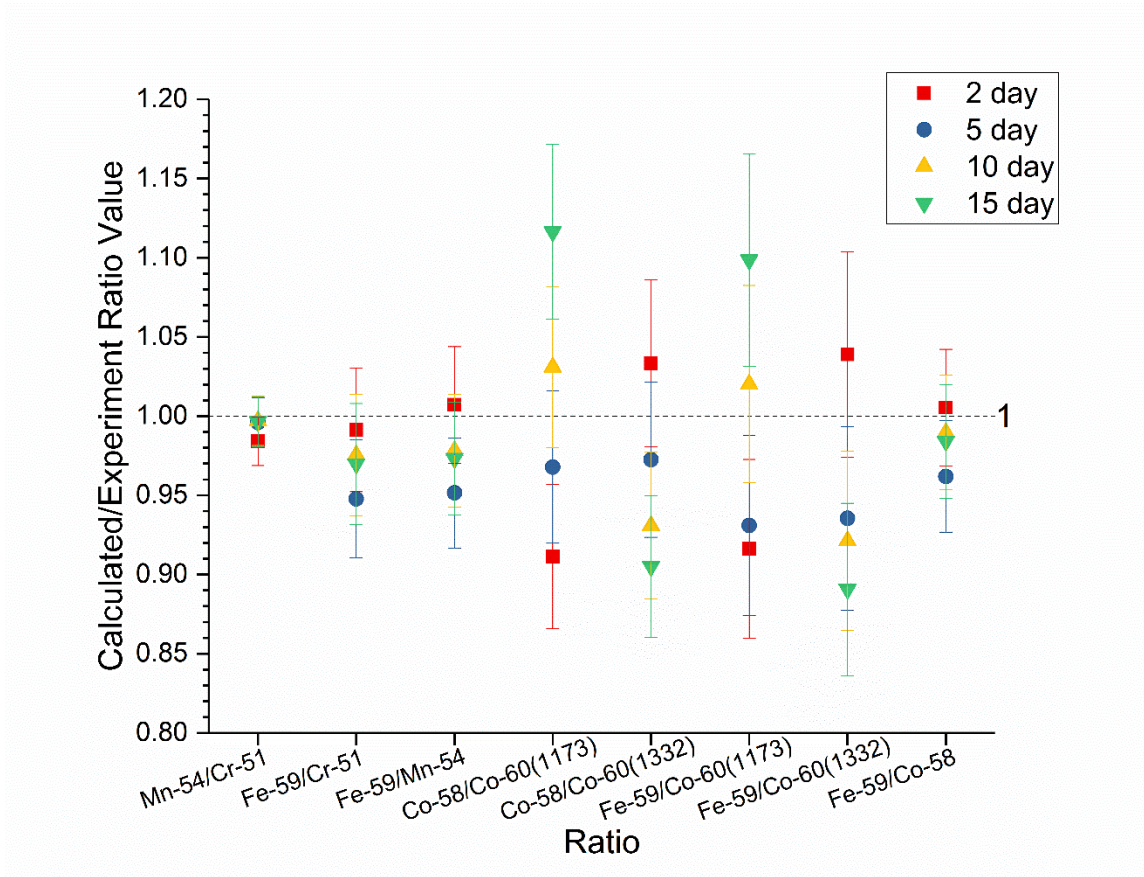


Figure 5.6 C/E values, with 1-sigma uncertainty, at each decay time for activation product ratios in the SS-L foil, as determined by HPGe simulation.

The decay time dependence of the $^{58}\text{Co}/^{60}\text{Co}$ and $^{59}\text{Fe}/^{60}\text{Co}$ activation product ratios is shown in Fig. 5.7. Interestingly, the trends are dependent on which line of ^{60}Co is being used, suggesting separate interferences for each line. C/E values for activation products using the 1173 keV peak increase with decay time, while the opposite is true for the 1332 keV peak. Analysis of the relative change in peak area between time steps helps to clarify what the causes may be. For the 1332 keV based activation product ratios, the ^{60}Co peak area increases by approximately 28% between the 2 day and

15 day time steps. The ^{59}Fe peak area decreases by roughly 1.5% and the ^{58}Co peak area increases by about 8%. The trends for the relative changes in peak areas between time steps match up with the trend for the 1332 keV based activation product ratios in Fig. 5.7. The large increase in the ^{60}Co 1332 keV peak area can be attributed to its longer half-life, relative to the measurement period, and the disappearance of short-lived interfering products, like ^{140}La and ^{24}Na . The longer half-life of ^{60}Co prevents significant decrease in its activity between the shortest and longest measurement. The disappearance of short-lived products reduces the background around the 1332 keV peak. Both of these contribute to making ^{60}Co a larger relative component of the sample at later time steps. Similar reasoning can be applied to the change in ^{58}Co peak area but showing a lesser effect. The relative decrease in ^{59}Fe peak area is related more to its shorter half-life relative to ^{58}Co and ^{60}Co . Since the increase in the 1332 keV peak area is much larger than the changes in ^{58}Co and ^{59}Fe , the 1332 keV peak dictates the decreasing trend in C/E values.

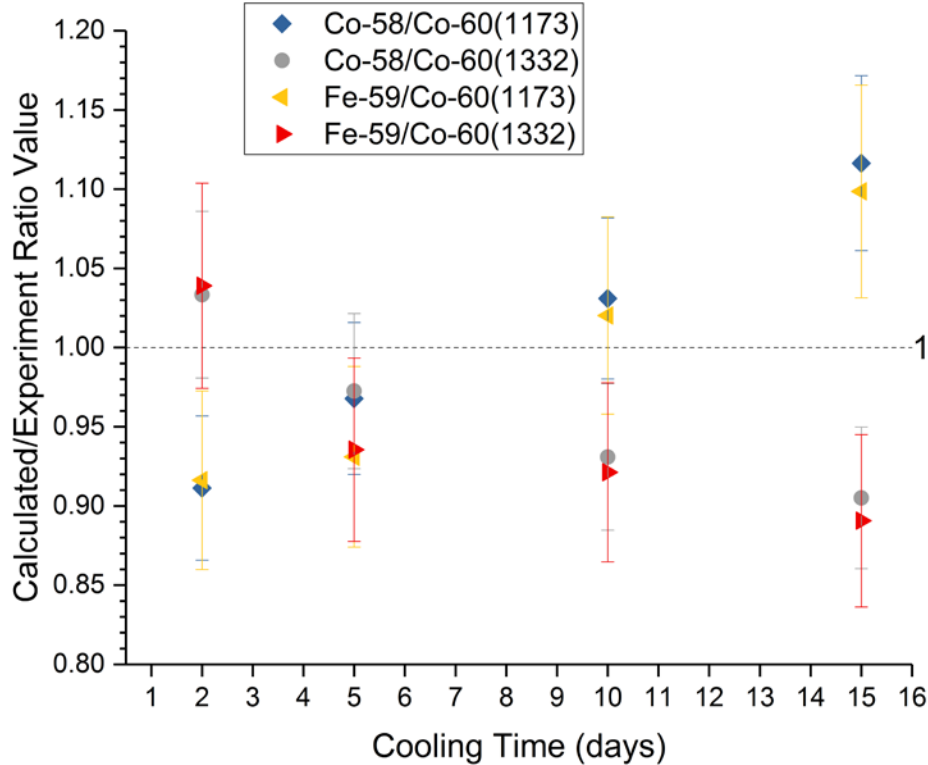


Figure 5.7 Decay time dependence of ^{60}Co based activation product ratios in the SS-L foil as determined by HPGGe simulation. C/E results are given with 1-sigma uncertainty.

For the 1173 keV peak of ^{60}Co , the relative change in simulated peak area between the 2 day and 15 day time steps is less than 0.1%. The 1173 keV peak area would be expected to increase, as seen with the 1332 keV peak, since both gamma-ray lines have similar intensities and are close enough to experience similar changes in background. The constant behavior can be attributed to the presence of ^{132}I , which has an 1172.9 keV line, interfering with the 1173 keV line of ^{60}Co . If the calculated ^{60}Co at 1173 keV was all ^{60}Co , then the simulated peak area would increase, as is seen with the 1332 keV peak. However, ^{132}I has a half-life of only 2.295 hours, causing the 1173 keV peak to remain constant as the ^{132}I decays away. It should be noted that ^{132}I

is in secular equilibrium with its parent, ^{132}Te , which was detected in the SS-L foil during the experiment. This causes the ^{132}I interference to persist, but its effect decreases with time. Taking this into consideration, the trend seen for the 1173 keV based ratios is an increase over the time steps since the amount of ^{60}Co measured by the 1173 keV line is less than it would be without the interference from ^{132}I .

The time dependence shown for the ^{59}Fe based ratios in Fig. 5.5 (Ni foil) is more significant, based on the range of C/E values, than what is seen for the ^{60}Co based ratios in Fig. 5.7 (SS-L foil). Allowing the interference to decay away when production of the desired activation product is low, such as in Fig. 5.5, improves measurement accuracy, as would be expected. For Fig. 5.7, the interferences are more persistent, not leading to measurement improvement over time. The simulated results are most consistent with each other, 1173 keV versus 1332 keV peaks, around 5 days after irradiation. Longer decay times lead to greater inaccuracies, but in this case, results are still within 10% of experiment values.

The time dependence of the ^{59}Fe and ^{60}Co based ratios in the Ni and SS-L foils suggest that there is an optimal measurement window for this work. Separate interferences on the 1173 keV and 1332 keV lines of ^{60}Co lead to statistically different results over time. For the ^{59}Fe based ratios in the Ni foil, the optimal measurement window appears to be for decay times in the 9-11 day range. For the ^{60}Co based ratios in the SS-L foil, the optimal measurement window is for decay times in the 4-7 day range.

5.4 *Conclusions*

This work shows that activation calculations, restricted to a small subset of reactions, cannot adequately predict activation product ratios consistently in Fe, Ni, and stainless steel foils. Therefore, the calculated activation results are unsuitable as the input for measurement simulations. The primary source of error was determined to be the collapsed cross section, including errors in the neutron flux distribution and also in the cross-section data. Secondary activations causing depletion or buildup of desired activation products are not likely to have a significant impact. More work is needed to inspect the neutron flux distribution and the collapsed cross section calculation for oversimplification and other potential errors. Also, sensitivity to the nuclear data library should also be investigated.

Gamma-ray spectroscopy measurements simulated using a MCNP HPGe detector model show that there is no correlation between the ability to measure activation product ratios and the decay time, provided that there are no significant interferences. Specifically, in this work, activation product ratios based on ^{59}Fe in the Ni foil and ^{60}Co in the SS foil showed a slight correlation with decay time. When interferences are present, the choice of decay time can affect accuracy, depending on the characteristics of the interfering nuclide. Allowing the interference to decay away does not impair predictive measurement capabilities, provided that nuclides under consideration are sufficiently active and long-lived. The extent to which gamma-ray spectroscopy measurements are affected by the decay time depends on the specific interference and the ratio being studied.

Chapter 6: Determining the Activation Network of Stainless Steel in Different Neutron Energy Regimes and Decay Scenarios Using Foil Activation Experiments and FISPACT-II Calculations

In this chapter, the activation network of stainless steel grade 304 was explored using the FISPACT-II code and foil irradiations. Both the Flattop critical assembly and the d+Be converter at the University of California-Davis Crocker Nuclear Laboratory were used as neutron sources. Descriptions of the Monte Carlo models that provided the initial neutron flux distributions are described in App. B. Results from different nuclear data libraries were used to assess available cross-section data. Comparisons were made against foil irradiation experiments using both neutron sources in order to validate the Monte Carlo neutron source models. Additionally, comparisons between experimental data from each neutron source were used to evaluate differences between the activation networks. Lastly, the progression of the activation network from Flattop was evaluated with regards to the irradiation time for three different decay times.

6.1 *Introduction*

Neutron activation leads to a diverse collection of radionuclides, dependent on incident neutron energy and the material being irradiated. Activation of composite materials, such as stainless steel, easily generates complex activation networks. Knowing how each component of stainless steel interacts with an ambient radiation

field is important for dose assessment as well as the design of shielding and safety measures to limit worker exposure [68, 69]. Minor differences in stainless steel compositions can lead to significant differences in activation products, which may then require a re-evaluation of shielding and safety measures to limit dose rates.

Activation calculations have been performed using various transmutation codes like MCNP, the ORIGEN module of SCALE, and FISPACT-II [54, 111, 112]. Each of these codes has its own approach and problem constraints. MCNP is the most flexible of these three, being adaptable to almost any situation and allowing for the use of different nuclear data and physics models [84]. The ORIGEN module of SCALE is reliant on the JEFF-3.0/A library only and is limited by its energy group structures, with all of them having a maximum neutron energy of 20 MeV [87]. FISPACT-II is similarly limited in energy group structures but offers coverage of energies beyond 20 MeV and also allows for the use of different nuclear data libraries [86]. ORIGEN is not suitable for this work since the neutron energies involved are known to exceed 20 MeV. The advantages of FISPACT-II over MCNP relevant to this work are the ability to survey the entire activation network without pre-selection of specific reactions and the ability to perform pathway analysis for activation products.

In this work, the activation network of stainless steel grade 304 (SS-304) was investigated using foil activation experiments and the FISPACT-II activation code version 3.00. Two neutron sources covering different energy regimes were used to explore differences in the activation network due to the neutron energy distributions. Production rates normalized to target foil mass were used to make direct comparisons between neutron sources. FISPACT-II results were compared against foil activation

experiments to validate the input neutron distributions and assess the available cross-section data. Additionally, the relationship between the extent of the activation network and the irradiation time was evaluated for decay times of 15 s, 2 d, and 7 d. Advance knowledge of the activation network progression allows for informed decisions to be made regarding material choice, potential dose hazards, and appropriate shielding considerations, as well as aid in the design of experiments.

6.2 Methodology

6.2.1 The Activation Network

The neutron activation network for any given number of target nuclides is defined by the set of neutron capture reactions being considered. Although many reactions are possible, previous work by the authors has focused on only six reactions: (n,γ) , $(n,2n)$, $(n,3n)$, $(n,4n)$, (n,α) , and (n,p) [43, 44]. Figure 6.1 shows the activation map with these six reactions for the naturally occurring isotopes of the major elements in SS-304, namely Fe, Cr, and Ni. In Fig. 6.1, nuclides are shaded based on their role during activation and decay, with the arrows representing each specific reaction. The activation map is complex when limited to only six reactions on three target elements. Several activation products are produced through multiple reactions, while some reactions repopulate other targets or lead to stable activation products. Natural abundances, half-lives, and branching ratios are given where appropriate, using data from the National Nuclear Data Center Chart of the Nuclides [80]. The activation

network that is seen for a particular scenario will depend on the neutron source, irradiation time, and the post-irradiation decay time.

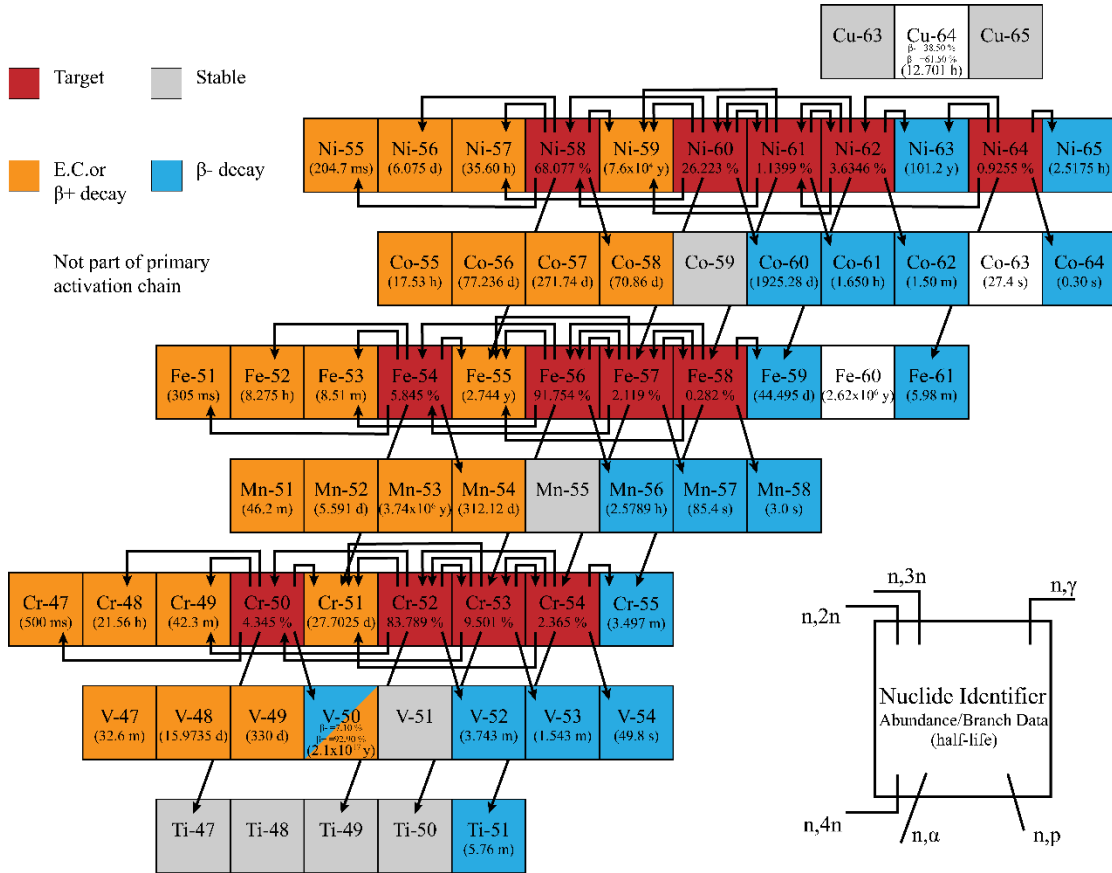


Figure 6.1 Activation map based on the Fe, Cr, and Ni components of stainless steel grade 304, showing the different pathways for the six neutron reactions and the decay modes of activation products.

6.2.2 Foil Activation Experiments

Experimental results were calculated from gamma-ray spectroscopy measurements of activated foils irradiated using the Flattop critical assembly and the d+Be neutron converter at the University of California-Davis (UC Davis). Gamma-ray spectroscopy measurements were performed using a suite of HPGe detectors, with

decay times from 2 to 10 d, and processed using GAMANAL [109]. Experimental flux magnitudes for each source were determined through analysis of the ^{198}Au product from included Au flux monitor foils. The experimental flux magnitude was determined to be $1.306(9)\times 10^{12}$ n cm^{-1} s^{-1} for Flattop and $1.17(3)\times 10^{12}$ n cm^{-1} s^{-1} for UC Davis. Irradiations were for 0.883 h using Flattop and 7 h using UC Davis. The UC Davis irradiation used a deuteron beam energy of 30 MeV and beam current of 10 μA .

6.2.3 *Activation Calculations*

Activation calculations were performed for the irradiation of an SS-304 target foil using FISPACT-II. The target foil composition was based on a SS-304 sample foil from Goodfellow Corporation, which was determined to be 71.21% Fe, 18.39% Cr, 8.05% Ni, 1.81% Mn, and 0.54% Cu using ICP-MS analysis [98]. Calculations were performed using a 709-energy group structure and the TALYS-2014, ENDF/B-VII.1, and JEFF-3.2 cross-section libraries. Total flux magnitudes and irradiation times used in calculations were those given in Sec. 6.2.2.

The Flattop critical assembly consisted of a highly-enriched U core surrounded by a natural U reflector [82]. The UC Davis neutron converter uses a 76-inch cyclotron to supply a deuteron beam, with tunable energy, focused on a ^9Be cylinder [96]. UC Davis neutrons are produced through the d+Be family of neutron sputtering reactions, with the deuteron energy set to 30 MeV. Initial input neutron spectra were flux probability distributions derived from flux tallies in Monte Carlo models of each neutron source. The input distributions were then re-binned to the 709-group structure

in FISPACT-II. Figure 6.2 and Fig. 6.3 show the input neutron energy probability distributions for Flattop and UC Davis, along with the re-binned distributions in the 709-group structure. Figure 6.3 also shows the experimental data available for that facility.

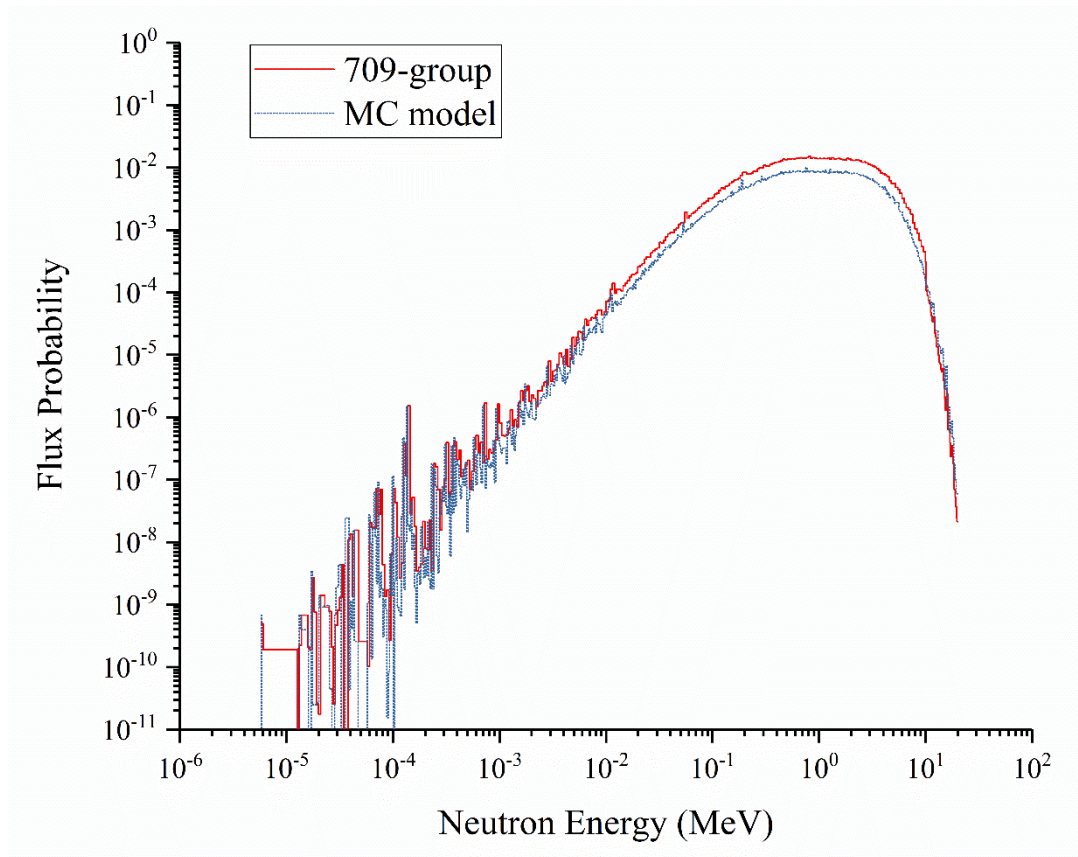


Figure 6.2 Neutron flux probability distributions for the Flattop critical assembly. Dot (blue): Monte Carlo input distribution. Line (red): input re-binned to FISPACT-II 709-group structure.

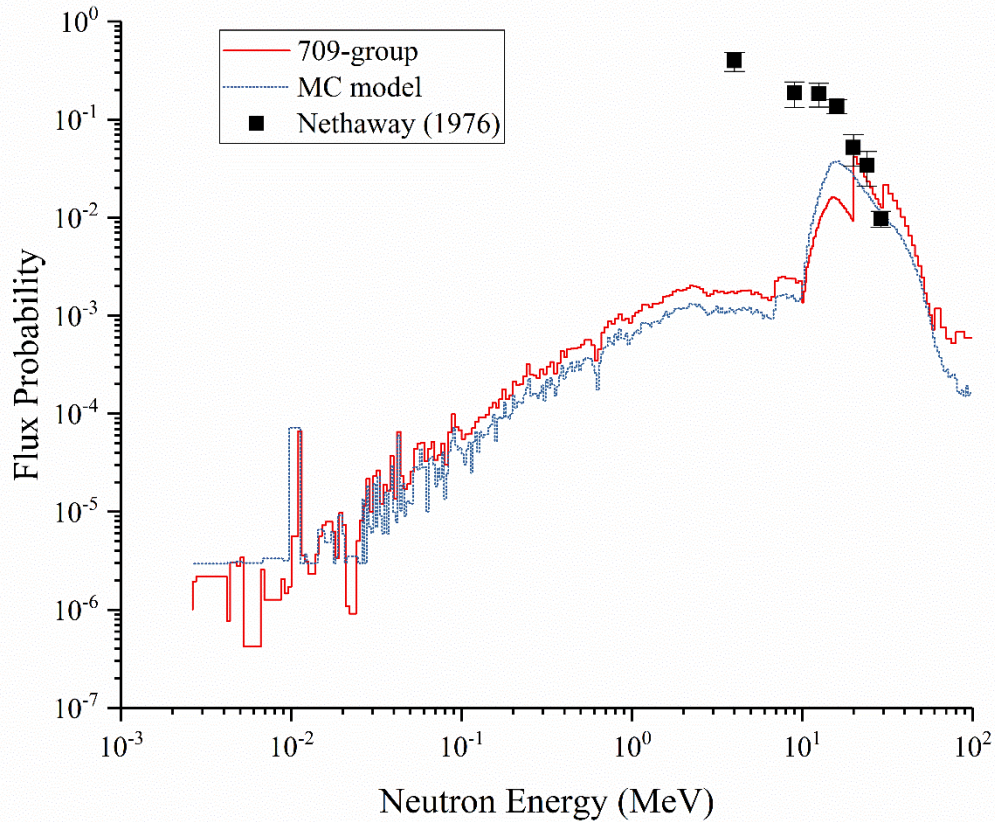


Figure 6.3 Neutron flux probability distributions for the d+Be neutron source at UC Davis. Dot (blue): Monte Carlo input distribution. Line (red): input re-binned to FISPACT-II 709-group structure. Square (black): experiment data [96].

Comparing Fig. 6.2 to Fig. 6.3 shows that Flattop covers a larger energy range and extends to lower neutron energies while UC Davis is shifted toward higher neutron energies. Figure 3 shows that the limited experiment data is not well represented by the multi-group structure, except in the 20-30 MeV range. It is unclear whether the disagreement is from the UC Davis model or the limited experiment data. However, the presence of neutron energies extending up to 100 MeV suggests that there are issues with the UC Davis model that need to be addressed.

Flattop neutron flux probabilities are greater than UC Davis up to approximately 8 MeV. After that, UC Davis has higher probabilities. The Flattop neutron distribution is well represented by the 709-group structure, with the most probable energies in the few MeV range, consistent with the fission of ^{235}U [113]. For the UC Davis Monte Carlo model input distribution, the most probable energies are near 15 MeV, somewhat agreeing with other investigations of the d+Be source [53, 83]. However, re-binning to the 709-group structure distorts the original input distribution, shifting the most probable energies to approximately 20 MeV. The higher energies of the UC Davis neutron spectrum present more reaction channels than are available with Flattop, creating a potential for different activation networks having different production rates.

6.2.4 Production Rates vs Activation Network Progression

Production rates were calculated as saturation activities (A_{sat}), based on nuclide activities at the end of irradiation and corrected for irradiation time using Eq. (6.1).

$$Production\ Rate = A_{sat} = A(t_{irr})[1 - e^{-\lambda t_{irr}}]^{-1} \quad (6.1)$$

The activity at the end of irradiation, from experiment results or activation calculations, is given by $A(t_{irr})$. The irradiation time is t_{irr} and λ is the decay constant for the given nuclide. Production rates were normalized to target foil mass for comparison between sources and are presented in units of atoms $\text{s}^{-1} \text{g}^{-1}$. Production rate ratios were used to compare results between Flattop and UC Davis for common activation products.

A threshold activity was set in order to determine the relationship between the scope of the activation network and irradiation time for three decay scenarios. The threshold activity (A_{thr}) was arbitrarily set to 1 Bq at the time of measurement for this work. Decay times of 15 s, 2 d, and 7 d were chosen as the three decay scenarios. The 15 s decay represents irradiation setups where automatic sample transfer is available. The 2 d and 7 d decay times represent two situations where manual transport of the sample from the irradiation facility to a separate counting facility is required. The irradiation time (t_{irr}) required to achieve A_{thr} at the time of measurement was calculated by rearranging Eq. (6.1) and correcting for the decay time (t_d), resulting in Eq. (6.2):

$$t_{irr} = -\lambda^{-1} \ln \left(1 - \frac{A_{thr} e^{\lambda t_d}}{A_{sat}} \right). \quad (6.2)$$

Values of t_{irr} were calculated for activation products in order to investigate the progression of the activation network with regards to irradiation time.

6.3 Results and Discussion

6.3.1 Input Neutron Distributions and Cross Section Validation

Calculated/Experiment (C/E) ratios, based on foil mass-normalized production rates resulting from Eq. (6.1), were used to validate the input neutron spectra and available neutron reaction data. C/E ratios are presented in Table 6.1 and Table 6.2 for the measured activation products from Flattop and UC Davis foil activation

experiments. Calculated results from FISPACT-II are presented for the TENDL-2014, ENDF/B-VII.1, and JEFF-3.2 libraries.

Table 6.1 C/E values with 1-sigma uncertainty for the Flattop irradiation using available libraries in FISPACT-II

Nuclide	TENDL-14	ENDF/B-VII.1	JEFF-3.2
⁵⁷ Co	1.3(3)	1.05(18)	0.95(17)
⁵⁸ Co	0.73(9)	1.04(3)	1.06(4)
⁶⁰ Co	0.55(12)	0.60(8)	0.68(8)
⁵¹ Cr	0.97(12)	0.96(4)	0.85(12)
⁵⁹ Fe	0.94(3)	1.14(3)	1.04(12)
⁵⁴ Mn	1.07(5)	1.07(3)	0.945(24)

Table 6.2 C/E values with 1-sigma uncertainty for the UC Davis irradiation using available libraries in FISPACT-II

Nuclide	TENDL-14	ENDF/B-VII.1	JEFF-3.2
⁵⁶ Co	88(3)	55.8(14)	8(3)
⁵⁷ Co	19(3)	18.9(9)	12.1(4)
⁵⁸ Co	3.28(22)	5.4(5)	5.05(20)
⁶⁰ Co	10(3)	11.5(8)	10.0(5)
⁵¹ Cr	21(3)	21.9(11)	21.2(11)
⁵⁹ Fe	10.1(24)	8.13(24)	3.9(4)
⁵² Mn	172(25)	233(6)	205(5)
⁵⁴ Mn	17.3(15)	19.0(9)	14.8(4)
⁵⁶ Mn	7.1(16)	7.0(15)	6.9(15)
⁵⁶ Ni	57(4)	28.7(19)	6.9(5)E-04
⁵⁷ Ni	23.3(24)	24.5(7)	12.9(5)
⁴⁸ V	78(10)	62.2(15)	78.0(19)

Tables 6.1 and 6.2 show significant variation in C/E values between the neutron sources. Flattop C/E values span 0.55-1.3, while UC Davis C/E values cover several orders of magnitude. The C/E values in Table 6.1 from the Flattop irradiation are reasonably consistent for each activation product across the different libraries, not immediately identifying a “best” option for the entire set of activation products. The consistency suggests that deviations from C/E=1 result from differences in the available cross-section data, validating the input neutron spectrum for Flattop. Uncertainties in C/E values are driven by uncertainties in the nuclear data, except for ^{57}Co . Based on the relatively low uncertainties, any errors in the Flattop neutron distribution appear to be minor.

The only activation product from the Flattop irradiation that is consistently underestimated across all libraries is ^{60}Co . This finding is consistent with other analysis [40, 68]. This suggests room for improvement in the reaction cross sections leading to the production of ^{60}Co . Pathway analysis performed by FISPACT-II shows that approximately 96% of total ^{60}Co production is from the $^{60}\text{Ni}(n,p)^{60}\text{Co}$ reaction. Therefore, improvements to the (n,p) reaction cross section on ^{60}Ni are needed.

C/E values from UC Davis results in Table 6.2 show much more variation between libraries and are not consistent with the Flattop results. Not a single C/E value is within a factor of 3 of experiment results and there can be a difference of up to several orders of magnitude between library options. Here, the inconsistencies suggest that there are major errors in the input neutron distribution. Additionally, the 709-group structure significantly alters the UC Davis neutron distribution at high energies and may not be the most appropriate group structure for this source. It is unlikely that the

cross sections for the UC Davis nuclides are the major source of error since the Flattop results do not share the same severity of error. Therefore, the Monte Carlo model of the UC Davis neutron source needs to be re-evaluated and experimentally validated using a neutron spectrum unfolding technique. Other energy group structures should also be investigated to alleviate the re-binning issue seen here.

In the results that follow, calculated values are based on the FISPACT-II code using the JEFF-3.2 library option. This selection was made by summing the squares of the deviations of the C/E values from unity for the Flattop results and choosing the lowest value. The UC Davis results were not considered in this decision since there is low confidence in the neutron distribution. Using this method of comparison, the library options from “best” to “worst” are JEFF-3.2, ENDF/B-VII.1, and then TENDL-2014.

6.3.2 Neutron Source Dependence

Comparison of experimental activation yields between neutron sources is done through the calculation of production rate ratios for common activation products. This was accomplished by taking the ratio of the mass-normalized production rates, calculated from experiment data using Eq. (6.1) and the target foil mass, between activation products that were detected in both UC Davis and Flattop irradiations. Common activation products and their experimental production rate ratios are presented in Table 6.3 as the ratio of UC Davis to Flattop.

Table 6.3 Experimental production rate ratios, with 1-sigma uncertainty, between UC Davis and Flattop neutron sources for common activation products

Nuclide	Product Rate Ratio	Uncertainty
⁵⁷ Co	213	± 34
⁵⁸ Co	0.580	± 0.010
⁶⁰ Co	3.6	± 0.3
⁵¹ Cr	33.2	± 0.7
⁵⁹ Fe	1.13	± 0.04
⁵⁴ Mn	1.025	± 0.008

Of the activation products listed in Tables 6.1 and 6.2, ⁵⁷Co, ⁵⁸Co, ⁶⁰Co, ⁵¹Cr, ⁵⁹Fe, and ⁵⁴Mn were quantified in both experiments. ⁵⁹Fe and ⁵⁴Mn have production rate ratios near 1, showing that they are produced at similar rates, regardless of the neutron source. ⁵⁸Co is produced at a faster rate in Flattop than in UC Davis. The nuclides ⁶⁰Co, ⁵¹Cr, and ⁵⁷Co are produced at increasingly higher rates with UC Davis than with Flattop. The higher energy neutron distribution from UC Davis opens up more reaction channels for these activation products and increases the probability of higher energy reactions occurring. Other activation products from UC Davis not detected from Flattop include ⁵⁶Co, ⁵²Mn, ⁵⁶Mn, ⁵⁶Ni, ⁵⁷Ni, and ⁴⁸V.

The original intent of the foil irradiation experiments was not to investigate activation network differences. Therefore, irradiation and decay times were not optimized for activation network visibility. To investigate differences in the activation network not shown by the experiment results, FISPACT-II activation calculations were performed using the JEFF-3.2 library and the 709-group structure. A qualitative evaluation of the extent of the differences in the activation networks between the

activation products. Additional UC Davis activation products covering various isotopes from Si to Sc were also produced by FISPACT-II calculations. However, pathway analysis performed by FISPACT-II gives the (n,O) reaction as a contributing pathway for many activation products. This pathway corresponds to MT=5 in the ENDF list of reaction types, which is a sum of all reactions not explicitly defined by other MT designators. The prevalence of the (n,O) pathway requires additional investigation to determine if many of the nuclides identified in Fig. 6.4 are indeed significant activation products.

6.3.3 *Activation Network Time Progression*

The relationship between the scope of the Flattop activation network and irradiation time was investigated through analysis of the minimum required irradiation time, calculated using Eq. (6.2). Saturation activities for all possible activation products were calculated from FISPACT-II results using the JEFF-3.2 library. The threshold activity at the time of measurement was set to 1 Bq for the 15 s, 2 d, and 7 d decay scenarios. Analysis was performed for the Flattop activation network, but not for the UC Davis network due to low confidence in the UC Davis results, caused by apparent error in the input neutron distribution.

FISPACT-II calculations for Flattop show a maximum of 29 possible activation products, identified in Fig. 6.4. For the 15 s decay period, all but ^{58}Mn are able to meet the threshold activity. The low production rate and short half-life of ^{58}Mn prevent sufficient build-up of the activation product to enable detection, even for a short decay

time. When switching to the 2 d decay period, the number of activation products that meet or exceed the threshold activity of 1 Bq was reduced to 15. The nuclides ^{61}Co , ^{62}Co , ^{49}Cr , ^{55}Cr , ^{62}Cu , ^{66}Cu , ^{53}Fe , ^{61}Fe , ^{56}Mn , ^{57}Mn , ^{65}Ni , ^{51}Ti , ^{52}V , ^{53}V , and ^{54}V were no longer visible. Limited again by production rates and half-lives, these activation products do not reach a sufficient activity level during irradiation to meet or exceed the threshold activity at the time of measurement. The final decay scenario of 7 d only sees the loss of an additional activation product, ^{56}Mn . Of all the activation products, ^{60}Co , ^{55}Fe , ^{53}Mn , ^{59}Ni , and ^{63}Ni were found to have constant respective minimum irradiation times, regardless of the decay scenario. This is due to the combination of high production rates and long half-lives of these activation products.

The irradiation time values can be used to show the number of visible activation products as a function of irradiation time for a given decay scenario and activity threshold. This view is presented in Fig. 6.5 and is analogous to a cumulative distribution of activation products in the activation network with respect to the irradiation time. Each plot shows the irradiation time at which an activation product will exceed the threshold activity at the time of measurement for the given decay scenario. This information becomes useful for experiment planning by allowing researchers to choose an appropriate irradiation time based on their particular decay scenario and the desired extent of the activation network. For example, if ^{59}Ni , ^{56}Co , and ^{53}Mn were deemed insignificant activation products, then the full activation network, determined by ^{49}V production, would exceed the threshold activity after an irradiation time of approximately 13.8 h instead of over 684 a. Additionally, this view enables the anticipation of dose rates based on high activity nuclides for a given set of

irradiation and decay times and threshold activity. With this information, experiment parameters can be adjusted, and additional safety measures can be added or removed as needed. Furthermore, if an undesirable activation product is to be limited or avoided, then this approach can inform decisions on whether or not that material, SS-304 in this case, is appropriate for the given application.

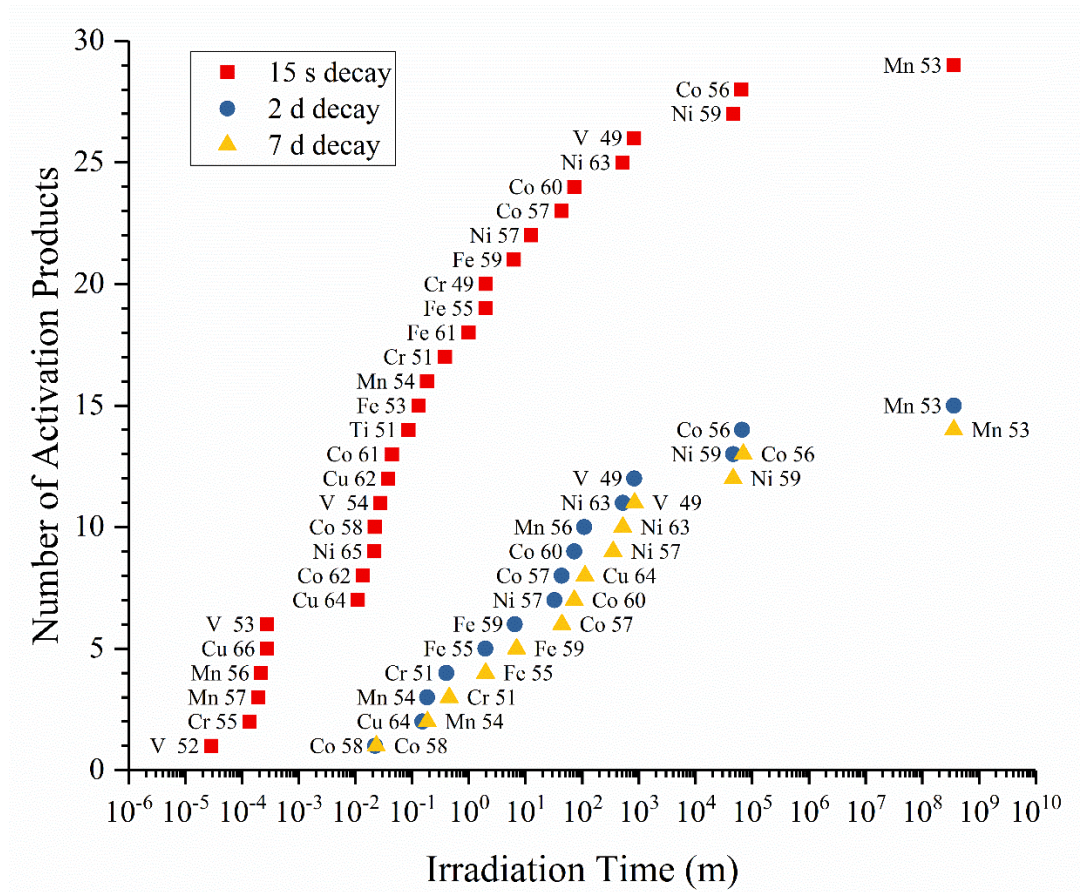


Figure 6.5 The progression of the stainless steel 304 activation network in a Flattop irradiation, for three decay scenarios, having a measurement threshold activity of 1 Bq. Results are based on activation calculations performed using FISPACT-II and the JEFF-3.2 library. Square (red): 15 s decay; Circle (blue): 2 d decay; Triangle (yellow): 7 d decay.

6.4 Conclusions

The FISPACT-II activation code has proven useful for exploring the activation network of stainless steel grade 304 using the Flattop critical assembly. Quantitative results from UC Davis calculations were found to be unreliable due to substantial errors with the input neutron distribution, as suggested by poor C/E values. These errors may be from re-binning to the 709-group structure or from the Monte Carlo model itself. To remedy this, the UC Davis neutron production model needs to be re-evaluated and validated with additional experimental work. Additional group structures should also be investigated. Then, exploration of the activation network using the UC Davis neutron source, and comparison to Flattop, can be revisited using this approach.

Different library options in FISPACT-II produced a range of C/E results, based on foil mass normalized production rates, for detected activation products from the Flattop irradiation. No “best” option was immediately evident, with each library option outperforming others for different activation products. The C/E values of 0.55-0.68 for ^{60}Co are consistent with other analysis and suggest errors in the cross-section data, primarily driven by the $^{60}\text{Ni}(n,p)^{60}\text{Co}$ reaction. C/E values for other activation products range from 0.73 to 1.3 and may be high or low depending on the chosen library. The FISPACT-II code using the JEFF-3.2 library was selected for use in further calculations, as it provided the best C/E results when considering all measured activation products as a set.

Comparison of the activation networks between Flattop and UC Davis showed that there are no activation products unique to Flattop. However, through experimental

production rate ratios, it was found that ^{57}Co , ^{60}Co and ^{51}Cr have higher production rates from UC Davis, while ^{58}Co has a higher production rate from Flattop, and ^{59}Fe and ^{54}Mn are produced at similar rates by each neutron source.

The extent of the Flattop activation network was shown to be sensitive to the decay time between irradiation and measurement. Extending the decay time from 15 s to 2 d reduced the number of activation products that are able to meet the threshold by approximately one half. Further extension of the decay time had little effect. Viewing the activation network as a function of irradiation time provides a cumulative distribution which can be useful for planning future experiments and assessing radiation exposure, as well as the selection of appropriate materials.

The approach used here can easily be extended to other neutron sources and materials, provided the input neutron distribution is an accurate representation of the true neutron energy distribution. Choice of activation code and cross-section library depends on the energy range being used, reactions being investigated, and the activation products being studied. Variations between libraries can be significant and should be evaluated for each particular application and set of activation products.

Chapter 7: Summary

The success of nuclear forensic analysis depends on its ability to be effective in every situation. This requires that signatures be developed for all possible scenarios. As the efforts and intention of adversaries evolve, so to must nuclear forensic signatures. This dissertation has presented an attempt to identify new diagnostic nuclides for further signature development, highlighting the use of simulations as an exploratory tool for nuclear forensics. Simulations have the advantage of being adaptable to many more situations than are experimentally possible while conserving resources and limiting safety hazards to researchers. The objective was to use neutron activation and gamma-ray spectroscopy simulations to identify activation products or ratios that are characteristic of the neutron source responsible for irradiation.

7.1 *Simulation Efficacy*

Signatures are only as useful as the ability to measure them. Therefore, the gamma-ray spectroscopy detector model must meet or exceed the performance of real detectors. Chapter 4 showed that the HPGe model in MCNP, described solely by the manufacturer's specifications, can achieve performance equivalent to real detectors. The only requirements are a detector response function describing Gaussian energy broadening within the detector and an efficiency calibration. Shielding and other peripheral materials are not necessary in the geometry description, a benefit which saves on computation time. Chapter 5 showed that the HPGe detector model can be used to explore different measurement scenarios while providing equivalent or lower

uncertainties than real measurements. The model was used to show that when significant interferences are present, the ability to measure low yield activation products is dependent on the decay time, resulting in an optimal measurement window specific to the activation product and interfering nuclide.

The performance of the measurement simulation is only as good as the activity data of the initial nuclide mixture used to calculate the gamma-ray distribution. If the input for the measurement simulation is flawed, then the results will be flawed as well. Chapters 5 and 6 explored different approaches to calculating activation product yields to be used as input to the measurement simulation. In Chap. 5, theoretical activation calculations were done by hand using a limited set of reactions for activation by the Flattop critical assembly. Calculated/Experimental values of 0.6-1.3 show that the simple approach may not be sufficient to supply input to the measurement simulation. Errors may lie with the reaction cross-section values, the Flattop neutron distribution, or the limited selection of reactions.

In Chap. 6, the FISPACT-II activation code was used to evaluate the entire activation network of stainless steel. Results for the simulation of activation from Flattop are consistent with what was observed in Chap. 5, as shown in Table 7.1, validating the neutron distribution and selection of reaction pathways. Errors are then the result of the cross-section values for each reaction. Chapter 6 also simulated activation by the d+Be neutron converter at UC Davis, but results varied widely from experimental values. The range of results shows that the UC Davis model neutron distribution is severely flawed.

Table 7.1 Comparison of foil mass-normalized production rates for theoretical activation calculations based on Flattop irradiation done by hand and with the FISPACT-II code for different nuclear data libraries, with 1-sigma uncertainty.

Nuclide	Hand Calculation	FISPACT-II Calculation		
	ENDF/B-V.11	TENDL-14	ENDF/B-V.11	JEFF-3.2
⁵⁸ Co	1.070(20)	0.73(9)	1.04(3)	1.06(4)
⁶⁰ Co	0.61(5)	0.55(12)	0.60(8)	0.68(8)
⁵¹ Cr	1.00(3)	0.97(12)	0.96(4)	0.85(12)
⁵⁹ Fe	0.93(3)	0.94(3)	1.14(3)	1.04(12)
⁵⁴ Mn	1.100(13)	1.07(5)	1.07(3)	0.945(24)

Also in Chap. 6, comparison of experimental production rates between UC Davis and Flattop showed that ⁵⁷Co, ⁵⁸Co, ⁶⁰Co, ⁵¹Cr, ⁵⁹Fe, and ⁵⁴Mn are activation products that could prove useful in future signature development. Experimental results also showed that ⁵⁶Co, ⁵²Mn, ⁵⁶Mn, ⁵⁶Ni, ⁵⁷Ni, and ⁴⁸V are activation products unique to UC Davis, for the given experimental conditions. The nuclides ⁵⁹Fe and ⁵⁴Mn are produced at almost the same rates by both neutron sources, while ⁵⁷Co, ⁶⁰Co and ⁵¹Cr have higher production rates with UC Davis and ⁵⁸Co has a higher production rate with Flattop. Ratios built on these activation products could then be used to identify or eliminate possible neutron sources.

Examples of possible activation product production rate ratios using ⁵⁷Co, ⁵⁸Co, ⁶⁰Co, ⁵¹Cr, ⁵⁹Fe, and ⁵⁴Mn are shown in Fig. 7.1 for experimental and simulated production rates. Also, the activation product ratios discussed in Chap. 5 have been included, and inverted where necessary. The relative changes between the simulated and experimental results further support the validation of the Flattop distribution and the large errors in the UC Davis distribution. Since ⁵⁹Fe and ⁵⁴Mn have production rate ratios between sources close to a value of 1, activation product production rate ratios

relative to these nuclides can be indicative of the neutron source. This is because both ^{59}Fe and ^{54}Mn are produced at approximately the same rate by UC Davis and Flattop. Therefore, the ratio of the production rates relative to ^{59}Fe or ^{54}Mn will be specific to the neutron source.

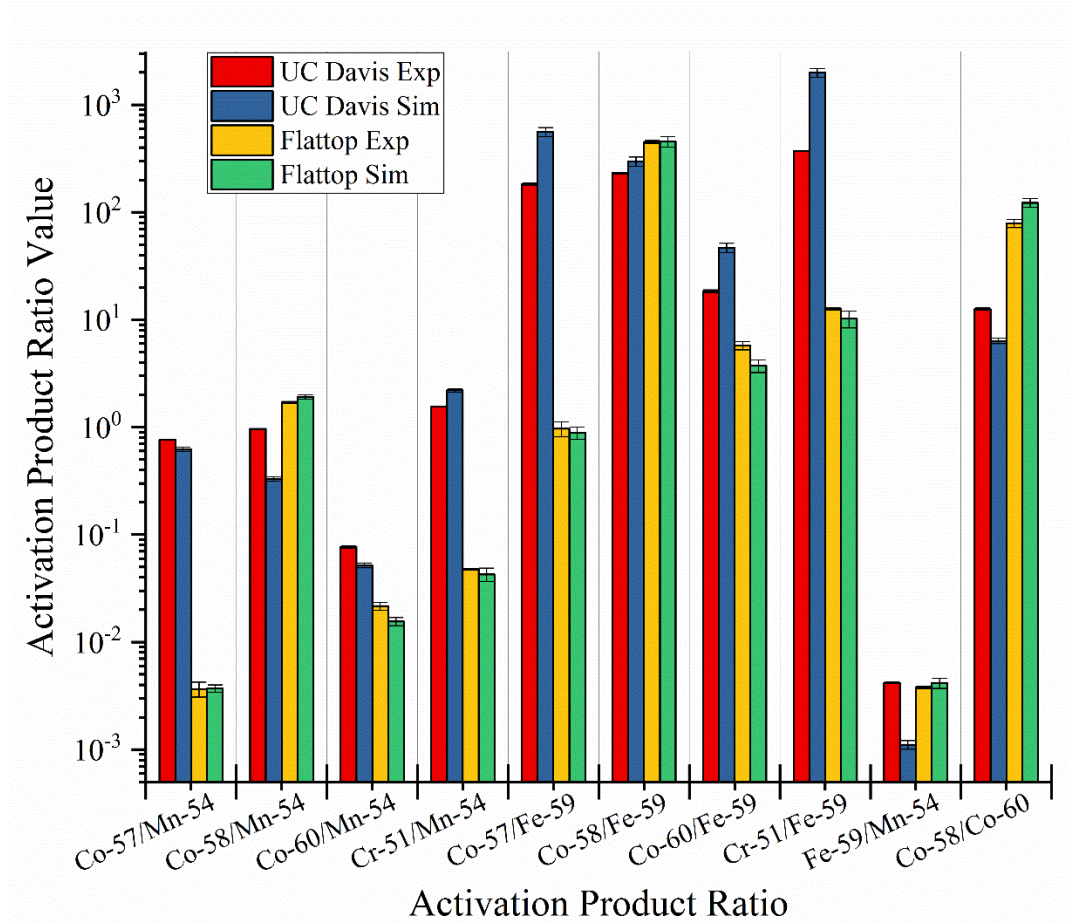


Figure 7.1 Activation product ratios based on simulated and experimental production rates from the Flattop and UC Davis neutron sources. Significant changes between UC Davis and Flattop identify ratios that may be useful as nuclear forensic signatures. Simulated values are calculated from FISPACT-II results with the JEFF-3.2 library.

Ratios with larger differences between UC Davis and Flattop values are better suited for neutron source identification. If values are reasonably close, then the identification may become ambiguous, especially if there is large experimental

uncertainty. Activation product ratios that have the most potential as nuclear forensic signatures of the Flattop or UC Davis neutron sources are $^{57}\text{Co}/^{54}\text{Mn}$, $^{51}\text{Cr}/^{54}\text{Mn}$, $^{57}\text{Co}/^{59}\text{Fe}$, and $^{51}\text{Cr}/^{59}\text{Fe}$. This is consistent with the experimental comparison in Chap. 6, since ^{57}Co had the most extreme ratio difference between neutron sources, followed by ^{51}Cr .

FISPACT-II calculations in Chap. 6 showed that there are no activation products unique to Flattop activation, relative to UC Davis activation. However, there are many potential activation products unique to the UC Davis source. Unfortunately, there is low confidence in the UC Davis model neutron distribution, which is why the UC Davis results are regarded as potential activation network differences. Also, the low confidence in the UC Davis model neutron distribution prevented a quantitative comparison of production rates for other common activation products produced by both neutron sources.

The work in Chap. 6 also showed the effect of decay time on the activation network progression for Flattop. Again, a similar analysis could not be made for UC Davis due to the errors in the model neutron distribution. For Flattop, the experimental shared activation products are not affected by decay time, at least out to 7 d. However, even though ^{56}Co , ^{56}Mn , and ^{57}Ni are not experimental shared activation products, they are simulated shared activation products according to FISPACT-II calculations. Of these three simulated shared activation products, only ^{56}Mn is sensitive to the decay time, making it unattractive for signature development. The nuclides ^{56}Co and ^{57}Ni require further investigation with a validated neutron distribution from UC Davis.

7.2 *Future Outlook*

This work clearly shows that the current evaluation of the UC Davis neutron distribution is inadequate for activation calculations. Improvements to the Monte Carlo model are necessary if the UC Davis neutron distribution is to be used in future work. The different physics options and d+Be reaction cross sections need to be thoroughly investigated to tune the model. A deliberate evaluation of the experimental neutron spectrum through neutron spectrum unfolding methods is also required to validate the model. Only then can this work be revisited to further explore differences in activation products and production rates between the UC Davis and Flattop neutron sources.

A careful evaluation of available cross-section data should also be completed as new data library evaluations are released. At the time of this work, a major update to the ENDF library is pending, which includes changes to the evaluated $^{60}\text{Ni}(n,p)^{60}\text{Co}$ cross section. Once officially released, the activation calculations should be performed again to determine if further improvements are needed. Any deficiencies in the evaluated cross sections should be announced to the nuclear data community.

When provided with accurate neutron distributions and cross-section data, additional materials can be investigated using these simulations to develop new signatures based on activation products for nuclear forensic analysis. If activation calculations can provide accurate irradiation yields, differences between neutron sources can be exploited to create comparative fingerprints for each neutron source. When activation yields are reliable, they can be used as initial input data to explore different measurement scenarios with the HPGe detector model. Activation product

gamma-ray distributions can be combined with fission product spectra, and other complicating factors, to determine optimal measurement windows or whether measurement of the desired activation product is possible in a complex sample. Together, the simulation of neutron activation calculations and gamma-ray spectroscopy measurements provide useful tools for exploring different materials for new nuclear forensic signatures based on activation products

Appendix A: Equation Derivations

Derivations for Chap. 2 equations describing nuclide decay, Eqs. (2.1) – (2.5), neutron activation, Eqs. (2.6) and (2.7) along with the saturation value, and Compton scattering, Eq. (2.8), are presented here. Additionally, the expression for the simulated activation product ratio value, Eq. (4.3), and the depletion reactions through secondary activation, Eq. (5.5), are derived as well.

A.1 Nuclide Decay

Radioactive decay of unstable nuclides is a random process that follows first order kinetics, meaning that the rate of decay is proportional to the amount of substance, the number of nuclei in this case. Therefore, the rate equation for the decay of nuclide A is:

$$dN_A/dt = -\lambda_A N_A, \quad (A.1)$$

where λ_A is the decay constant for nuclide A. The rate is negative relative to the population of A (N_A) since A is disappearing. Rearranging and integrating gives:

$$\frac{dN_A}{N_A} = -\lambda_A dt, \quad (A.2)$$

$$\int \frac{dN_A}{N_A} = -\lambda_A \int dt, \quad (A.3)$$

$$\ln N_A = -\lambda_A t + C, \quad (A.4)$$

where C is the constant of integration. For the initial condition of $N_A=N_0$ at $t=0$, the constant of integration becomes $C = \ln N_0$. Substituting for C in Eq. (A.4) gives:

$$\ln N_A = -\lambda_A t + \ln N_0, \quad (A.5)$$

$$\ln N_A - \ln N_0 = -\lambda_A t, \quad (A.6)$$

$$\ln \frac{N_A}{N_0} = -\lambda_A t, \quad (A.7)$$

$$\frac{N_A}{N_0} = e^{-\lambda_A t}, \quad (A.8)$$

$$N_A = N_0 e^{-\lambda_A t}, \quad (A.9)$$

which is a variation of Eq. (2.2) where t is the elapsed time of the decay period.

Eq. (A.9) can then be used to derive the expression for the half-life. Setting $N_A=N_0/2$ gives:

$$\frac{N_0}{2} = N_0 e^{-\lambda_A t}, \quad (A.10)$$

$$\frac{N_0}{2N_0} = e^{-\lambda_A t}, \quad (A.11)$$

$$\frac{1}{2} = e^{-\lambda_A t}. \quad (A.12)$$

Taking the natural logarithm of both sides and solving for t gives:

$$\ln \frac{1}{2} = \ln(e^{-\lambda_A t}), \quad (A.13)$$

$$\ln \frac{1}{2} = -\lambda_A t, \quad (A.14)$$

$$-\ln \frac{1}{2} / \lambda_A = t, \quad (A.15)$$

$$t_{1/2} = t = \ln 2/\lambda_A, \quad (A.16)$$

which is Eq. (2.3) for the half-life of a given radionuclide.

For the case of decay where the parent (A) decays to the daughter (B) which then also decays, the rate equation for the daughter includes the decay of the daughter as well as growth from the decay of the parent. This results in:

$$dN_B/dt = -\lambda_B N_B + \lambda_A N_A. \quad (A.17)$$

Solving this first-order linear differential equation begins by rearranging, then multiplying both sides by $e^{\lambda_B t}$ and distributing, giving:

$$\left[\frac{dN_B}{dt} + \lambda_B N_B = \lambda_A N_A \right] e^{\lambda_B t}, \quad (A.18)$$

$$\frac{dN_B}{dt} e^{\lambda_B t} + \lambda_B N_B e^{\lambda_B t} = \lambda_A N_A e^{\lambda_B t}, \quad (A.19)$$

The left-hand side of Eq. (A.19) reduces to the derivative of $e^{\lambda_B t}$ with respect to t .

Substituting N_A with the expression given in Eq. (A.9) and simplifying gives:

$$\frac{d}{dt} (N_B e^{\lambda_B t}) = \lambda_A N_{A0} e^{-\lambda_A t} e^{\lambda_B t}, \quad (A.20)$$

$$\frac{d}{dt} (N_B e^{\lambda_B t}) = \lambda_A N_{A0} e^{t(\lambda_B - \lambda_A)}. \quad (A.21)$$

Integrating gives:

$$N_B e^{\lambda_B t} = \lambda_A N_{A0} \int e^{t(\lambda_B - \lambda_A)} dt, \quad (A.22)$$

$$N_B e^{\lambda_B t} = \frac{\lambda_A N_{A0}}{\lambda_B - \lambda_A} e^{t(\lambda_B - \lambda_A)} + K, \quad (A.23)$$

where K is the constant of integration. Solving for K with the initial condition that $N_B=0$ at $t=0$, substituting the result, and simplifying gives:

$$K = -\frac{\lambda_A N_{A0}}{\lambda_B - \lambda_A}, \quad (\text{A.24})$$

$$N_B e^{\lambda_B t} = \frac{\lambda_A N_{A0}}{\lambda_B - \lambda_A} e^{t(\lambda_B - \lambda_A)} - \frac{\lambda_A N_{A0}}{\lambda_B - \lambda_A}, \quad (\text{A.25})$$

$$N_B = \left(\frac{\lambda_A N_{A0}}{\lambda_B - \lambda_A} e^{t(\lambda_B - \lambda_A)} - \frac{\lambda_A N_{A0}}{\lambda_B - \lambda_A} \right) e^{-\lambda_B t}, \quad (\text{A.26})$$

$$N_B = \frac{\lambda_A N_{A0}}{\lambda_B - \lambda_A} e^{t(\lambda_B - \lambda_A)} e^{-\lambda_B t} - \frac{\lambda_A N_{A0}}{\lambda_B - \lambda_A} e^{-\lambda_B t}, \quad (\text{A.27})$$

$$N_B = \frac{\lambda_A N_{A0}}{\lambda_B - \lambda_A} e^{-t\lambda_A} - \frac{\lambda_A N_{A0}}{\lambda_B - \lambda_A} e^{-\lambda_B t}, \quad (\text{A.28})$$

$$N_B = \frac{\lambda_A N_{A0}}{\lambda_B - \lambda_A} (e^{-t\lambda_A} - e^{-\lambda_B t}), \quad (\text{A.29})$$

which is Eq. (2.5).

A.2 Neutron Activation and Depletion

The rate of nuclide production for a single neutron capture reaction is determined by the difference between the production and decay terms. The production term is determined by the number of target nuclei (n_0) the total flux magnitude (Φ_T), and the flux weighted 1-group cross section ($\bar{\sigma}$). The decay term is equal to Eq. (A.1). The resulting rate equation is for the production of P is:

$$dN_p/dt = n_0 \Phi_T \bar{\sigma} - \lambda_p N_p. \quad (\text{A.30})$$

Rearranging, using the same multiplicative factor as with the multistep decay equation, and simplifying gives:

$$\frac{dN_p}{dt} + \lambda_p N_p = n_0 \Phi_T \bar{\sigma}, \quad (\text{A.31})$$

$$\left[\frac{dN_p}{dt} + \lambda_p N_p = n_0 \Phi_T \bar{\sigma} \right] e^{\lambda_p t}, \quad (\text{A.32})$$

$$\frac{dN_p}{dt} e^{\lambda_p t} + \lambda_p N_p e^{\lambda_p t} = n_0 \Phi_T \bar{\sigma} e^{\lambda_p t}, \quad (\text{A.33})$$

$$\frac{d}{dt} (N_p e^{\lambda_p t}) = n_0 \Phi_T \bar{\sigma} e^{\lambda_p t}. \quad (\text{A.34})$$

Integrating gives:

$$N_p e^{\lambda_p t} = n_0 \Phi_T \bar{\sigma} \int e^{\lambda_p t} dt, \quad (\text{A.35})$$

$$N_p e^{\lambda_p t} = \frac{n_0 \Phi_T \bar{\sigma}}{\lambda_p} e^{\lambda_p t} + H, \quad (\text{A.36})$$

where H is the constant of integration. Solving for H with the initial condition that $N_p=0$ at $t=0$, substituting the result into Eq. (A.36) gives:

$$H = -\frac{n_0 \Phi_T \bar{\sigma}}{\lambda_p}, \quad (\text{A.37})$$

$$N_p e^{\lambda_p t} = \frac{n_0 \Phi_T \bar{\sigma}}{\lambda_p} e^{\lambda_p t} - \frac{n_0 \Phi_T \bar{\sigma}}{\lambda_p}, \quad (\text{A.38})$$

$$N_p = \frac{n_0 \Phi_T \bar{\sigma}}{\lambda_p} e^{\lambda_p t} e^{-\lambda_p t} - \frac{n_0 \Phi_T \bar{\sigma}}{\lambda_p} e^{-\lambda_p t}, \quad (\text{A.39})$$

$$N_p = \frac{n_0 \Phi_T \bar{\sigma}}{\lambda_p} (1 - e^{-\lambda_p t}), \quad (\text{A.40})$$

which is Eq. (2.7) and Eq. (5.1).

Secondary activations on primary activation products constitute depletion reactions. When this occurs, the rate of production of P, Eq. (A.30), is further reduced by the activation expression for the secondary reaction. The secondary activation term

is defined in the same way as the production term for the primary activation equation, where $\bar{\sigma}_s$ is the flux weighted 1-group cross section for the secondary reaction. The resulting rate equation is:

$$dN_p/dt = n_0\Phi_T\bar{\sigma}_p - \lambda_p N_p - N_p\Phi_T\bar{\sigma}_s. \quad (A.41)$$

Rearranging and simplifying gives:

$$dN_p/dt + \lambda_p N_p + N_p\Phi_T\bar{\sigma}_s = n_0\Phi_T\bar{\sigma}_p, \quad (A.42)$$

$$dN_p/dt + N_p(\lambda_p + \Phi_T\bar{\sigma}_s) = n_0\Phi_T\bar{\sigma}_p. \quad (A.43)$$

To solve this differential equation, the multiplicative factor is $e^{t(\lambda_p + \Phi_T\bar{\sigma}_s)}$, which again allows for the reduction of the left-hand side of Eq. (A.43) via the power rule.

Simplifying and integrating the result gives:

$$[dN_p/dt + N_p(\lambda_p + \Phi_T\bar{\sigma}_s) = n_0\Phi_T\bar{\sigma}_p]e^{t(\lambda_p + \Phi_T\bar{\sigma}_s)}, \quad (A.44)$$

$$\frac{dN_p}{dt}e^{t(\lambda_p + \Phi_T\bar{\sigma}_s)} + N_p(\lambda_p + \Phi_T\bar{\sigma}_s)e^{t(\lambda_p + \Phi_T\bar{\sigma}_s)} = n_0\Phi_T\bar{\sigma}_pe^{t(\lambda_p + \Phi_T\bar{\sigma}_s)}, \quad (A.45)$$

$$\frac{d}{dt}(N_pe^{t(\lambda_p + \Phi_T\bar{\sigma}_s)}) = n_0\Phi_T\bar{\sigma}_pe^{t(\lambda_p + \Phi_T\bar{\sigma}_s)}, \quad (A.46)$$

$$N_pe^{t(\lambda_p + \Phi_T\bar{\sigma}_s)} = n_0\Phi_T\bar{\sigma}_p \int e^{t(\lambda_p + \Phi_T\bar{\sigma}_s)} dt, \quad (A.47)$$

$$N_pe^{t(\lambda_p + \Phi_T\bar{\sigma}_s)} = \frac{n_0\Phi_T\bar{\sigma}_p}{\lambda_p + \Phi_T\bar{\sigma}_s} e^{t(\lambda_p + \Phi_T\bar{\sigma}_s)} + G, \quad (A.48)$$

where G is the constant of integration. Solving for G with the initial same initial condition as for the primary activation equation, substituting into Eq. (A.48), and simplifying gives:

$$G = -\frac{n_0\Phi_T\bar{\sigma}_p}{\lambda_p+\Phi_T\bar{\sigma}_s}, \quad (A.49)$$

$$N_p e^{t(\lambda_p+\Phi_T\bar{\sigma}_s)} = \frac{n_0\Phi_T\bar{\sigma}_p}{\lambda_p+\Phi_T\bar{\sigma}_s} e^{t(\lambda_p+\Phi_T\bar{\sigma}_s)} - \frac{n_0\Phi_T\bar{\sigma}_p}{\lambda_p+\Phi_T\bar{\sigma}_s}, \quad (A.50)$$

$$N_p = \frac{n_0\Phi_T\bar{\sigma}_p}{\lambda_p+\Phi_T\bar{\sigma}_s} e^{t(\lambda_p+\Phi_T\bar{\sigma}_s)} e^{-t(\lambda_p+\Phi_T\bar{\sigma}_s)} - \frac{n_0\Phi_T\bar{\sigma}_p}{\lambda_p+\Phi_T\bar{\sigma}_s} e^{-t(\lambda_p+\Phi_T\bar{\sigma}_s)}, \quad (A.51)$$

$$N_p = \frac{n_0\Phi_T\bar{\sigma}_p}{\lambda_p+\Phi_T\bar{\sigma}_s} [1 - e^{-t(\lambda_p+\Phi_T\bar{\sigma}_s)}], \quad (A.52)$$

which is equivalent to Eq. (5.5).

A.3 *The Compton Scattering of Gamma rays*

The scattering of gamma-ray photons through collisions with electrons in an absorbing material requires the conservation of energy and momentum in relativistic terms. The geometry of a Compton scattering event is shown in Fig. A.1. The subscripts of γ , e , i , and f denote the photon and electron energies (E) and momenta (p) of the initial and final states.

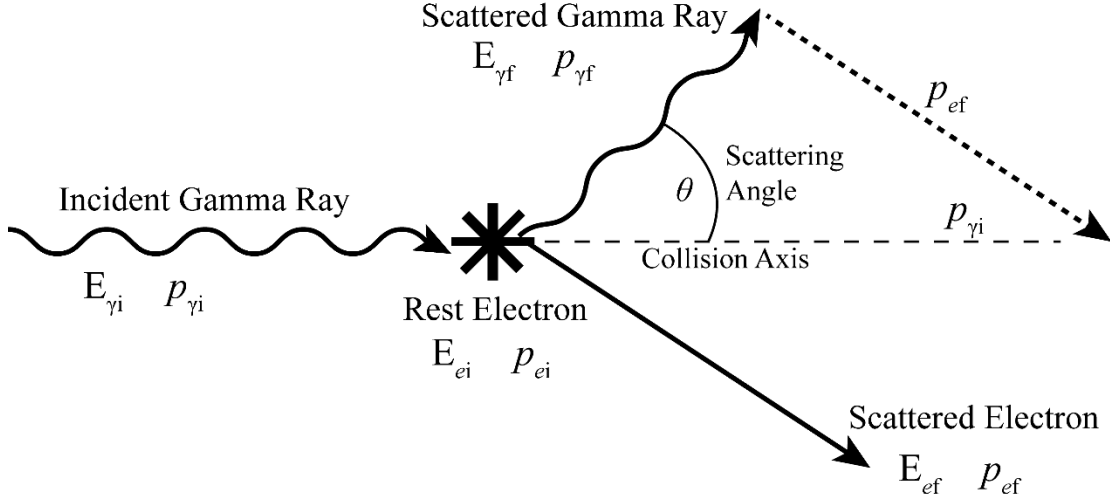


Figure A.1 The geometry of a Compton scattering event where energy and momentum must be conserved. The final momentum of the scattered electron is duplicated as dotted line to show vector addition for the conservation of momentum.

Relativistic kinematics states that the energy of a particle is determined by its momentum (p) and rest-mass (m_o) according to:

$$E_T^2 = (pc)^2 + (m_o c^2)^2, \quad (\text{A.53})$$

where c is the speed of light. For a photon having no mass, $E_T = E_{\gamma i} = p_{\gamma i} c$ prior to the collision. For an electron at rest relative to the incident photon, $E_T = E_{ei} = m_e c^2$, where m_e is the rest-mass of an electron. The final states of each particle are then $E_{\gamma f} = p_{\gamma f} c$ and $E_{ef}^2 = (p_{ef} c)^2 + (m_e c^2)^2$. The conservation of energy gives:

$$E_{\gamma i} + E_{ei} = E_{\gamma f} + E_f, \quad (\text{A.54})$$

$$E_{\gamma i} + m_e c^2 = E_{\gamma f} + \sqrt{(p_{ef} c)^2 + (m_e c^2)^2}, \quad (\text{A.55})$$

$$(E_{\gamma i} - E_{\gamma f} + m_e c^2)^2 = p_{ef}^2 c^2 + m_e^2 c^4. \quad (\text{A.56})$$

The scattering angle (θ) can be calculated by applying the law of cosines to the conservation of momentum with vector addition, resulting in:

$$p_{ef}^2 = p_{\gamma i}^2 + p_{\gamma f}^2 - 2p_{\gamma i}p_{\gamma f} \cos \theta. \quad (\text{A.57})$$

Substituting Eq. (A.57) in to Eq. (A.56) gives:

$$(E_{\gamma i} - E_{\gamma f} + m_e c^2)^2 = p_{\gamma i}^2 c^2 + p_{\gamma f}^2 c^2 - 2p_{\gamma i}p_{\gamma f} c^2 \cos \theta + m_e^2 c^4. \quad (\text{A.58})$$

Expanding the left-hand side (LHS), applying the relationship between photon energy and momentum of $E = pc$ to the right-hand side (RHS), and canceling terms gives:

$$LHS = E_{\gamma i}^2 + E_{\gamma f}^2 - 2E_{\gamma i}E_{\gamma f} + 2E_{\gamma i}m_e c^2 - 2E_{\gamma f}m_e c^2 + m_e^2 c^4, \quad (\text{A.59})$$

$$RHS = p_{\gamma i}^2 c^2 + p_{\gamma f}^2 c^2 - 2p_{\gamma i}p_{\gamma f} c^2 \cos \theta + m_e^2 c^4, \quad (\text{A.60})$$

$$RHS = E_{\gamma i}^2 + E_{\gamma f}^2 - 2E_{\gamma i}E_{\gamma f} \cos \theta + m_e^2 c^4, \quad (\text{A.61})$$

$$-E_{\gamma i}E_{\gamma f} + E_{\gamma i}m_e c^2 - E_{\gamma f}m_e c^2 = -E_{\gamma i}E_{\gamma f} \cos \theta. \quad (\text{A.62})$$

Rearranging and simplifying gives:

$$E_{\gamma i}m_e c^2 - E_{\gamma f}m_e c^2 = E_{\gamma i}E_{\gamma f} - E_{\gamma i}E_{\gamma f} \cos \theta, \quad (\text{A.63})$$

$$E_{\gamma i}m_e c^2 = E_{\gamma i}E_{\gamma f}(1 - \cos \theta) + E_{\gamma f}m_e c^2, \quad (\text{A.64})$$

$$E_{\gamma i} = \frac{E_{\gamma i}E_{\gamma f}}{m_e c^2}(1 - \cos \theta) + E_{\gamma f}, \quad (\text{A.65})$$

$$E_{\gamma i} = E_{\gamma f} \left[\frac{E_{\gamma i}}{m_e c^2}(1 - \cos \theta) + 1 \right], \quad (\text{A.66})$$

$$\frac{E_{\gamma i}}{1 + \frac{E_{\gamma i}}{m_e c^2}(1 - \cos \theta)} = E_{\gamma f}, \quad (A.67)$$

which is equivalent to Eq. (2.8).

A.4 *The Simulated Activation Product Ratio*

Simulated activation product ratios in Chap. 4 and Chap. 5 were calculated based on analysis of the simulated gamma-ray spectra created with the MCNP model. The activity (A) of a given nuclide at the time of measurement is determined by the calculated peak area (PA) in net counts divided by the counting time (t_c), the probability of emission of the gamma ray being used (P_γ), and the photopeak efficiency (ε_γ) for that specific gamma ray on the detector being used, which gives:

$$A = \frac{PA}{t_c \varepsilon_\gamma P_\gamma}. \quad (A.68)$$

The population of the activation product at the end of irradiation can be determined by converting from activity to nuclide population and correcting for the decay time between the end of irradiation and measurement. The conversion from activity to population uses the relationship of $A = \lambda N$:

$$A_m = \lambda N_m = \frac{PA}{t_c \varepsilon_\gamma P_\gamma}, \quad (A.69)$$

$$N_m = \frac{PA}{t_c \varepsilon_\gamma P_\gamma}, \quad (A.70)$$

where N_m is the population at the time of measurement. The decay time correction uses the relationship given in Eq. (A.9) to calculate the population and the end of irradiation (N_0), where N_m is the population at the time of measurement, giving:

$$N_m = N_0 e^{-\lambda_A t} \rightarrow N_0 = N_m e^{\lambda t}. \quad (\text{A.71})$$

Combining Eqs. (A.70) and (A.71) gives:

$$N_0 = \frac{PA}{t_c \varepsilon_\gamma P_\gamma} e^{\lambda t}. \quad (\text{A.72})$$

Taking the ratio of two activation products from the same measurement (N_1 and N_2) and simplifying gives:

$$\frac{N_1}{N_2} = \frac{\frac{PA_1}{t_c \varepsilon_{\gamma 1} P_{\gamma 1} \lambda_1} e^{\lambda_1 t}}{\frac{PA_2}{t_c \varepsilon_{\gamma 2} P_{\gamma 2} \lambda_2} e^{\lambda_2 t}}, \quad (\text{A.73})$$

$$\frac{N_1}{N_2} = \frac{PA_1 \varepsilon_{\gamma 2} P_{\gamma 2} \lambda_2}{PA_2 \varepsilon_{\gamma 1} P_{\gamma 1} \lambda_1} e^{t(\lambda_1 - \lambda_2)}, \quad (\text{A.74})$$

which is equivalent to Eq. (4.3).

Appendix B: Simulation Descriptions and Input Files

Each of the simulations used in this work are described here in greater detail: the HPGe detector model, neutron production with the University of California-Davis campus d+Be converter and the Flattop critical assembly, and neutron activation calculations with FISPACT-II. Input files for use with MCNP are included for the HPGe detector and neutron source models, as well as those necessary for neutron activation using FISPACT-II.

B.1 The HPGe Model

The HPGe detector model in MCNP was based on an existing detector at the Lawrence Livermore National Laboratory Nuclear Counting Facility. The physical detector was an ORTEC GEM series p-type coaxial HPGe detector. Only the detector capsule itself was modeled, using dimensions from the manufacturer specification sheet. All composite material descriptions were taken from the Pacific Northwest National Laboratory Materials Compendium [99]. Corrections for the bulletization of the physical crystal were not included. A cylindrical shield was included in some simulations, consisting of Cd, Cu, Pb, and generic steel. A schematic representation of the shield is shown in Fig. B.1.

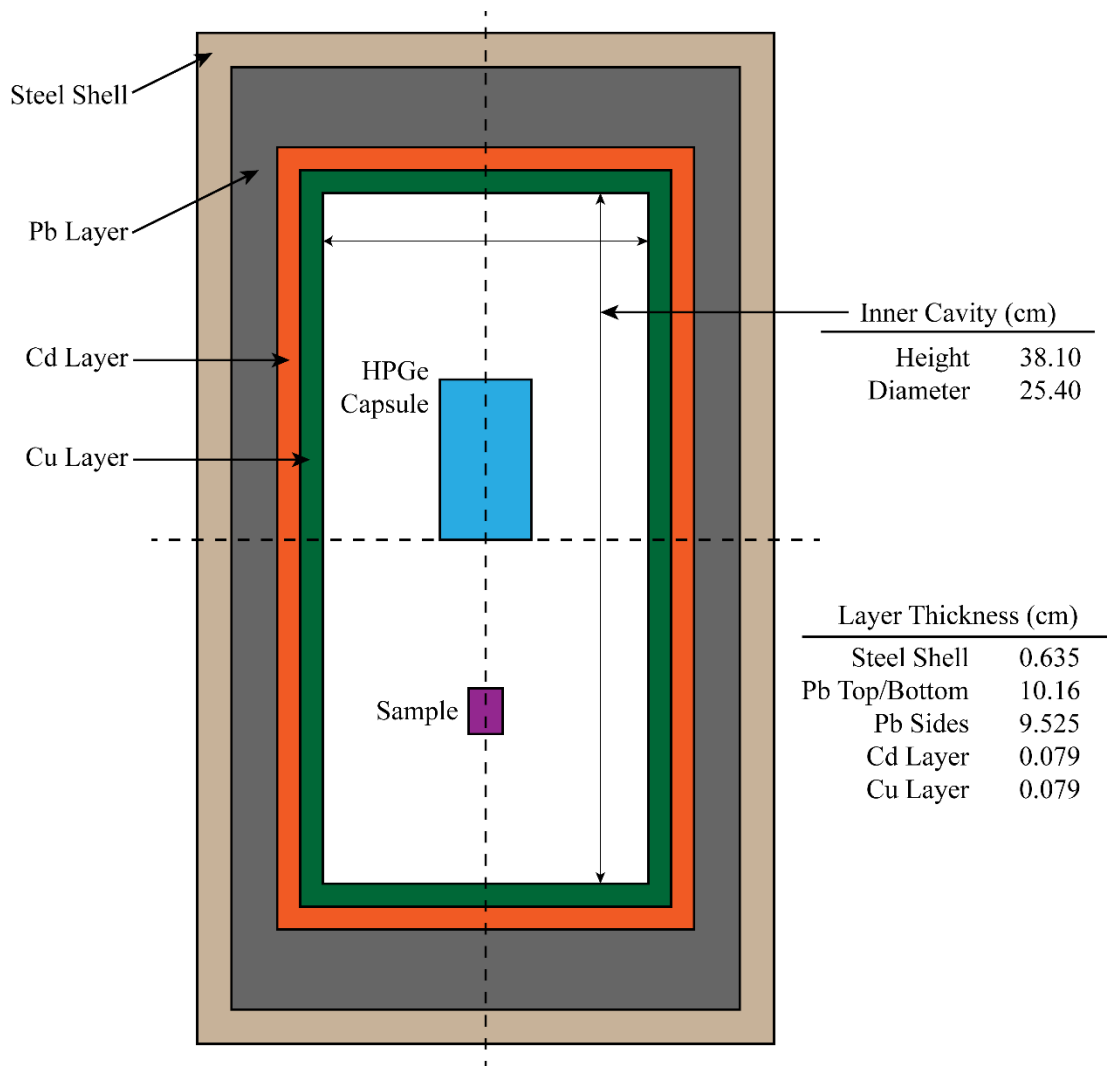


Figure B.1 Schematic representation of the shield chamber geometry for the HPGe detector simulation in MCNP, showing layer thicknesses and inner cavity dimensions, along with the relative positions of the HPGe capsule and sample.

The sample was modeled as a small cylindrical polyethylene vial to be consistent with the experiment setup. Experimental procedures called for dissolution of activated foils, so source particles originated from randomly sampled locations within the sample vial. Since experimental samples were liquid based, the simulated source assumed a density of 1 g cm^{-3} . The simulation environment around the detector and sample was defined as dry air near sea level.

Simulations ran at least 10^9 photons emitted isotropically as source particles. Both photon and electron interactions were tracked in the simulations. A lower energy cutoff of 50 keV was used for both photons and electrons to save on computation time. Interactions were sampled based on the MCPLIB84 photon library and the el03 electron library. The pulse-height spectrum was created using the F8 tally with the Gaussian energy broadening (GEB) option as a detector response function. The GEB terms were derived from experimental data using the physical detector on which the model was based. The simulated spectra were setup to record counts in 4096 channels with a 0.5 keV gain per channel, consistent with experimental counts.

The MCNP input file for the HPGe detector with the shielding chamber is:

```

HPGe Simulation
c -----
c "comment section"
c
c -----Cell Block-----
c -----XP/3 Detector cells-----
21 51 -2.70 3 -2 imp:p,e=1 $ Al endcap
22 0 4 -3 imp:p,e=1 $ Area under vacuum
23 51 -2.70 -4 5 imp:p,e=1 $ Al mounting cup
83 60 -1.380 -5 -45 imp:p,e=1 $ Mylar layer
24 52 -5.323 -46 45 -5 6 imp:p,e=1 $ Outer dead layer
84 0 -5 46 imp:p,e=1 $ Void area
25 52 -5.323 7 -6 imp:p,e=1 $ Active Ge crystal
26 52 -5.323 8 -7 imp:p,e=1 $ Inner dead layer
27 0 -8 imp:p,e=1 $ Inner crystal bore
c
c -----Shield-----
32 55 -0.001205 2 12 10 -14 imp:p,e=1 $ Air within simulation environment
33 56 -8.96 14 -15 imp:p,e=1 $ Cu shield layer
34 57 -8.65 15 -16 imp:p,e=1 $ Cd shield layer
35 58 -11.35 16 -17 imp:p,e=1 $ Pb shield layer
36 59 -7.82 17 -18 imp:p,e=1 $ Steel shield cover
c
c -----Sample and Universe cells-----
28 53 -0.93 11 -10 imp:p,e=1 $ Prindle vial base
29 53 -0.93 10 -12 imp:p,e=1 $ Prindle vial cap
30 54 -1 -11 -13 imp:p,e=1 $ Liquid sample (assumed H2O)
31 55 -0.001205 -11 13 imp:p,e=1 $ Air inside Prindle vial

```

99 0 18 imp:p,e=0 \$ Universe boundary, external face of shield

c -----
c

c -----Surface Block-----

c -----XP/3 Detector-----

2 rcc 0 0 0 0 0 13.4 3.5 \$ Outer endcap boundary
3 rcc 0 0 0.1 0 0 13.2 3.4 \$ Inner endcap boundary
4 rcc 0 0 0.4 0 0 9.4 3.03 \$ Outer mounting cup boundary
5 rcc 0 0 0.403 0 0 9.097 2.95 \$ Inner mounting cup boundary
45 pz 0.406 \$ Mylar cap
6 rcc 0 0 0.476 0 0 6.03 2.88 \$ Outer dead layer boundary
46 pz 6.506 \$ Rear crystal boundary
7 rcc 0 0 1.76597 0 0 4.74003 0.45003 \$ Inner dead layer boundary
8 rcc 0 0 1.766 0 0 4.74 0.45 \$ Crystal inner bore

c
c -----Shield-----

14 rcc 0 0 -19.05 0 0 38.10 12.7 \$ Inner cavity boundary
15 rcc 0 0 -19.1293750 0 38.25875 12.779375 \$ Cu/Cd boundary
16 rcc 0 0 -19.20875 0 0 38.4175 12.85875 \$ Cd/Pb boundary
17 rcc 0 0 -29.36875 0 0 58.7375 22.38375 \$ Pb/Steel boundary
18 rcc 0 0 -30.00375 0 0 60.0075 23.001875 \$ External shield boundary

c
c -----Sample and Universe-----

10 rcc 0 0 -11.2445 0 0 4.3 1.85 \$ Prindle base outer diameter
11 rcc 0 0 -11.0445 0 0 4.1 1.65 \$ Prindle base inner diameter
12 rcc 0 0 -8.0445 0 0 1.3 2.25 \$ Prindle cap outer boundary
13 pz -9.8755 \$ Sample volume boundary

c
c Surface 10-13 are based on the distance from the detector to the source
c center of mass (DSCM) in cm. 10: DSCM + 0.7845; 11: DSCM + 0.5845;
c 12: DSCM - 2.4155; 13: DSCM - 0.5845

c -----
c

c -----Data Block-----

c -----Materials-----From PNNL Compendium-----

m0 plib=84p elib=03e \$ Electron and photon libraries
m51 13000 1 \$ Natural Al
m52 32000 1 \$ Natural Ge
m53 1000 -0.143716 6000 -0.856284 \$ Polyethylene
m54 1000 -0.111894 8000 -0.888106 \$ Sample solvent - assumed to be H2O
m55 6000 -0.000124 \$ Air - C, N, O, and Ar, dry at sea level
7000 -0.755268
8000 -0.231781
18000 -0.012827
m56 29000 1 \$ Natural Cu lining of shield
m57 48000 1 \$ Natural Cd lining of shield
m58 82000 1 \$ Natural Pb of shield
m59 6000 -0.005 26000 -0.995 \$ Carbon steel (mat.294, PNNL)
m60 1000 -0.041960 \$ Mylar (PET-mat.246, PNNL)

```

6000 -0.625016
8000 -0.333024
c
c -----Physics & Options-----
mode p e $ photon transport problem
prdmp 2j 1 3 $ creates mctal file, saves last 3 dumps
print -85 -86 -30 $ table printing
cut:p,e j 0.05 $ 50 keV cutoff
c
c -----Source Definition-----
nps 1e9
sdef cel=30 erg=d3 rad=d1 ext=d2 axs=0 0 1 pos= 0 0 -11.0445 par=p
c --Have to change POS to match sample location---POS=location of cell 11----
si1 0 1.65 $ radial extent of the prindle
si2 0 1.169 $ linear extent of the prindle
# si3 sp3 $ source line energies and probabilities
c
c -----Tally-----
fc108 Simulated HPGe Spectrum
f108:p 25 $ pulse-height tally for HPGe cell
ft108 geb 4.93076e-4 9.39315e-4 0.07615 $ Energy broadening terms
e108 0 4095i 2.048 $ energy bins, 4096 channels
c -----

```

The ORTEC specification sheet giving detector capsule component dimensions is shown in Fig. B.2.

QUALITY ASSURANCE DATA SHEET

**GEM Series HPGe (High-Purity Germanium) Coaxial Detector System
Model and Serial Numbers**

Detector Model No.	GEM30P4-70	Ship Date	28-Apr-09
Cryostat Configuration	CFG-PD4-13	Serial No.	49-TP22638A
Dewar Model	Dewar with Cryostat	When calling Customer Service, always reference the Detector Serial No.	
Preamplifier Model	A257P	Sales Order No.	10000088
Preamplifier Serial No.	9035032		
H. V. Filter Model	138EMI		
H. V. Filter Serial No.	9079111		
SMART-1-P Serial No.			

Cryogenic Information

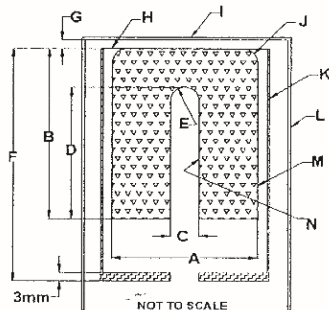
Dewar Capacity	13 liters	Static Holding Time	n/a
Detector Cool-Down Time	n/a		

High Voltage Bias

Recommended Operating Bias POSITIVE 2400 Volts

Performance Specifications*

	<u>Warranted</u>	<u>Measured</u>	<u>Amp Shape Time</u>
Resolution (FWHM) at 1.33 MeV, ⁶⁰ Co	1.85 keV	1.73 keV	6 μs
Peak-to-Compton Ratio, ⁶⁰ Co	60:1	70:1	6 μs
Relative Efficiency at 1.33 MeV, ⁶⁰ Co	30 %	37 %	6 μs
Peak Shape (FWTM/FWHM), ⁶⁰ Co	1.9	1.8	6 μs
*Peak Shape (FWFM/FWHM), ⁶⁰ Co	2.6	2.5	6 μs
* FWFM/FWHM is typical not warranted			
Resolution (FWHM) at 122 KeV, ⁵⁷ Co	850 eV	700 eV	6 μs



E: NOMINAL 5-mm RADIUS

F: 94-mm CUP LENGTH

G: 3-mm SPACE

H: 0.03-mm/0.03-mm Al/Mylar

I: 1-mm Al

J: NOMINAL 8-mm RADIUS

K: 0.8-mm Al

L: 1-mm Al

M: 0.7-mm Ge/Li DEAD LAYER

N: 0.3-micron Ge/B DEAD LAYER

A= 59 mm
Crystal Diameter

B= 61 mm
Crystal Length

C= 9 mm
Hole Diameter

D= 47.4 mm
Hole Depth

OTHER Capsule: SCA # 9026

Cryo: PD4-13 #12584

Data Certified By: *Thomas Jennings*

DATE 4-28-09

Form no. 0308BK vers. 1

Figure B.2 The ORTEC specification sheet for the physical detector used to build to the MCNP detector model.

B.2 The d+Be Neutron Converter

Neutron production for the d+Be converter was modeled after the setup at the University of California-Davis campus Crocker Nuclear Laboratory. The experimental deuteron source was a 30 MeV beam operating at 10 μ A supplied by a 76-inch cyclotron. The deuteron beam is centered on the Be converter cylinder. The cylinder is housed in a Cu jacket to facilitate cooling. The foil holder was modeled as mica rectangle with a hole in the center for target foils. The shape of the experimental target holder is slightly different but was idealized for simplicity in the MCNP model. A 3D representation of the irradiation setup is shown in Fig. B.3. The Be cylinder was 2.54 cm long with a 1.27 cm diameter. The Cu jacket surrounded the Be cylinder and was 20 μ m thick. The target frame was approximately 5.08 cm wide and 3.71 cm high with a thickness of 0.80 cm. The frame cutout was centered, with a diameter of 1.91 cm. The target foil modeled in Fig. B.3 has a diameter of 1.27 cm and a thickness of 0.254 cm.

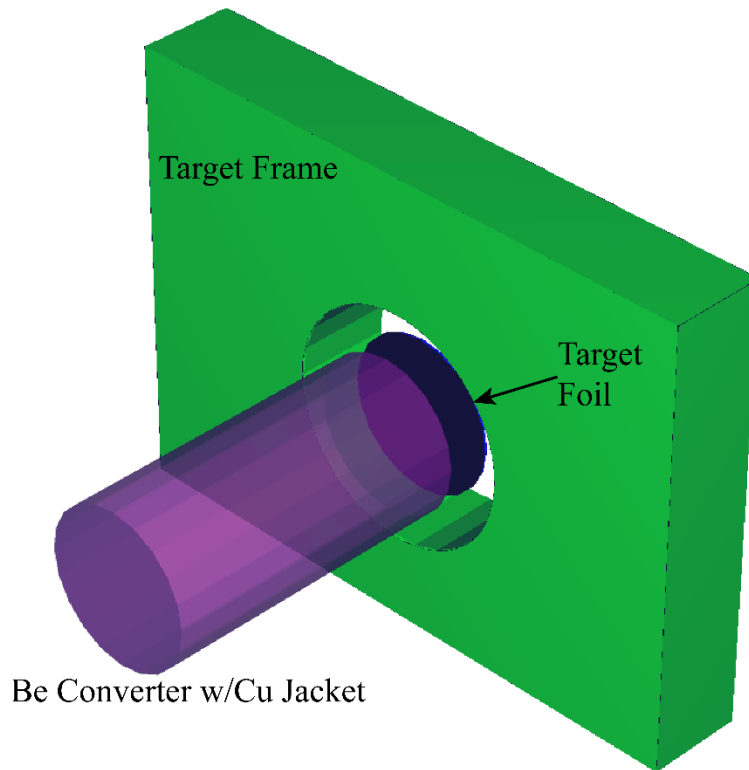


Figure B.3 Simulation geometry in MCNP for the d+Be neutron converter at the University of California-Davis campus.

The source was defined as 30 MeV monodirectional deuterons aimed at the center of the converter cylinder end. The simulation ran 2×10^9 source particles in order to pass all statistical checks for the neutron energy tally. The ENDF/B-VII.1 library data was used when available and was supplemented by the CEM03.03 and LAQGSM03.03 physics models. Neutrons were tallied in 1000 equal unit lethargy energy bins from 1×10^{-11} MeV up to 100 MeV using the F4 tally.

The MCNP input file for neutron production from the d+Be converter is:

```
UC Davis Neutron Production Simulation
c -----
c using pencil beam deuteron source
c
c -----Cell Block-----
```

```

32 2 -1.848 -11          $ Be converter
33 3 -8.96  11 -12      $ Cu jacket
34 4 -2.82  -13 14      $ Mica target frame w/cutout
35 0      -15          $ Target foil
36 5 -0.001205 -19 #32 #33 #34 #35 $ Air
99 0      19          $ Outside simulation universe

```

```

c -----
c

```

```

c -----Surface Block-----

```

```

11 rcc 0 0 0 -2.54 0 0 0.635 $ Be converter cylinder
12 rcc 0.002 0 0 -2.544 0 0 0.637 $ Cu jacket cover
13 rpp 0.1 0.89502 -2.54 2.54 -1.64338 2.06502 $ Frame
14 rcc 0.1 0 0 0.79502 0 0 0.9525 $ Frame cutout
15 rcc 0.33876 0 0 0.02 0 0 0.635 $ Target foil
19 sph 0 0 0 5 $ Simulation environment boundary

```

```

c -----
c

```

```

c -----Data Block-----

```

```

c -----Materials-----

```

```

m0 nlib=80c hlib=70h $ Data Library specification: ENDF/B-VII.1
m2 4009 1 $ Be converter
mt2 be.20t $ Treatment option for thermal neutrons in Be
m3 29063 69.15 29065 30.85 $ Cu converter jacket
m4 1001 8.69465E-02 $ Mica as muscovite - webmineral.com
    1002 1.00000E-05
    8016 5.20471E-01
    8017 1.98261E-04
    8018 1.06957E-03
    9019 8.69565E-02
    13027 1.30435E-01
    14028 4.00970E-02
    14029 2.03696E-03
    14030 1.34435E-03
    19039 1.21641E-01
    19040 1.52609E-05
    19041 8.77852E-03
m5 6012 1.48395E-04 $ Air - dry, near sea level, PNNL mat #4
    6013 1.60500E-06
    7014 7.81576E-01
    7015 2.85533E-03
    8016 2.10236E-01
    8017 8.00842E-05
    8018 4.32033E-04
    18036 1.55825E-05
    18038 2.93806E-06
    18040 4.65248E-03

```

```

c
c -----Physics & Options-----

```

```

mode n d h t s a # $ Specify neutrons all particles

```

```

imp:n,d,h,t,s,a,# 1 1 1 1 1 0 $ Cell importances
prdmf 2j 1 3 $ Creates mctal files, saves last 3 dumps
print -85 -86 -30 $ Table printing options
lca 8j 1 1 $ CEM03.03 & LAQGSM03.03
phys:n j 200 $ Use analog neutron capture
cut:n 2j 0 0 $ Use analog neutron capture
rand gen=2 $ Random number generator #2
c
c ----Source Definition-----
nps 2e9 $ Number of source particles
sdef pos=-3 0 0 erg=30 vec=1 0 0 par=d dir=1 $ Pencil beam
c
c ----Tally-----
fc354 log binning
f354:n 35
e354 1e-11 1000log 100
c -----

```

B.3 *The Flattop Critical Assembly*

The Flattop critical assembly is a spherical natural uranium reflector with interchangeable cores and mass buttons for changing reactivity and achieving different neutron spectra. The configuration used in this work employed a highly enriched uranium core. The assembly has a horizontal sample bore through the center of the core and reflector to allow for irradiations at different locations. The neutron spectrum used in this work was obtained from a detailed model in MCNP created by collaborators at Los Alamos National Laboratory. Due to the sensitive nature of the assembly, exact dimensions were not available. A representative description was taken from the International Handbook of Evaluated Criticality Safety Benchmark Experiments for this Flattop configuration. The input file for the representative Flattop critical assembly model in MCNP is:

Flattop Spectrum Determination

```
C -----
c "comment section"
c
c -----Cell Block-----
11 101 0.04767449 -1 imp:n=1      $ HEU core
12 102 0.048069744 1 -2 imp:n=1  $ nat U reflector
13 0 2 imp:n=0                    $ outside assembly
c -----
c

c -----Surface Block-----
1 so 6.1156  $ core
2 so 24.1242 $ reflector
c -----
c

c -----Data Block-----
c ----Materials-----
m101 92234.80c 0.00048869      $ HEU core
      92235.80c 0.044482
      92238.80c 0.0027038
m102 92234.80c 0.0000026438   $ nat U reflector
      92235.80c 0.0003461
      92238.80c 0.047721
c
c ----Physics, Options, & SDEF-----
mode n
totnu
rand gen=2 seed=100000001
kcode 1200000 1.0 50 2050
prtmp j 500
sdef rad=d1 erg=d2
si1 0. 24.1242
sp1 -21 2
sp2 -3 0.988 2.249
print
c
c ----Tally-----
fc5 Point Detector Tally at Origin
f5:n 0 0 0 0.01
e5 1e-11 1000log 100
c -----
c -----
```

B.4 Activation Calculations with FISPACT-II

Activation calculations were performed using the FISPACT-II code with the ENDF/B-VII.1, JEFF-3.2, and TENDL-14 nuclear data libraries. Initial neutron spectra derived from the flux tallies in the models of each neutron source were converted to the 709-group structure in FISPACT-II using the GRPCONVERT keyword. Activation reaction libraries were then pre-compiled for each nuclear data based on the 709-group neutron distributions. The group conversion, library building, and activation calculations can be run from a single input file but were separated for this work for verification after each step. The group conversion input is:

```
<< convert flux to 709 group structure>>
CLOBBER
GRPCONVERT 1001 709
FISPACT
* Convert UCD log-binned flux to 709 group structure
END
* END
```

The input file for compiling the reaction libraries is:

```
<< --FISPACT input file to process library data for UCD 709-group flux irradiation-- >>
<< -----first block is library prep block----- >>
CLOBBER                << overwrite if existing filename >>
LOGLEVEL 4             << error reporting information >>
GETXS 1 709            << get XS data for 709 group structure linked in "files" >>
GETDECAY 1             << get decay data from link in "files" >>
NOFISS                 << don't process fission yield data, ok since no actinides >>
FISPACT
* Library Prep for UCD Irradiation w/JEFF-3.2 data << title card >>
PRINTLIB 0             << gives full library description output >>
END
* End of Library Prep Run for UCD spectrum
<< have to use ALL CAPS for keywords >>
```

The input file for the activation calculations is:

```
<< Input file to run UCD activation calculations w/JEFF-3.2 data on SS-304 >>
<< library prep block >>
MONITOR 1      << update display while running >>
CLOBBER       << file overwrite >>
GETXS 0       << read XS from collapx file >>
GETDECAY 0    << read decay from arrayx file >>
LOGLEVEL 4    << error level printing >>
FISPACT
* UCD Activation of SS-304 w/JEFF-3.2 data
<< Initial Conditions and Print Options section >>
TAB1 1        << output # of atoms and grams of each nuclide in separate table >>
TAB2 2        << output activity and dose rate of each nuclide in separate table >>
DENSITY 7.93  << g/cm^3 >>
MASS 1.518e-4 5 << mass of material in kg and # of elements in material >>
Fe 71.21      << wt% of each component >>
Ni 8.05
Cu 0.54
Mn 1.81
Cr 18.39
MIND 1000     << output threshold level, print nuclides over 1k atoms >>
UNCERTAINTY 2 << uncertainty for inventory and pathways, retain other defaults>>
UNCTYPE 3     << include half-life and XS uncertainties in final values >>
TOLERANCE 0 1e-5 1e-9 << set solver convergence tolerance limits >>
NOSTABLE      << do not include stable nuclides in output >>
SORTDOMINANT 150 150 << display the top 100 nuclides, sorted >>
<< Irradiation Phase >>
FLUX 1.1691E+12 << flux value in n/cm^2-s >>
ATOMS         << calculate inventory at this step >>
TIME 7.0 HOURS << irradiation time and units, can do multiple steps if desired >>
ATOMS         << calculate inventory at this step >>
<< Cooling Phase - need at least 1 cooling step >>
FLUX 0        << set flux to 0 before cooling, signals end of irradiation >>
ZERO          << terminates irradiation phase >>
END
* End of P3 UCD Activation w/JEFF-3.2 data
```

Appendix C: The Random Walk of MCNP

The Monte Carlo N-Particle radiation transport code (MCNP) is a general purpose stochastic computational code used to simulate various particle interactions in a variety of situations [84]. As a stochastic code, MCNP uses random numbers to sample interactions throughout a particle's history for a given problem geometry. The result is a statistical approximation of the average behavior of an observable for the defined problem.

Simulation with MCNP involves tracking the individual interaction history of a particle through a defined geometry, where probabilities of collisions and other interactions are statistically sampled from available data and probability distributions using random numbers. This process is then repeated many, many times to arrive at an average value. A particle's history ends with an event such as absorption or escape from the problem geometry. All subsequent particles produced during the lifetime of the original particle may also be tracked.

Consider a photon interacting with an absorbing material. The total interaction probability at any given instance is the sum of all possible interactions, which include photoelectric absorption, Compton scattering, and pair production. Each possible interaction has a defined probability based on the energy of the photon and the available nuclear data. At each collision or interaction point, the specific interaction that takes place is sampled from the total interaction probability using random numbers. One photon may undergo several Compton scattering events before exiting the material. Another photon may experience a different number of Compton scattering

events before photoelectric absorption occurs and terminates the life of the photon. If a Compton scattering event is randomly selected, the scattering angle (θ) is also randomly sampled, thereby determining the scattered photon energy and direction for the next step of the photon's history.

For problems with multiple materials defined in the geometry, the process of relying on random interactions is continued as the photon interacts with different each material. The life of the photon is terminated only when an absorption event occurs or when the photon exits the defined problem geometry. The random walk process is repeated over and over again to obtain satisfactory statistical results.

List of References

1. International Atomic Energy Agency (2016) IAEA Incident and Trafficking Database 2016 Fact Sheet. <https://www-ns.iaea.org/downloads/security/itdb-fact-sheet.pdf>. Accessed 27 Nov 2017
2. Global Initiative to Combat Nuclear Terrorism Brochure. <http://www.gicnt.org/documents/GICNT-Brochure-v2-WebReady.pdf>. Accessed 12 Mar 2017
3. Nuclear Forensics International Technical Working Group. <http://www.nf-itwg.org/>. Accessed 30 Nov 2017
4. Zubarev J, Tittmore G (2004) The Global Threat Reduction Initiative: Enhancing Radiological Security in the Russian Federation. https://www.iaea.org/OurWork/ST/NE/NEFW/CEG/documents/ws052007_15E.pdf. Accessed 1 Dec 2017
5. (2003) Proliferation Security Initiative. <https://www.state.gov/t/isn/c10390.htm>. Accessed 3 Dec 2017
6. Moody KJ, Grant PM, Hutcheon ID (2015) Nuclear Forensic Analysis, 2nd ed. CRC Press Taylor and Francis Group, LLC, Boca Raton, Florida
7. International Atomic Energy Agency (2015) Nuclear Forensics in Support of Investigations. IAEA Nucl Secur Ser 2–G:1–80.
8. Kristo MJ, Tumey SJ (2013) The state of nuclear forensics. Nucl Instruments Methods Phys Res Sect B Beam Interact with Mater Atoms 294:656–661. doi: 10.1016/j.nimb.2012.07.047
9. Keegan E, Kristo MJ, Toole K, et al (2016) Nuclear Forensics: Scientific Analysis Supporting Law Enforcement and Nuclear Security Investigations. Anal Chem 88:1496–1505. doi: 10.1021/acs.analchem.5b02915
10. Nuclear Regulatory Legislation 112th Congress: 2nd Session. NUREG-0980; Vol. 1, No. 10. <https://www.nrc.gov/docs/ML1327/ML13274A489.pdf>. Accessed 29 Nov 2017
11. International Atomic Energy Agency (1956) STATUTE. <https://www.iaea.org/about/statute>. Accessed 25 Nov 2017
12. Pellaud B (2002) Proliferation aspects of plutonium recycling. Comptes Rendus Phys 3:1067–1079. doi: 10.1016/S1631-0705(02)01364-6
13. Mayer K, Wallenius M, Varga Z (2013) Nuclear forensic science: Correlating measurable material parameters to the history of nuclear material. Chem Rev 113:884–900. doi: 10.1021/cr300273f
14. Schwantes JM, Marsden O, Pellegrini KL (2017) State of practice and emerging application of analytical techniques of nuclear forensic analysis:

highlights from the 4th Collaborative Materials Exercise of the Nuclear Forensics International Technical Working Group (ITWG). *J Radioanal Nucl Chem* 311:1441–1452. doi: 10.1007/s10967-016-5037-5

15. (1953) Atoms for Peace. https://www.eisenhower.archives.gov/research/online_documents/atoms_for_peace.html. Accessed 3 Dec 2017
16. (1968) Treaty on the Non-Proliferation of Nuclear Weapons. <https://www.un.org/disarmament/wmd/nuclear/npt/text>. Accessed 29 Nov 2017
17. (1991) Strategic Arms Reduction Treaty (START I). <https://fas.org/nuke/control/start2/index.html>. Accessed 3 Dec 2017
18. (1993) Strategic Arms Reduction Treaty (START II). <https://fas.org/nuke/control/start2/index.html>. Accessed 3 Dec 2017
19. (1996) Comprehensive Nuclear-Test-Ban Treaty. http://ctbto.org/fileadmin/content/treaty/treaty_text.pdf. Accessed 28 Nov 2017
20. Woolf AF (2017) The New START Treaty: Central Limits and Key Provisions. <https://fas.org/sgp/crs/nuke/R41219.pdf>. Accessed 2 Dec 2017
21. Nuclear-Weapon-Free Zones. <https://www.un.org/disarmament/wmd/nuclear/nwzf/>. Accessed 3 Dec 2017
22. Stages of the Nuclear Fuel Cycle. <https://www.nrc.gov/materials/fuel-cycle-fac/stages-fuel-cycle.html>. Accessed 29 Nov 2017
23. Robel M, Kristo MJ (2008) Discrimination of source reactor type by multivariate statistical analysis of uranium and plutonium isotopic concentrations in unknown irradiated nuclear fuel material. *J Environ Radioact* 99:1789–1797. doi: 10.1016/j.jenvrad.2008.07.004
24. Alamelu D, Aggarwal SK (2011) Application of chemometry for identification of the source of plutonium. *Int J Nucl Energy Sci Technol* 6:30–36. doi: 10.1504/IJNEST.2011.039245
25. Nicolaou G (2008) Provenance of unknown plutonium material. *J Environ Radioact* 99:1708–1710. doi: 10.1016/j.jenvrad.2008.06.001
26. Nygren U, Ramebäck H, Nilsson C (2007) Age determination of plutonium using inductively coupled plasma mass spectrometry. *J Radioanal Nucl Chem* 272:45–51. doi: 10.1007/s10967-006-6780-9
27. Ramebäck H, Nygren U, Lagerkvist P, et al (2008) Basic characterization of ²³³U: Determination of age and ²³²U content using sector field ICP-MS, gamma spectrometry and alpha spectrometry. *Nucl Instruments Methods Phys Res Sect B Beam Interact with Mater Atoms* 266:807–812. doi: 10.1016/j.nimb.2008.01.008
28. Wallenius M, Mayer K (2000) Age determination of plutonium material in

- nuclear forensics by thermal ionisation mass spectrometry. *Fresenius J Anal Chem* 366:234–238. doi: 10.1007/s002160050046
29. Richter S, Alonso A, De Bolle W, et al (1999) Isotopic “fingerprints” for natural uranium ore samples. *Int J Mass Spectrom* 193:9–14. doi: 10.1016/S1387-3806(99)00102-5
 30. Srncik M, Mayer K, Hrnccek E, et al (2011) Investigation of the $^{236}\text{U}/^{238}\text{U}$ isotope abundance ratio in uranium ores and yellow cake samples. *Radiochim Acta* 99:335–339. doi: 10.1524/ract.2011.1840
 31. Permana S, Suzuki M, Su’ud Z (2012) Comparative analysis of LWR and FBR spent fuels for nuclear forensics evaluation. *AIP Conf Proc* 1448:142–152. doi: 10.1063/1.4725449
 32. Joe K, Jeon YS, Song BC, et al (2010) Isotope correlations for determining the isotopic composition of plutonium in high burnup pressurized water reactor (PWR) samples. *Appl Radiat Isot* 68:505–510. doi: 10.1016/j.apradiso.2009.10.055
 33. Wallenius M, Lützenkirchen K, Mayer K, et al (2007) Nuclear forensic investigations with a focus on plutonium. *J Alloys Compd* 444–445:57–62. doi: 10.1016/j.jallcom.2006.10.161
 34. Keegan E, Richter S, Kelly I, et al (2008) The provenance of Australian uranium ore concentrates by elemental and isotopic analysis. *Appl Geochemistry* 23:765–777. doi: 10.1016/j.apgeochem.2007.12.004
 35. Keegan E, Kristo MJ, Colella M, et al (2014) Nuclear forensic analysis of an unknown uranium ore concentrate sample seized in a criminal investigation in Australia. *Forensic Sci Int* 240:111–121. doi: 10.1016/j.forsciint.2014.04.004
 36. Badaut V, Wallenius M, Mayer K (2009) Anion analysis in uranium ore concentrates by ion chromatography. *J Radioanal Nucl Chem* 280:57–61. doi: 10.1007/s10967-008-7404-3
 37. Varga Z, Krajčo J, Peňkin M, et al (2017) Identification of uranium signatures relevant for nuclear safeguards and forensics. *J Radioanal Nucl Chem* 312:639–654. doi: 10.1007/s10967-017-5247-5
 38. Manna S, Roy SB, Joshi JB (2012) Study of crystallization and morphology of ammonium diuranate and uranium oxide. *J Nucl Mater* 424:94–100. doi: 10.1016/j.jnucmat.2012.02.012
 39. Wallenius M, Mayer K, Ray I (2006) Nuclear forensic investigations: Two case studies. *Forensic Sci Int* 156:55–62. doi: 10.1016/j.forsciint.2004.12.029
 40. Keith C, Selby H, Lee A, et al (2018) Activation Product Interpretation of Structural Material for Fast Critical Assemblies. Submitt. to *Ann. Nucl. Energy* (under rev):
 41. Sharp N, Ticknor BW, Bronikowski M, et al (2017) Nd and Sm isotopic

- composition of spent nuclear fuels from three material test reactors. *J Radioanal Nucl Chem* 311:801–808. doi: 10.1007/s10967-016-5099-4
42. The Stainless Steel Family. <http://www.worldstainless.org/Files/issf/non-image-files/PDF/TheStainlessSteelFamily.pdf>. Accessed 12 Nov 2017
 43. Goodell JJ, Egnatuk CM, Padgett SW, et al (2017) Validation of a Monte Carlo HPGe detector model against irradiated foil gamma-ray spectroscopy measurements. *J Radioanal Nucl Chem* 314:1793–1802. doi: 10.1007/s10967-017-5579-1
 44. Goodell JJ, Egnatuk CM, Padgett SW, et al (2018) Comparison of Irradiated Foil Measurements with Activation Calculations and HPGe Simulations. *J Radioanal Nucl Chem*. doi: 10.1007/s10967-018-5820-6
 45. Dunlap RA (2004) *An Introduction to the Physics of Nuclei and Particles*. Brooks/Cole, Belmont, California
 46. Lilley J (2001) *Nuclear Physics Principles and Applications*. John Wiley & Sons, Chichester, West Sussex
 47. Bateman H (1910) The solution of a system of differential equations occurring in the theory of radioactive transformations. *Proc Cambridge Philos Soc Math Phys Sci* 15:423–427.
 48. Bajoga AD, Alazemi N, Regan PH, Bradley DA (2015) Radioactive investigation of NORM samples from Southern Kuwait soil using high-resolution gamma-ray spectroscopy. *Radiat Phys Chem* 116:305–311. doi: 10.1016/j.radphyschem.2015.01.041
 49. Guguła S, Kozak K, Mazur J, et al (2017) Fast in situ gamma spectroscopy using hand-held spectrometer with NaI probe. *J Environ Radioact*. doi: 10.1016/j.jenvrad.2017.09.018
 50. Baldoncini M, Albéri M, Bottardi C, et al (2017) Exploring atmospheric radon with airborne gamma-ray spectroscopy. *Atmos Environ* 170:259–268. doi: 10.1016/j.atmosenv.2017.09.048
 51. Ene A, Badica T, Olariu A, et al (2001) Coincidence method for the analysis of minor elements in steel by deuteron-induced prompt γ -ray spectrometry (d-PIGE). *Nucl Instruments Methods Phys Res Sect B Beam Interact with Mater Atoms* 179:126–132. doi: 10.1016/S0168-583X(01)00441-4
 52. Graham J, Landsberger S, Ferreira PJ, et al (2012) Neutron flux characterization techniques for radiation effects studies. *J Radioanal Nucl Chem* 291:503–507. doi: 10.1007/s10967-011-1270-0
 53. Stefanik M, Bem P, Majerle M, et al (2017) Neutron spectrum determination of d(20)+Be source reaction by the dosimetry foils method. *Radiat Phys Chem* 140:466–470. doi: 10.1016/j.radphyschem.2017.03.029
 54. Schulc M, Baroň P, Novák E, et al (2016) Measurement of reaction rates for

- different neutron induced reactions in ^{27}Al . *Appl Radiat Isot* 118:277–280. doi: 10.1016/j.apradiso.2016.10.001
55. Weisshaar D, Bazin D, Bender PC, et al (2017) The performance of the γ -ray tracking array GRETINA for γ -ray spectroscopy with fast beams of rare isotopes. *Nucl Instruments Methods Phys Res Sect A Accel Spectrometers, Detect Assoc Equip* 847:187–198. doi: 10.1016/j.nima.2016.12.001
 56. Bucurescu D, Căta-Danil I, Ciocan G, et al (2016) The ROSPHERE γ -ray spectroscopy array. *Nucl Instruments Methods Phys Res Sect A Accel Spectrometers, Detect Assoc Equip* 837:1–10. doi: 10.1016/j.nima.2016.08.052
 57. Browne E, Tuli JK (2013) Nuclear data sheets for $A = 60$. *Nucl Data Sheets* 114:1849–2022. doi: 10.1016/j.nds.2013.11.002
 58. Knoll GF (2010) *Radiation Detection and Measurement*, 4th ed. John Wiley & Sons, Hoboken, New Jersey
 59. Gilmore GR (2008) *Practical Gamma-Ray Spectrometry*, 2nd ed. John Wiley & Sons, Chichester, West Sussex
 60. Nicolini R, Camera F, Blasi N, et al (2007) Investigation of the properties of a $1'' \times 1''$ LaBr₃:Ce scintillator. *Nucl Instruments Methods Phys Res Sect A Accel Spectrometers, Detect Assoc Equip* 582:554–561. doi: 10.1016/j.nima.2007.08.221
 61. Drescher A, Yoho M, Landsberger S, et al (2017) Gamma-gamma coincidence performance of LaBr₃:Ce scintillation detectors vs HPGe detectors in high count-rate scenarios. *Appl Radiat Isot* 122:116–120. doi: 10.1016/j.apradiso.2017.01.012
 62. Han D, Kim W, Lee S, et al (2018) Assessment of gamma radiation shielding properties of concrete containers containing recycled coarse aggregates. *Constr Build Mater* 163:122–138. doi: 10.1016/j.conbuildmat.2017.12.078
 63. Kurudirek M (2017) Heavy metal borate glasses: Potential use for radiation shielding. *J Alloys Compd* 727:1227–1236. doi: 10.1016/j.jallcom.2017.08.237
 64. Stark K, Gómez-Ros JM, Vives i Batlle J, et al (2017) Dose assessment in environmental radiological protection: State of the art and perspectives. *J Environ Radioact* 175–176:105–114. doi: 10.1016/j.jenvrad.2017.05.001
 65. Duc Tam H, Hai Yen NT, Tran LB, et al (2017) Optimization of the Monte Carlo simulation model of NaI(Tl) detector by Geant4 code. *Appl Radiat Isot* 130:75–79. doi: 10.1016/j.apradiso.2017.09.020
 66. Garcia AR, Mendoza E, Cano-Ott D, et al (2017) New physics model in GEANT4 for the simulation of neutron interactions with organic scintillation detectors. *Nucl Instruments Methods Phys Res Sect A Accel Spectrometers, Detect Assoc Equip* 868:73–81. doi: 10.1016/j.nima.2017.06.021
 67. Laramore D, Pfeifer MP, Lindstrom J, Bindra H (2018) Design and criticality

- analysis of colloidal slurry nuclear reactors. *Ann Nucl Energy* 111:255–261. doi: 10.1016/j.anucene.2017.09.005
68. Pohorecki W, Jodłowski P, Pytel K, Prokopowicz R (2017) Long-lived radionuclide activity formed in ITER construction steels in 6 Li-D converter neutron field. *Fusion Eng Des* 124:1042–1045. doi: 10.1016/j.fusengdes.2017.04.034
 69. Ródenas J (2017) Application of the Monte Carlo method to estimate doses due to neutron activation of different materials in a nuclear reactor. *Radiat Phys Chem* 140:442–446. doi: 10.1016/j.radphyschem.2017.02.015
 70. Zwermann W, Aures A, Gallner L, et al (2014) Nuclear data uncertainty and sensitivity analysis with XSUSA for fuel assembly depletion calculations. *Nucl Eng Technol* 46:343–352. doi: 10.5516/NET.01.2014.711
 71. Herman M, Trkov A, Brown DA (2018) ENDF-6 Formats Manual. BNL-90365-2009, Brookhaven National Laboratory
 72. Chadwick MB, Herman M, Obložinský P, et al (2011) ENDF/B-VII.1 nuclear data for science and technology: Cross sections, covariances, fission product yields and decay data. *Nucl Data Sheets* 112:2887–2996. doi: 10.1016/j.nds.2011.11.002
 73. Nuclear Energy Agency (2014) JEFF-3.2 evaluated data library. http://www.oecd-nea.org/dbforms/data/eva/evatapex/jeff_32/.
 74. Shibata K, Iwamoto O, Nakagawa T, et al (2011) JENDL-4.0: A new library for nuclear science and engineering. *J Nucl Sci Technol* 48:1–30. doi: 10.1080/18811248.2011.9711675
 75. Koning AJ, Rochman D, Kopecky J, et al (2015) TENDL-2015: TALYS-based evaluated nuclear data library. https://tendl.web.psi.ch/tendl_2015/tendl2015.html.
 76. Koning AJ, Rochman D (2012) Modern Nuclear Data Evaluation with the TALYS Code System. *Nucl Data Sheets* 113:2927–2934. doi: 10.1016/j.nds.2012.11.002
 77. Kondev FG, Thoennessen M, Batchelder J, et al (2017) White Paper on Nuclear Data Needs and Capabilities for Basic Science. Nuclear Data Program, U.S. Department of Energy Office of Science
 78. TENDL-2015 Neutron sub-library for Ni: Automatic plotting comparison between libraries, TALYS, and EXFOR. https://tendl.web.psi.ch/tendl_2015/neutron_html//plots/n-Ni.pdf. Accessed 23 Jan 2018
 79. Pritychenko B, Sonzogni A Q-value Calculator (QCalc). <http://www.nndc.bnl.gov/qcalc/>.
 80. (2010) Chart of the Nuclides. <http://www.nndc.bnl.gov/chart/>.

81. Nuclear Energy Agency (2016) International Handbook of Evaluated Criticality Safety Benchmark Experiments.
82. Brewer RW, McLaughlin TP, Dean V (2016) Uranium-235 Sphere Reflected by Normal Uranium using Flattop. Int Handb Eval Crit Saf Benchmark Exp HEU-MET-FAST-028.
83. Wei Z, Yan Y, Yao ZE, et al (2013) Evaluation of the neutron energy spectrum, angular distribution, and yield of the $^9\text{Be}(d,n)$ reaction with a thick beryllium target. Phys Rev C - Nucl Phys. doi: 10.1103/PhysRevC.87.054605
84. Goorley T, James M, Booth T, et al (2012) Initial MCNP6 Release Overview. Nucl Technol 180:298–315. doi: 10.13182/NT11-135
85. Agostinelli S, Allison J, Amako K, et al (2003) GEANT4 - A simulation toolkit. Nucl Instruments Methods Phys Res Sect A Accel Spectrometers, Detect Assoc Equip 506:250–303. doi: 10.1016/S0168-9002(03)01368-8
86. Sublet J-CC, Eastwood JW, Morgan JG, et al (2015) FISPACT-II User Manual. In: Tech. Rep. UKAEA-R(11)11 Issue 7. <http://fispact.ukaea.uk/>.
87. Rearden BT, Jessee MA (2017) SCALE Code System 6.2.2. Oak Ridge Natl Lab. doi: 10.2172/1408010
88. Hitch S, Keyser R, Smalling J, Twomey T (2009) White Paper: Why High-Purity Germanium (HPGe) Radiation Detection Technology is Superior to Other Detector Technologies for Isotope Identification. ORTEC Online 1–5.
89. Szentmiklósi L, Belgya T, Maróti B, Kis Z (2014) Characterization of HPGe gamma spectrometers by geant4 Monte Carlo simulations. J Radioanal Nucl Chem 300:553–558. doi: 10.1007/s10967-014-2976-6
90. Boson J, Ågren G, Johansson L (2008) A detailed investigation of HPGe detector response for improved Monte Carlo efficiency calculations. Nucl Instruments Methods Phys Res Sect A Accel Spectrometers, Detect Assoc Equip 587:304–314. doi: 10.1016/j.nima.2008.01.062
91. Şahin D, Ünlü K (2009) Modeling a gamma spectroscopy system and predicting spectra with Geant-4. In: J. Radioanal. Nucl. Chem. pp 167–172
92. Britton R, Burnett J, Davies A, Regan PH (2013) Determining the efficiency of a broad-energy HPGe detector using Monte Carlo simulations. J Radioanal Nucl Chem 295:2035–2041. doi: 10.1007/s10967-012-2203-2
93. Conti CC, Salinas ICP, Zylberberg H (2013) A detailed procedure to simulate an HPGe detector with MCNP5. Prog Nucl Energy 66:35–40. doi: 10.1016/j.pnucene.2013.03.003
94. Haj-Heidari MT, Safari MJ, Afarideh H, Rouhi H (2016) Method for developing HPGe detector model in Monte Carlo simulation codes. Radiat Meas 88:1–6. doi: 10.1016/j.radmeas.2016.02.035

95. Aerospace Specification Metals Inc. AISI Type 304 Stainless Steel. <http://asm.matweb.com/search/SpecificMaterial.asp?bassnum=mq304a>. Accessed 27 Mar 2017
96. Nethaway DR, Van Konynenburg RA, Adams TM (1976) MEASUREMENT OF THE NEUTRON SPECTRUM ON A THICK BERYLLIUM TARGET FROM THE REACTION OF 30-MeV DEUTERONS. Natl Tech Inf Serv UCID52024.
97. Shieldwerx SWX-500 Series Activation Foils Specification Sheet. <http://www.shieldwerx.com/assets/swx-5xx.pdf>. Accessed 27 Mar 2017
98. Goodfellow (2014) Stainless Steel - AISI 304 - Foil. goodfellowusa.com. Accessed 7 Mar 2017
99. McConn RJ, Gesh CJ, Pagh RT, et al (2011) Compendium of Material Composition Data for Radiation Transport Modeling. PNNL-15870 Rev 1. doi: 10.2172/1023125
100. Zadeh EE, Feghhi SAH, Bayat E, Roshani GH (2014) Gaussian Energy Broadening Function of an HPGe Detector in the Range of 40 keV to 1 . 46 MeV. J Exp Phys 2014:1–5. doi: 10.1155/2014/623683
101. Rooney B, Garner S, Felsher P, Karpus P (2017) PeakEasy 4.96. Los Alamos National Laboratory.
102. Wang S, Landsberger S (2016) MCNP modeling of NORM dosimetry in the oil and gas industry. J Radioanal Nucl Chem 309:367–371. doi: 10.1007/s10967-016-4781-x
103. Assar E, Motavalli LR, Miri-Hakimabad H, Vejdani-Noghreiyani A (2013) The operator dose assessment of landmine detection systems using the neutron backscattering method. J Radioanal Nucl Chem 298:375–381. doi: 10.1007/s10967-013-2501-3
104. Sharma MK, Alajo AB, Liu X (2014) MCNP modeling of a neutron generator and its shielding at Missouri University of Science and Technology. Nucl Instruments Methods Phys Res Sect A Accel Spectrometers, Detect Assoc Equip 767:126–134. doi: 10.1016/j.nima.2014.08.011
105. Auxier JP, Auxier JD, Hall HL (2017) Review of current nuclear fallout codes. J Environ Radioact 171:246–252. doi: 10.1016/j.jenvrad.2017.02.010
106. (2010) Planning Guidance for Response to a Nuclear Detonation, 2nd Edition. <https://www.remm.nlm.gov/PlanningGuidanceNuclearDetonation.pdf>. Accessed 26 Jun 2017
107. Perez-Andujar A, Pibida L (2004) Performance of CdTe, HPGe and NaI(Tl) detectors for radioactivity measurements. Appl Radiat Isot 60:41–47. doi: 10.1016/j.apradiso.2003.10.006
108. Hung NQ, Chuong HD, Vuong LQ, et al (2016) Intercomparison NaI(Tl) and

- HPGe spectrometry to studies of natural radioactivity on geological samples. *J Environ Radioact* 164:197–201. doi: 10.1016/j.jenvrad.2016.07.035
109. Gunnink R, Niday JB (1972) *Computerized Quantitative Analysis by Gamma-ray Spectroscopy (Gamanal)*, Vol. 1-4, UCRL-51061.
 110. Coursey JS, Schwab DJ, Tsai JJ, Dragoset RA (2015) *Atomic Weights and Isotopic Compositions with Relative Atomic Masses*. In: NIST Phys. Meas. Lab. <https://www.nist.gov/pml/atomic-weights-and-isotopic-compositions-relative-atomic-masses>. Accessed 5 Jun 2017
 111. Ilas G, Gauld IC, Liljenfeldt H (2014) Validation of ORIGEN for LWR used fuel decay heat analysis with scale. *Nucl Eng Des* 273:58–67. doi: 10.1016/j.nucengdes.2014.02.026
 112. Gilbert MR, Fleming M, Sublet JC (2017) Automated inventory and material science scoping calculations under fission and fusion conditions. *Nucl Eng Technol* 49:1346–1353. doi: 10.1016/j.net.2017.07.005
 113. Watt BE (1952) Energy spectrum of neutrons from thermal fission of U235. *Phys Rev* 87:1037–1041. doi: 10.1103/PhysRev.87.1037